Photoluminescence and Photoconductive Dynamics of InAs/InAsSb In-Plane Ultrahigh-Density Quantum Dots

OON SIM JUI

Department of Engineering Science

The University of Electro-Communications

This dissertation is submitted for the degree of

Doctor of Philosophy

December 2024

Supervisory Committee

Chairperson:

Professor Koichi Yamaguchi

Reviewing committees:

Professor Tomah Sogabe

Professor Tsuyoshi Okuno

Professor Yoshinao Mizugaki

Associate Professor Naoya Miyashita

和文概要

量子ドット間の電子的強結合により、量子ドット分子構造や量子ドット結晶構造の新たな固体物質の創製が期待されている。従来のエピタキシャル成長による自己形成量子ドットの研究では、量子ドットを近接積層した構造の縦方向における量子ドット分子や１次元量子ドット鎖が作製され、それらの光電子物性やデバイス応用の研究が盛んに進められてきた。一方、量子ドットの面内で近接した超高密度化が難しく、量子ドットの面内強結合の研究は遅れていた。本研究では、世界最高密度（8-10 $\times 10^{11}$ cm^{-2}）の InAs/InAsSb 量子ドット構造を作製し、その光ルミネッセンスの温度依存性を詳細に調べ、一般的な低密度量子ドット構造に比べて異常な発光特性を示すことを見出した。また、面内超高密度量子ドット層の光伝導特性の温度依存性および光励起強度依存性から、２段階光励起効果や光伝導促進効果が観測され、面内超高密度量子ドット層における特有な光伝導ダイナミクスを明らかにした。

Abstract

Quantum dots (QDs) hold significant promise in optoelectronics and photovoltaics due to their size-tunable bandgap ability, leading to variations in optical absorption and emission spectra. This has fueled extensive research on the photoluminescence (PL) and photoconductive properties of various QD structures to understand their electronic behavior under different conditions. Following this trend, this study investigates ultra-high density (UHD) InAs/InAsSb QDs with a density of $0.8 - 1 \times 10^{12}\ cm^{-2}$ fabricated using molecular beam epitaxy (MBE). PL and photocurrent-voltage (J-V) measurements were employed to determine the electronic interactions and carrier transport mechanisms between these closely packed in-plane QDs. While strong coupling between vertically stacked QDs has been explored through experiments and theoretical studies, similar investigations on in-plane self-assembled QDs are scarce due to their lower density and significant inhomogeneous broadening of QD size. Achieving UHD QDs while simultaneously understanding the carrier transport mechanisms within them remains a complex and challenging task. When the separation distance between QDs becomes sufficiently small, electron wavefunctions can overlap, leading to electronic interaction through tunneling and potentially strong coupling between adjacent QDs. UHD QDs are crucial for realizing this in-plane electronic strong coupling, allowing the formation of in-plane energy minibands within the QD layer. This study focuses on achieving in-plane UHD QDs and investigating the electronic interactions between neighboring QDs. Specifically, it aims to determine carrier transport within the in-plane UHD QD layer by providing evidence of strong QD coupling that leads to miniband formation.

Based on the observed temperature dependences of PL energy and decay times, strong coupling of UHD QDs was evident at 60 K, starting with excited states (ESs) and

progressing towards strong coupling at the ground states (GSs) as the temperature increased to 100 K. This suggests a dynamic process where QD coupling and miniband formation initiate from the higher energy side (ESs) at lower temperatures, gradually progressing towards the lower energy side (GSs) with increasing temperature. Temperature-dependent photocurrent density measurements highlighted UHD QDs with a photocurrent density 50 times greater than that of LD QDs above 120 K. This significant enhancement is attributed to the strong coupling between adjacent QDs and minibands in QD layer, facilitating lateral carrier transport and suppressing carrier annihilation due to recombination, thus contributing significantly to the photocurrent.

This study successfully achieved the fabrication of in-plane UHD QDs and investigated the electronic interactions between adjacent QDs. Notably, the electron transport mechanism within the UHD QD layer was determined through PL and J-V measurements and analyses. These analyses provided evidence of strong QD coupling leading to miniband formation in the UHD QD layer. Understanding strong QD coupling and miniband formation in UHD QDs opens doors for researchers in this field to explore the potential of self-assembled InAs QDs, particularly in-plane UHD QDs. Given the excellent PL properties and high photocurrent observed across a wide range of temperatures and photoexcitation intensities, UHD QD samples are promising candidates for incorporation into intermediate-band solar cells or any QD solar cells. This study on UHD QDs holds significant promise for the development of next-generation solar cells with improved efficiency and cost-effectiveness, contributing to a cleaner and more sustainable energy future.

Contents

Abbreviations

AFM	Atomic Force Microscopy
CCD	Charge-coupled Device
CS	Continuous State
DBR	Distributed Bragg Reflector
DOS	Density Of States
ES	Excited State
FF	Fill Factor
FWHM	Full Width Half Maximum
GS	Ground State
HD	High-Density
HDE	Heterogeneous Droplet Epitaxy
HEMT	High-Electron-Mobility Transistors
IBSC	Intermediate Band Solar Cells
IP	Ion Pump
J-V	Photocurrent-Voltage
LD	Low-Density
LPF	Low-pass Filter
MBE	Molecular Beam Epitaxy
ML	Monolayer
PCE	Power Conversion Efficiency
PL	Photoluminescence
QDIP	Quantum Dot Infrared Photodetectors
QDs	Quantum Dots
QDSL	Quantum Dot Superlattice
QW	Quantum Well
QX	Quasi-sunlight Concentration
RHEED	Reflection High Energy Diffraction
RTDs	Resonant Tunneling Diodes
SFM	Scanning Force Microscope
SI	Semi-insulating

S-K	Stranski-Krastanov
SSL	Self-size Limit
TMP	Turbo Molecular Pump
TSP	Titanium Sublimation Pump
UHD	Ultrahigh-density
WKB	Wentzel-Kramers-Brillouin
WL	Wetting Layer
2DEG	Two-Dimensional Electron Gas

Chapter 1. Introduction

1.1. Research Background

The drive for smaller and more efficient technology has led to a growing interest in nanomaterials, particularly semiconductor quantum dots (QDs). These nanoscale crystals, often known as the artificial atoms, have unique and adjustable properties due to three-dimensional quantum confinement[1]. These properties make QDs a key focus of research, not just for their scientific interest but also for their wide-ranging practical uses that can greatly benefit society. The special features of QDs come from their size-tunable bandgap, which allows precise control over their optical absorption and emission spectra. This adjustability means QDs can be designed with specific properties for particular uses, making them valuable in fields like optoelectronics, photovoltaics, quantum computing etc. For instance, in optoelectronics, QDs are used to create QD lasers[2,3] resonant tunneling diodes (RTDs)[4], and QD infrared photodetectors (QDIP)[5–9] with enhance performance efficiencies. In photovoltaics, QD-based solar cells like intermediate band solar cells (IBSC)[10–17] have the potential to have higher power conversion efficiency and lower costs compared to traditional materials. Beyond their technical applications, semiconductor QDs also have a significant impact on society. QD solar cells help address climate change by providing more efficient renewable energy solutions, reducing dependence on fossil fuels. Moreover, integration of QDs into electronic devices supports the trend towards miniaturize and multifunctional gadgets, driving innovation in consumer electronics, telecommunications, and other areas.

In Yamaguchi laboratory, the research group focuses on fabricating self-assembled QDs with high uniformity and developing structures with exceptionally high QD densities using Molecular Beam Epitaxy (MBE). We have achieved significant progress in several

aspects. First and foremost, the fabrication conditions for high-uniformity QD samples were established, and this initial step laid the foundation for further research on high-density QD structures. Other than that, Sb was introduced into the wetting layer (WL) of InAs QDs. This approach effectively suppressed the migration of adsorbed atoms, resulting in nucleation of high density QDs, suppressing coalescence of QDs, and leading to the creation of ultrahigh-density (UHD) QD structures[18,19]. In 2016, our research team achieved world-record QD density of $1 \times 10^{12}\ cm^{-2}$ where we successfully fabricated Type-I ultra-high-density InAs QD/InAsSb WL[20,21] and Type-II high density InAs QD on GaAsSb[22,23], representing significant milestones in QD density control. The high density InAs QDs were incorporated in the application of IBSC[24,25]. The IBSC structure is the existence of a band (the intermediate band) located between the conventional conduction band and valence band of a semiconductor. Presence of the IB aids in absorption of photons below band gap. From the study, it is important to note that QD density is utmost important to achieve high PCE. To achieve PCE of over 40%, 600 stack layers are needed if the normal QD density of $5 \times 10^{10}\ cm^{-2}$ is used. Hence, the best way to get power conversion efficiency (PCE) above 40% is to have QD density of $3 \times 10^{13}\ cm^{-2}$.

As we successfully grew in-plane UHD QDs, we introduced them into the type II solar cell sample, which consists of InAs QDs capped with a GaAsSb capping layer[26]. The type II sample was compared with a GaAs reference cell. Photocurrent-Voltage (*J-V)* measurements were carried out for both GaAs and UHD QDs. As the quasi-sunlight concentration increased from 1 sun to >10 suns, the *J-V* curves deteriorated for the GaAs reference cell. On the other hand, the *J-V* curve shape of UHD QD cells was almost maintained even at 11.5 suns, despite the 500μm wide separation of electrodes. Based on the graph of maximum power point versus quasi-sunlight concentration (*QX)*, the

maximum power output (P_{max}) of the GaAs cell was 12-18 % lower than that of the UHD QD cells at 11 suns. Above 4 *QX*, the UHD QD cells exceeded the P_{max} of the GaAs cell. From the calculation of equipotential distribution for the GaAs cell, as the *QX* increased, the photocurrent increased, which caused a voltage drop. When comparing the case of 1 sun to the case of 10 suns, the lateral voltage drop in the 10 suns condition was more severe, and it occurred in both p-GaAs and n-GaAs, which lowered the fill factor (*FF*) value of the GaAs cell. From these results, it is expected that UHD QD solar cells operating under high sunlight concentration will achieve higher P_{max} and PCE by optimizing the UHD QD cell structure and growth conditions.

The developed UHD QD structures enable interaction of electronic states between adjacent QDs and it is interesting for the development of new physical properties and device applications. When the interdot separation distance becomes small enough for the electron wavefunctions to overlap, the electronic interaction occurs through tunneling and strong coupling occurred between adjacent QDs. While there have been reports on experimental and theoretical studies regarding strong coupling between vertically-stacked QDs[27–32], there are fewer experimental studies on in-plane self-assembled QDs due to low QD density and large inhomogeneous broadening of the QD size. The UHD QD is one of the key factors in realizing in-plane electronic strong coupling between neighboring QDs and forming in-plane energy minibands in the QD layer. More recently, our research team has demonstrated in-plane miniband formation due to the strong coupling in ground states (GS) of InAs/InAsSb UHD QDs through photoluminescence (PL) properties and simulation model[33].

Research on QDs has made significant progress, particularly in creating UHD QD structures and exploring QD strong coupling phenomena. These advancements hold

immense potential for the development of novel QD-based devices with enhanced performance and functionality in various fields, including quantum information, photovoltaics, and optoelectronics.

1.2. Research Objectives

The objective of this study is to achieve in-plane UHD QDs and investigate the electronic interactions between adjacent QDs. Specifically, the aim is to determine carrier transport within the in-plane UHD QD layer by providing evidence of strong QD coupling leading to miniband formation in the UHD QD layer. Firstly, in-plane UHD QDs were fabricated using MBE. The strong coupling of neighboring QDs and the formation of in-plane minibands were analyzed by measuring the temperature dependence of PL spectra for UHD InAs QDs on InAsSb WL and comparing the PL characteristics with low-density (LD) QDs on InAs WL. Subsequently, *J-V* measurements were conducted to study the optoelectronic properties and photoconductance of UHD QDs and LD QDs. Additionally, to gain a deeper understanding of the carrier concentration and mobility of InAs QDs, Hall effect measurements were conducted under both light and dark conditions. With these properties elucidated through PL, *J-V*, and Hall effect analysis, the development of QD-based devices such as photodetectors, QD lasers, and IBSC will be further enhanced, benefiting not only our laboratory research group but also contributing to researchers in the field of QD.

Chapter 2. Literature Review

2.1. Quantum Dots (QD)

2.1.1. Characteristics of Quantum Dots

Quantum dots (QDs) are a unique class of quantum effect nanodevices that exhibit distinct electronic and optical properties compared to their three-dimensional bulk crystal counterparts. This remarkable behavior arises from the confinement of electrons and holes within nanoscale structures smaller than their de Broglie wavelengths[34]. Based on the dimensionality of the carrier confinement, these quantum structures are categorized into quantum wells, quantum wires, and quantum dots. When carrier confinement is restricted to one dimension, the resulting structure is known as a one-dimensional quantum well; two-dimensional carrier confinement leads to the formation of quantum wires; the ultimate form of carrier confinement occurs in three dimensions, resulting in quantum dots. The confinement of electrons within QDs significantly reduces their degrees of freedom, leading to a transformation of the electron state density. Figure 2.1 illustrates the density of states (DOS) for bulk crystals and other quantum structures. In

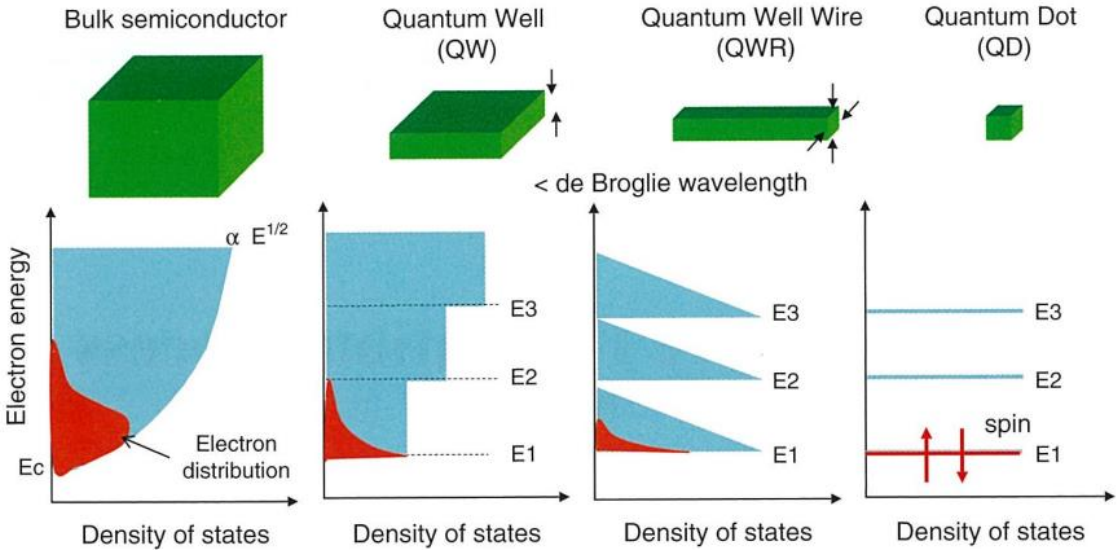

Figure 2.1 The density of states for bulk crystals and other quantum structures[18].

the case of QDs, the DOS behave like a delta function shape, causing the electron energy levels to become discrete. Hence, QDs have been referred to as "artificial atoms." The lowest energy level within a QD's discrete set of energy levels is referred to as the ground states (GS), while higher energy levels are known as the excited states (ES).

The discrete energy levels of QDs have profound effects for their electronic and optical properties. The emission wavelength of light from QDs can be precisely controlled by adjusting their size. This tunability originates from the direct relationship between QD size and the energy difference between the GS and ES. Besides that, QDs exhibit unique optical properties, including high luminescence efficiency and narrow emission linewidths. These properties arise from the strong confinement of excitons, the bound states of electrons and holes within QDs. These properties of QDs are important for a wide range of device applications, including quantum computing, quantum lasers, and solar cells that can absorb a broader spectrum of sunlight.

2.1.2. Band Structure of InAs QDs on InAsSb WL

In this study, the InAs QDs are fabricated on InAsSb WL, on top of semi-insulating (SI) GaAs substrates using MBE. The bandgap of GaAs is 1.52 eV at low temperatures, while the bandgap of InAs is 0.35 eV. InAs QDs are embedded in GaAs capping layer, the band structure of the QD sample is shown in Figure 2.2. Estimation values of electron affinities ($\chi_1, \chi_2, \chi_3, \chi_4$), bandgaps ($E_{g1}, E_{g2}, E_{g3}, E_{g4}$), and energy differences between valence bands and conduction bands ($\Delta E_{v1}, \Delta E_{v2}, \Delta E_{v3}, \Delta E_{c1}, \Delta E_{c2}, \Delta E_{c3}$) were calculated based on measurements from several studies[35–38]. In this configuration, electrons and holes are confined to the lower-energy InAs QDs, which are extremely small, typically ranging from a few to tens of nanometers in size. This confinement leads to quantum size

effects.

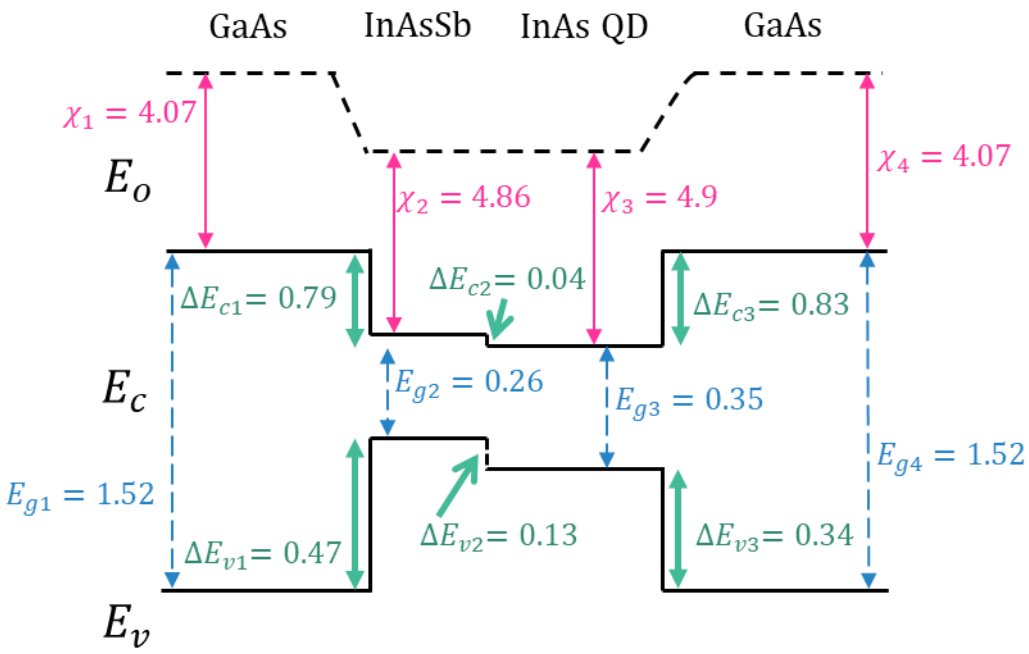

Figure 2.2 Band structure of InAs QD on InAsSb WL.

2.1.3. Crystal Growth Process of Self-Assembled QDs

The InAs QD samples discussed in this study were self-assembled QDs fabricated using MBE. Detailed descriptions of the MBE equipment will be explained in Section 2.2. Self-assembled QDs are semiconductor nanostructures that form spontaneously during epitaxial crystal growth. They are called "self-assembled" because their formation is driven by the natural tendency of atoms or molecules to arrange themselves into energetically favorable configurations. In our laboratory, the growth method of self-assembled QDs is through Stranski-Krastanov (*S-K*) growth mode, where a 2-dimension to 3-dimension growth mode transition is observed in heteroepitaxial growth of lattice mismatch materials[39,40]. The lattice mismatch between GaAs and InAs is approximately 7.2 % in this case. When InAs is heteroepitaxially grown on a GaAs layer, InAs experiences compressive strain due to GaAs's smaller lattice constant, leading to an

increase in strain energy. Strain energy increases as growth progresses, growth mode transition from 2D to 3D growth upon reaching InAs's critical thickness of 1.6 monolayer (*ML*), resulting in 3D islands (the self-assembled QDs) with high crystal quality. On the other hand, dislocations will form in case of excessive growth. Reflection High Energy Diffraction (RHEED) monitoring is used during crystal growth process, in which the diffraction beam intensity is used as a function of growth time for InAs growth on GaAs. When InAs coverage exceeds critical thickness for 2D-3D growth-mode transition, RHEED pattern changes from streak pattern to spot pattern as shown in Figure 2.3. Beam intensity will increase rapidly and randomly, meanwhile lateral size and height of QDs immediately saturate. Comprehensive explanations of the RHEED functions will be provided in Section 2.3.

As high density QDs play an important role in improving the performance of various applications, conventional type of *S-K* growth of QD under low temperature, high Arsenide pressure, and higher growth rate could yield high QD densities. However, coalescence of QDs and dislocations are often observed. Therefore, self-size limit (*SSL*) growth is important to enhance QD size uniformity, by employing low Arsenide pressure

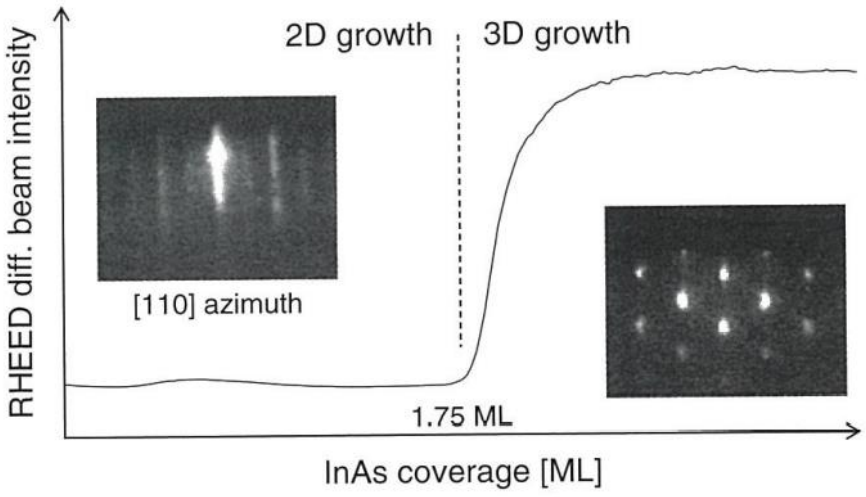

Figure 2.3 RHEED diffraction beam intensity of 2D-3D growth mode transition[18].

and a low growth rate[41]. As the coverage of InAs increases, the lateral size of 2D platelets expands until it reaches a certain width (in nanometer), where it becomes automatically limited. This behavior, attributed to the strained step edges of the platelets, facilitates the formation of uniform and sizable 2D platelets. Rapid transition from 2D to 3D mode occurs, resulting in the emergence of stable facets on the sidewalls of the QDs, eventually leading to the formation of similar pyramidal QDs, as shown in Figure 2.4. Upon surpassing the critical thickness, both the lateral size and height of the QDs remain unchanged and reach immediate saturation, except in cases of coalescence QDs. The two-step SSL process successfully yields QDs with narrow size fluctuation. While the advantage lies in the fact that their formation requires no additional processing steps, and they are intrinsically free from defects and dislocations, yet this process possesses a challenge to control their size uniformity and arrangement.

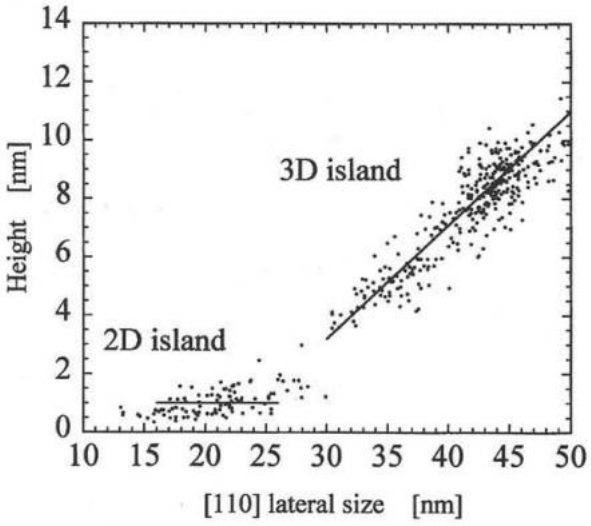

Figure 2.4 The dimension distribution of 2D islands and 3D dots[41].

2.1.4. Formation of Ultrahigh-Density QDs by Introducing Sb into Wetting Layer

In order to achieve high uniformity, density, and crystal quality of the InAs QDs, the

coalescence and ripening of neighboring QDs were efficiently inhibited through a Sb-mediated *S-K* growth mode[42,43]. This involved introducing Sb atoms into the WL prior to the growth of InAs QDs. The lattice mismatch between InAsSb and GaAs creates a higher compressive strain in the 2D islands compared to pure InAs. This strain restricts the lateral growth of the InAsSb islands, ultimately leading to a higher density of smaller islands. Figure 2.5 (a) shows the step edges of the 2D islands on the surface of samples grown with 1.25 *ML* of InAs WL and 1.25 *ML* of InAsSb WL on GaAs substrates using atomic force microscopy (AFM). The InAsSb WL has significantly higher density of 2D islands and step edges as compared to that of InAs WL[21].

Sb atoms on the surface and step-like features of the InAsSb WL act as potential energy barriers, reducing the possibility of migration of adsorbed atoms. This further promotes the formation of distinct islands rather than a continuous layer. The steps on the InAsSb WL also serve as nucleation sites for the formation of QDs, further contributing to growing higher density QDs. In addition, the segregation of Sb atoms helps to prevent neighboring 3D islands from merging, ensuring they remain small and distinct, ultimately

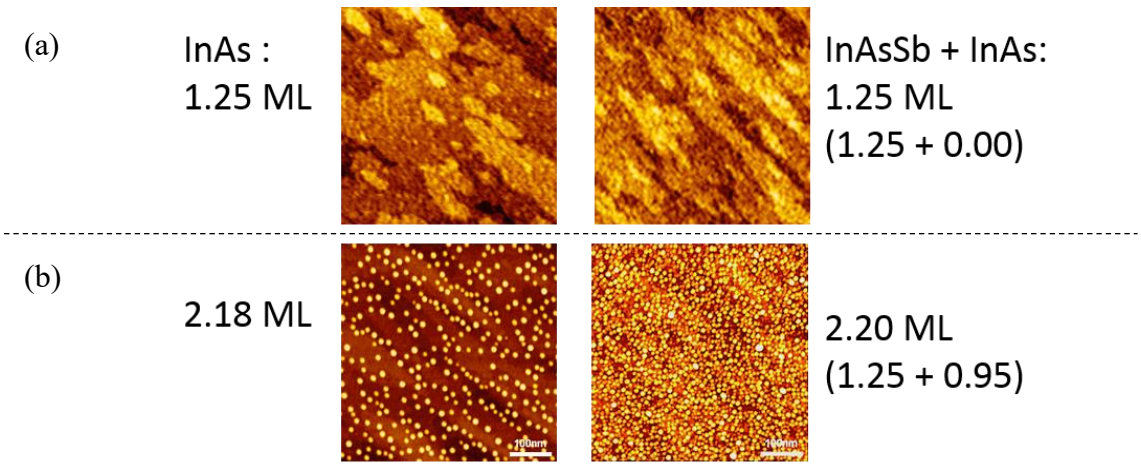

Figure 2.5 (a) Step edges of the 2D islands on the surface of samples grown with 1.25 ML of InAs WL and InAsSb WL on GaAs substrates, (b) InAs coverage of LD QDs (2.18 ML) and UHD QDs (2.2 ML)[21].

leading to a higher overall density of QDs. As shown in Figure 2.5 (b), beyond the critical thickness of around 1.6 *ML*, when the InAs coverage reaches 2.18 *ML* in InAs QD/InAs WL sample and the InAs coverage reaches 2.20 *ML* in InAs QDs/InAsSb sample, QD density increases sharply, resulting in significant differences in densities of $4 \times 10^{10}\ cm^{-2}$ (LD QDs) and $1 \times 10^{12}\ cm^{-2}$ (UHD QDs) respectively.

2.2. Molecular Beam Epitaxy (MBE)

2.2.1. Principles of MBE

MBE is an epitaxial growth technique for semiconductors, and crystal growth is achieved by reaction of thermal beams of atoms or molecules with a crystalline surface under ultra-high vacuum conditions (below 10^{-10} Torr)[44,45]. MBE can achieve precise control in both chemical compositions and doping profiles. It enables precise fabrication of thin layers from a fraction of a micron down to a monolayer.

The elements that serve as the raw materials for the crystal are placed in separate effusion cells (Knudsen cells), and the respective effusion cells are heated to generate molecular beams. Crystal growth is then achieved through interaction with the crystal substrate. Each effusion cell is equipped with a thermocouple for temperature detection and a resistance heating heater. By heating the effusion cell to a certain temperature, the raw material is ejected as a vapor. Keeping the chamber under ultra-high vacuum ensures that the average mean free path of the evaporated raw material molecules is sufficiently long, allowing them to reach the substrate in the form of molecular beams. Each effusion cell can control the supply and termination of raw materials by opening and closing the shutter, enabling precise thin-film growth at the atomic level. In addition, the ultra-high vacuum environment allows the surface of the cleaned substrate to be maintained, and the

growth rate can be slowed down to reduce impurity incorporation into the crystal. This allows for the growth of high-quality epitaxial single crystals. Furthermore, by changing the temperature at which each effusion cell is heated, the vapor pressure of each raw material molecular beam can be controlled, and the growth rate and composition of the crystal can be determined.

Since MBE involves crystal growth under ultra-high vacuum, the state of the substrate surface can be observed during crystal growth by irradiating the substrate with an electron beam via RHEED. By observing the reflection intensity and diffraction pattern of the electron beam, the flatness of the substrate during crystal growth and the formation of the three-dimensional structure can be confirmed.

2.2.2. Configuration of MBE

This MBE structure consists of three vacuum chambers as shown in Figure 2.6. The main chamber contains three vacuum pumps: an ion pump (IP), a titanium sublimation pump (TSP), and a turbo molecular pump (TMP). The IP is constantly operating to maintain ultra-high vacuum, and the TMP is used for initial vacuum pumping when the chamber is opened to atmospheric pressure. Before crystal growth begins, the TSP is used for further evacuation for about one minute to achieve a better vacuum. Second chamber is connected to the main chamber for transporting samples. This chamber is also maintained at high vacuum by the IP and connects to the main chamber via a transfer rod. The substrate is mounted on a trolley and moved into the main chamber. A load lock chamber (third chamber) is connected to the second chamber. Samples are introduced from here, and when the load lock chamber is opened to atmospheric pressure, it is purged

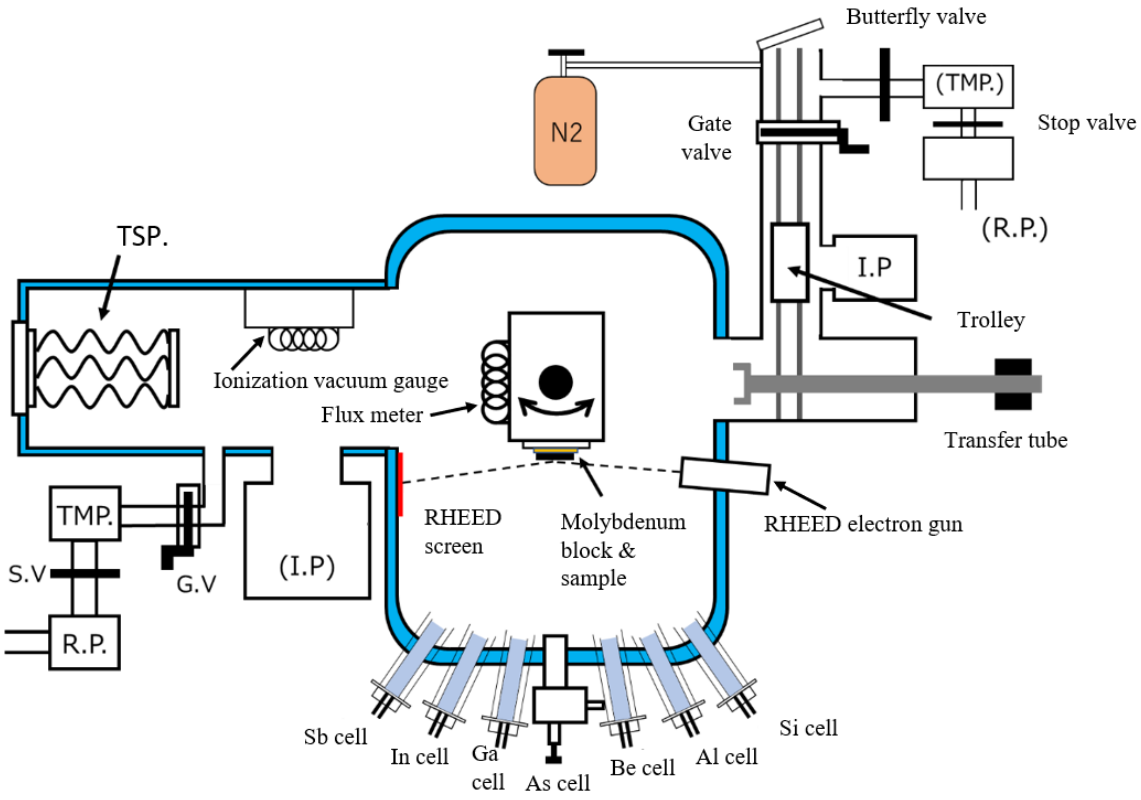

Figure 2.6 Structure of three chambers in MBE.

with nitrogen gas to prevent the introduction of reactive impurities.

The main chamber of the MBE system is equipped with effusion cells for In, Ga, Sb, Be, Al, and Si, and a valved cracker cell for As. The molecular flux of As can be controlled using a needle valve in the valved cracker cell, enabling more stable molecular beam supply and faster flux changes compared to temperature control. The valved cracker cell also has a cracking function that heats the cell outlet to decompose As_4 into As_2 molecules, which are then delivered to the substrate. Compared to As_4, As_2 has a higher adsorption coefficient on the substrate, resulting in fewer defects in the grown crystals and source material savings. However, for this study, As_4 was supplied to the substrate for crystal growth to align with previous studies.

In MBE, molecules emitted in the form of molecular beams that do not adsorb to the substrate are cooled and deposited on the inner walls of the chamber, maintaining ultra-

high vacuum in the chamber space during crystal growth. There are two methods for cooling the chamber walls: liquid nitrogen cooling and water cooling. In our laboratory, water cooling is employed. The substrate for crystal growth is attached to a molybdenum block with In and fixed to a holder on a manipulator in the main chamber. The manipulator can be rotated manually and by motor to ensure uniform crystal growth over the entire substrate. Furthermore, a flux meter is attached to another side of the manipulator, allowing flux measurement by directing it towards each cell. Electron beams emitted from RHEED are reflected and diffracted on the substrate and project an image onto the opposite screen.

2.3. Reflection High Energy Diffraction (RHEED)

2.3.1. Principles of RHEED

RHEED is a technique for investigating the surface state of crystals by observing the image projected onto a fluorescent screen when 10-50 kV accelerated electrons are incident on the sample substrate surface at a shallow angle of 1-2° and are reflected and diffracted by the surface atoms. Figure 2.7 shows the diffraction conditions (real and reciprocal space) of RHEED during MBE process. Because the electron beams are incident and diffracted at extremely shallow angles, they have little effect on molecular beams irradiated almost perpendicularly, making RHEED a preferred method for surface observation in MBE. The diffraction condition is the intersection point of the Ewald sphere and the reciprocal lattice point, which appears as a spot on the fluorescent screen[34,46]. The diffraction condition is given by the equation below:

$$k_1 - k_0 = a^* \tag{2.1}$$

Where k_0 is the wavevector of the incident electron beam, and k_1 is the wavevector of the diffracted electron beam. As the energy loss in diffraction process is very small and almost negligible, the diffraction condition can be expressed by the intersection point of Ewald's sphere (with radius $|k_0|$) and reciprocal lattice point. In real case, when crystal growth is conducted using MBE, the substrate surface contains adsorbed atoms, growth nuclei, two-dimensional islands, crystal defects, etc., and is not perfectly flat. Diffraction in RHEED only occurs on very thin surface, hence it lacks periodicity in vertical direction (2D lattice). The reciprocal 2D lattice appears on the screen as an elongated streak (1D rod array). Additionally, if three-dimensional structures occur on the substrate surface, diffraction patterns are projected onto the screen as spots. It is due to the radius of Ewald's sphere is much larger than the spacing of reciprocal lattice. In an ideal 2D lattice, the spot would be small and sharp. However, in practical scenarios, the spot is slightly thicker and

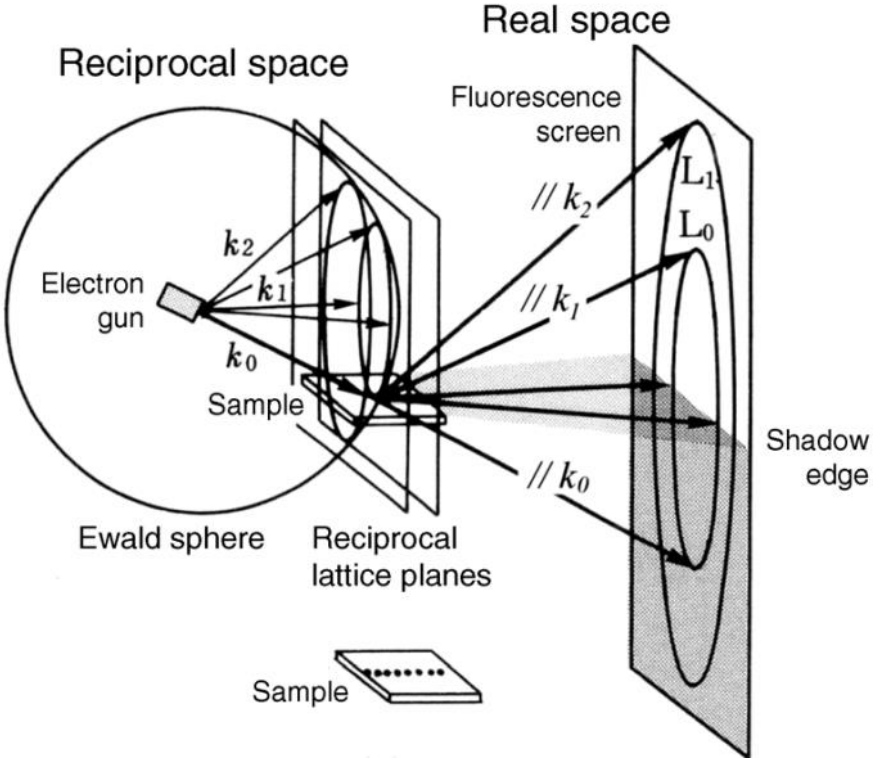

Figure 2.7 The diffraction conditions (real and reciprocal space) of RHEED during MBE process[46].

takes on an elongated shape due to the uneven surface. Oscillation of diffracted spots has been observed due to the repetition of rough and flat surface segments. This oscillation phenomenon is utilized to estimate growth rate and beam intensity.

2.3.2. RHEED Oscillations

Real-time observation of the crystal surface using RHEED is crucial for controlling thin film growth rate and film thickness. During thin film growth, periodic oscillations in the RHEED reflected beam intensity can be observed. Figure 2.8 shows the oscillation of the RHEED reflected beam intensity during GaAs growth on GaAs(001). This corresponds to the oscillation of the substrate surface flatness over time, and the period of the reflected beam intensity is equal to the growth time of one molecular layer. The intensity of the RHEED reflected beam decreases immediately after opening the Ga cell shutter. Once it reaches a certain intensity, it decreases and the oscillation cycle repeats.

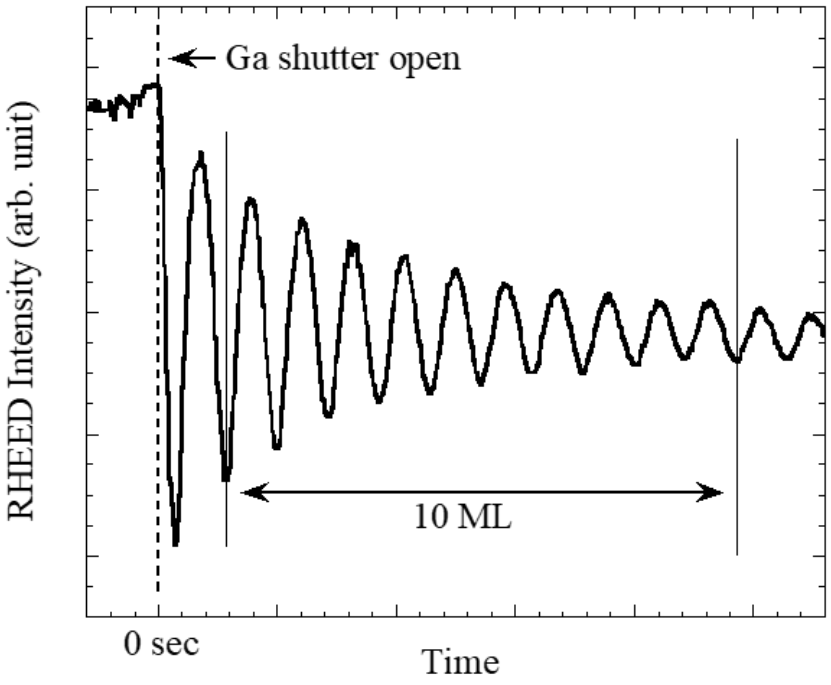

Figure 2.8 RHEED intensity oscillation during GaAs crystal growth.

The amplitude of the oscillation will decrease gradually, and after a while, the oscillation becomes undetectable. The intensity of the reflected beam becomes stronger when the surface flatness is high and weaker when the flatness is poor due to the formation of 2D nuclei by opening the Ga shutter. This flatness depends on the GaAs coverage rate. The amplitude decreases as the surface becomes rougher with repeated cycles. However, the amplitude of the intensity can be recovered by pausing the growth and waiting for the flatness to recover. The GaAs growth rate can be calculated by equation 2.2 given the number of oscillations (number of grown molecular layers), lattice constant of GaAs, and the oscillation time.

$$(Growth\ rate)[nm/s] = \frac{(No.of\ oscillation) \times (Lattice\ constant\ of\ GaAs) \div 2}{(Oscillation\ time)} \quad (2.2)$$

2.3.3. Confirmation of InAs QDs using RHEED

Figure 2.9 shows the transition of RHEED diffraction beam intensity during the growth of InAs QDs on a GaAs buffer layer using the *S-K* growth mode. After opening the In shutter, the streak patterns from the GaAs(001) surface and the InAs WL transitions to spot patterns when 3D islands are formed. When the streak pattern becomes spot pattern, RHEED diffraction intensity increases. The time taken for this rise is considered as the critical thickness growth time in the *S-K* growth mode, which allows for the determination of the growth rate of InAs. The critical thickness of InAs is approximately 1.6 *ML* on GaAs. The growth rate of InAs was derived using the following equation:

$$(Growth\ rate)[ML/s] = \frac{(Critical\ thickness)[ML]}{(Rise\ time)[sec]} \quad (2.3)$$

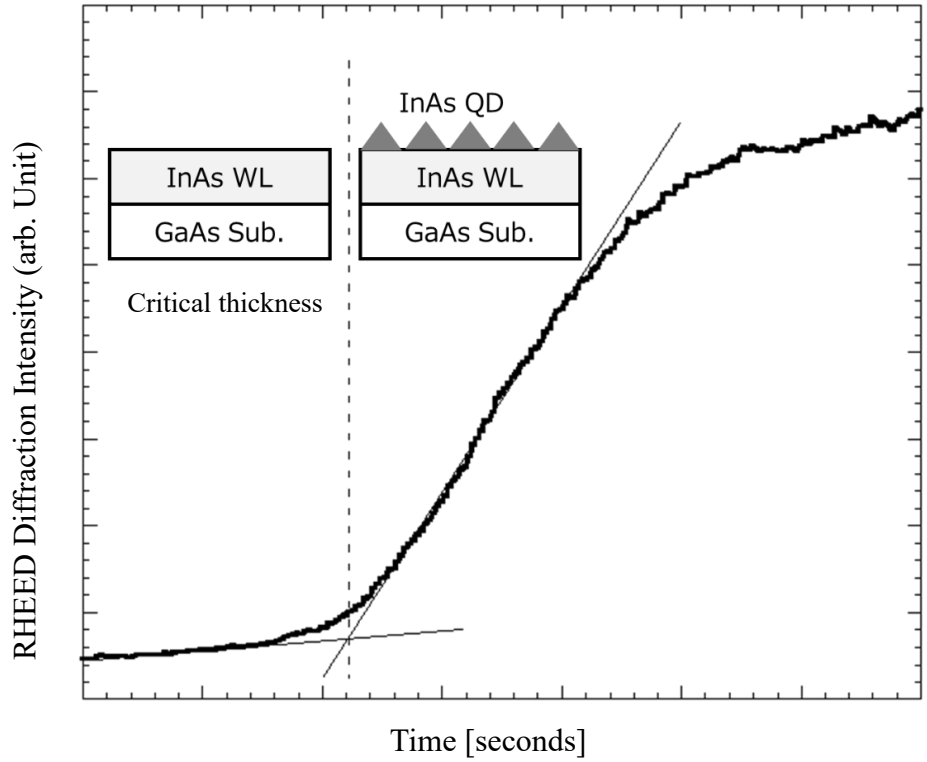

Figure 2.9 The change in RHEED diffraction intensity during crystal growth of InAs QDs on GaAs.

2.4. Chapter Summary

QDs are nanoscale semiconductor particles with unique electronic and optical properties due to quantum confinement, which results in discrete energy levels and tunable light emission. This chapter explores the characteristics and fabrication processes of InAs QDs grown on InAsSb wetting layers using MBE. The significant bandgap differences between GaAs and InAs facilitate electron and hole confinement, enhancing the QDs' quantum properties. The self-assembly process, driven by lattice mismatch and strain, transitions from 2D to 3D growth, forming high-quality QDs. Introducing Sb into the WL increases QD density and uniformity by enhancing compressive strain, crucial for improving the performance of QD-based applications in quantum computing, lasers, and solar cells.

Chapter 3. Methodology

3.1. MBE Process

3.3.1. Sample Preparation

In the preparation of test samples, semi-insulating (SI) GaAs(001) substrates were used. The substrates were cleaved from wafers to approximately $1\ \text{cm} \times 0.8\ \text{cm}$ in size. As-received SI GaAs(001) substrates are contaminated with various impurities. Direct epitaxial growth by MBE on these contaminated substrates would not only contaminate the MBE chamber but also result in the growth of non-uniform and low-quality epitaxial films with high defect and dislocation densities. Therefore, the substrates were etched prior to MBE growth to remove the surface contamination layer. The etching process consisted of three steps: (1) organic cleaning, (2) piranha etching, and (3) rinsing.

In stage (1) organic cleaning, the substrate was washed approximately 20 times with acetone and then approximately 20 times with distilled (DI) water in a beaker. The beaker was heated on a hot plate as needed to increase the solubility of impurities in the solvent. In stage (2) piranha etching, the substrate surface moisture was removed with sulfuric acid, followed by etching with piranha solution $(H_2SO_4 : H_2O_2 : H_2O = 4 : 1 : 1)$ for 20 seconds. In this etching step, the substrate surface was oxidized with H_2O_2, which is then removed by sulfuric acid. In stage (3) rinsing, the substrate after piranha etching was thoroughly rinsed approximately 20 times with DI water. Last but not least, the moisture that remained on the sample surface was blown dry with nitrogen gas.

3.3.2. Loading Process

After etching, the substrate was attached to the surface of a heated molybdenum block by surface tension of a melted Indium ribbon. Indium has a high thermal conductivity and

serves to uniformly transfer heat from the molybdenum block, which is heated during crystal growth. The molybdenum block with the attached substrate was loaded onto a trolley and transferred into an N_2-leaked load lock chamber. Vacuum pumping was performed using a TMP. After reaching high vacuum, the substrate was transported from load lock chamber to the main chamber through trolley.

3.3.3. Removal of Oxide Layer

Although the substrate surface was cleaned and contaminants were removed during sample preparation process, the substrate was exposed to the atmosphere before relocation into the MBE chamber, resulting in the formation of oxide layer of Ga and As on the substrate surface. Therefore, the substrate temperature was raised to remove the oxide layer. As the substrate temperature was raised, the shutter of As cell was adjusted to 300 °C to irradiate the substrate with an As_4 molecular beam, in order to prevent As evaporation from the substrate. As_4 was irradiated throughout the crystal growth of sample to keep the surrounding area in an As atmosphere.

Meanwhile, the surface condition was observed by RHEED at a substrate temperature of 580 °C, until the oxide layer was removed. The oxide layer is polycrystalline, so the RHEED diffraction pattern appears as rings. However, when the oxide layer is removed, a streak-like pattern (2×4) appears due to the periodic structure of the GaAs single crystal. The thermocouple temperature at this time was recorded and used to calibrate the thermocouple temperature and the actual substrate temperature. Calibration of temperature is needed as the placement of thermocouple is at the back of substrate holder, temperature difference exists between substrate and the holder.

3.3.4. Growth of GaAs Buffer Layer

After removing the oxide layer, a 200 nm GaAs buffer layer was grown at a substrate temperature of 590°C. Growing a GaAs buffer layer on the rough surface after oxide removal flattens the substrate surface for quantum dot growth and enables the growth of a crystalline quantum dot layer. In the initial stage of buffer layer growth, growth interruption was performed with a cycle of supplying Ga for 1 minute and interrupting for 30 seconds. This promotes Ga atom migration and flattens the crystal surface. The RHEED oscillation was observed during the growth interruption to determine the growth rate of the GaAs layer, which was used for thickness control of the GaAs buffer layer. Given that one cycle of the waveform corresponds to 1 *ML*, the GaAs growth rate of 200 nm GaAs buffer layer was approximately 0.13 nm/s.

3.3.5. Growth of InAs UHD QDs on InAsSb WL

After the growth of the GaAs buffer layer, the substrate temperature was lowered to the QD layer growth temperature of around 460 ℃. The RHEED pattern transitions from (2×4) to (4×4) streak-like pattern as the temperature decreases. After 1 minute, the As supply was reduced by changing the needle of the As needle valve. This is because low As supply and low growth rate result in formation of more uniform and high-quality QDs. After a total of 8-minute growth interruption, the substrate temperature reached the target value and the growth of the InAsSb WL began. The Sb and In shutters were opened at the same time, with continuous supply of As_4. Meanwhile, the RHEED e-beam was incident from the [110] direction of the GaAs, and the RHEED screen together with the oscillation window were observed very carefully to track the transformation of 2D islands (streak pattern) to 3D dots (spot pattern). In approximately 35 seconds, the Sb flux was closed

and this is when the QDs started to form. About 27 seconds, In flux was closed and the growth of InAs UHD QDs was completed. The sample undergo annealing for 15 seconds under constant supply of As flux.

Figure 3.1 shows the plot of RHEED diffraction beam intensity against growth time in InAs UHD QDs on InAsSb WL. When In and Sb supplies began, oscillations were observed during the initial half cycle due to the flatness of the growth surface. However, as a result of lattice mismatch with GaAs, the oscillations eventually disappeared as the 2D islands of InAsSb with step edges were formed. Transitioning from 2D to 3D growth when critical thickness was reached, the RHEED diffraction pattern changed from streak-like to spot-like, and the intensity increased sharply. The critical thickness was determined from the intersection point of the slopes before and after the increase, approximately 1.6 *ML*, and the growth rate of InAs and InAsSb were calculated based on the equation:

$$Growth\ rate\ (InAs\ and\ InAsSb) = \frac{Critical\ thickness}{2D \rightarrow 3D\ transition\ time}\ [ML/s] \qquad (3.1)$$

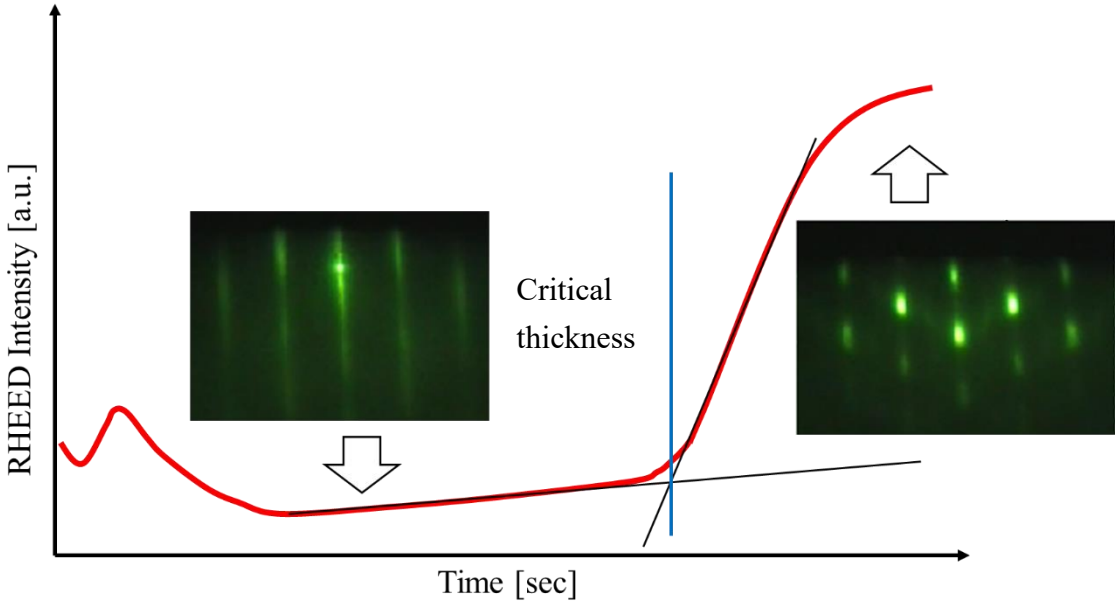

Figure 3.1 The RHEED diffraction intensity and RHEED diffraction patterns of 2D to 3D transitions of InAs UHD QDs on InAsSb WL during crystal growth process.

The growth rate of InAs UHD QDs was 0.035 *ML/s*, with the InAs coverage of 1.25 to 1.35 ML for InAsSb WL and 0.95 to 1 ML for InAs QDs.

3.3.6. Growth of GaAs Capping Layer

After the 15 seconds annealing process, embedding growth of InAs QDs with a GaAs capping layer was conducted for samples intended for PL measurements. The growth rate of GaAs during this phase was based on that of the GaAs buffer layer. The GaAs capping layer was grown to a thickness of 60 nm. After embedding growth, the substrate was rapidly cooled simultaneously with the closure of the Ga shutter. During rapid cooling, the supply of As was stopped by closing the As shutter when the substrate temperature dropped below 350°C to prevent clustering of As. QD samples intended for surface topology analysis using AFM were not subjected to embedding growth with GaAs capping layer. The sample was rapidly cooled after the completion of InAs QD layer growth.

3.3.7. Unloading Process

After crystal growth, the substrate temperature was allowed to cool down to 250 °C or below before being removed from the growth chamber. The sample was then transported to the load lock chamber via trolley. The load lock chamber was purged with nitrogen gas and the molybdenum block was removed from the chamber. Finally, the sample was detached from the molybdenum block by melting the Indium in between the block and sample.

3.2. Atomic Force Microscopy (AFM)

Atomic Force Microscopy (AFM), also known as the Scanning Force Microscope (SFM), is a versatile tool capable of measuring conductive, semiconductive, and non-conductive samples[47]. It provides a high-resolution 3D profile of surfaces on a nanoscale by measuring the forces between a sharp probe, typically less than 10 nm in diameter, and the surface at very short distances, typically ranging from 0.2 to 10 nm of probe-sample separation. The AFM probe is mounted on a flexible cantilever, resembling a spring, which gently touches the surface and records the small force between the probe and the surface, as shown in Figure 3.2. This force is dependent on the spring constant, or stiffness, of the cantilever and the distance between the probe and the sample surface, following Hooke's Law[48]:

$$F = -kx \tag{3.2}$$

where F represents force and x represents the distance the cantilever spring is bent. Controlled motion of the probe across the surface is achieved through a feedback loop

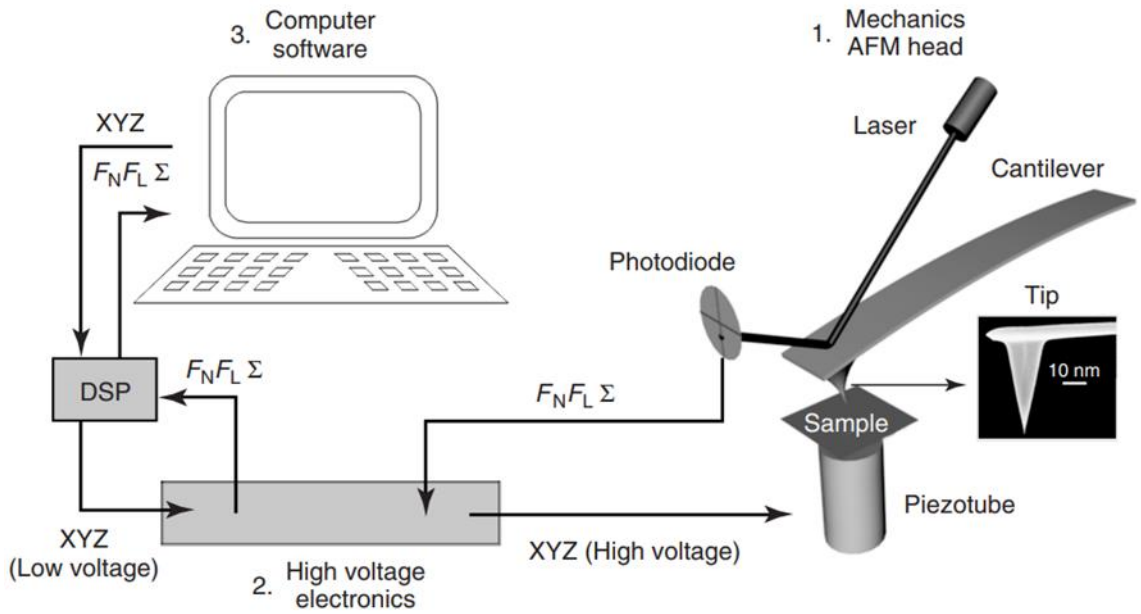

Figure 3.2 Schematic diagram of standard AFM setup[90].

and piezo electronic scanners. The deflection of the probe is typically measured using a "beam bounce" method, where a laser beam is directed onto the back of the cantilever and bounced into a photodiode detector. This detector measures the bending of the cantilever as the tip is scanned over the sample, and the measured cantilever deflections are used to generate the sample surface topography. In this study, contact mode was utilized where the probe-surface separation is typically less than 0.5 nm, the cantilever bends when its spring constant is less than that of the surface, resulting in a repulsive force on the tip. By maintaining a constant cantilever deflection, a constant force between the probe and the sample is achieved, allowing for the acquisition of surface images.

AFM is particularly useful for characterizing nanoparticles ranging from 0.5 nm to 50 nm in diameter, including those with variable geometries. It can also be employed for analyzing nanoparticle physical properties such as magnetic fields and determining nanoparticle size. Additionally, AFM can be utilized for rough samples and measuring friction, although fast scanning may cause damage to soft samples. In this study, apart from using the AFM equipment, both “NanoNavi II” and “SPIP” software as shown in Figure 3.3 were used after AFM measurements were obtained to analyze the lateral size

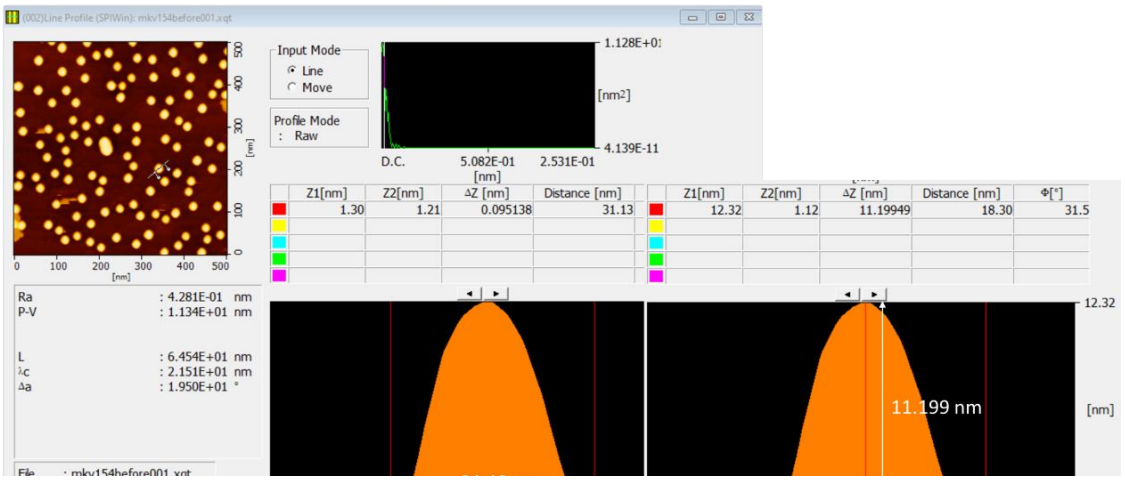

Figure 3.3 “NanoNavi II” software to determine the lateral size and height of InAs QDs. From analysis, the lateral size of LD QD is about 31 nm; height is about 11 nm.

and height of the InAs QDs. In order to determine the density of InAs QDs, the software "Katikati Counter" was used as shown in Figure 3.4.

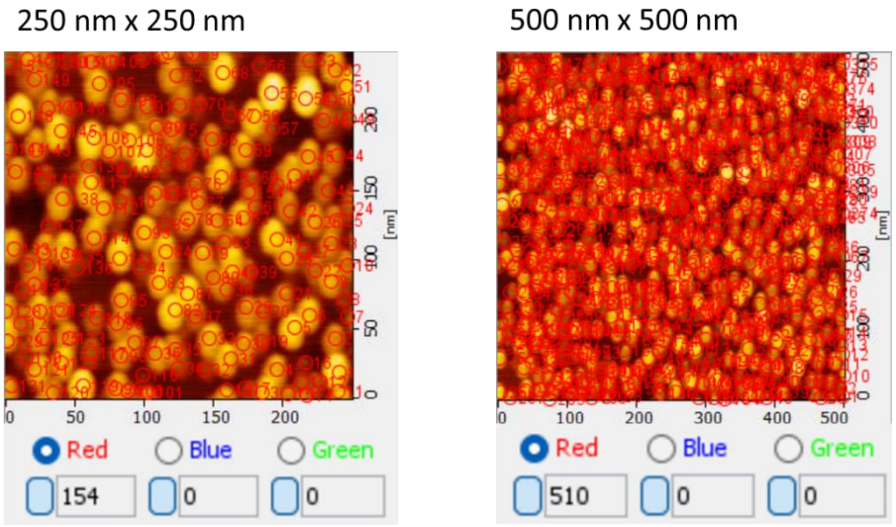

Figure 3.4 "Katikati Counter" software to determine the density of InAs high-density (HD) QDs from 250 nm^2 and 500 nm^2 inspection area. The average QD density from HD QDs is $3 \times 10^{11}\ cm^{-2}$.

3.3. Photoluminescence (PL)

Photoluminescence (PL) is a phenomenon characterized by the spontaneous emission of light from a material upon photon absorption[49]. This emission spectra are used to identify surface, interface, and impurity levels, as well as assessing alloy disorder and interface roughness. The intensity of the PL signal could indicate surface and interface quality, offering insights into radiative and nonradiative recombination rates. When a material absorbs light of sufficient energy, it generates electronic excitations. Subsequently, as these excitations relax, electrons return to their ground state. If this relaxation process involves radiative emission, the emitted light can be collected and analyzed to glean information about the photoexcited material. Surface recombination processes typically result in nonradiative emission, diminishing the overall PL intensity.

Additionally, the formation of a depletion region or 'dead layer' induced by band bending at interfaces can further contribute to a decrease in PL intensity.

In this study, PL measurements were conducted as an evaluation method for the InAs QD samples. PL measurement involves the excitation of electron-hole pairs in the sample by illuminating it with light, and observing the luminescence emitted when the excited carriers relax by recombination, releasing energy in the form of light. By incorporating a microscope into the optical system, it is possible to observe the sample surface while locally irradiating the excitation light, enabling measurement of the luminescent characteristics of small areas. Two types of PL measurement setups were used to determine PL properties of samples, namely macro-PL and micro-PL.

3.3.1. Macro-PL

Figure 3.5 illustrates the schematic diagram of Macro-PL measurement system. Sample is mounted in a cryostat using Ag paste, and a cooling system utilizing Helium gas is used to lower the temperature to 4.2 K. A laser with a wavelength of 635nm and an output power of 100mW is used as the excitation light, which is directed onto the sample. The laser light is intermittently interrupted by a chopper rotating at approximately 380 Hz, resulting in a rectangular wave excitation light. Before reaching the InGaAs photodetector, the light passes through a 700 nm low-pass filter (LPF) and a spectrometer. The purpose of the 700nm LPF is to prevent the photodetector from being damaged by a portion of the 635nm laser light reflected from the sample. After that, the spectrometer narrows down the wavelength of the incoming light using internal diffraction gratings. To reduce noise, the signal obtained from the photodetector and the reference signal from the chopper are input into a lock-in amplifier. Finally, PL intensity of the sample is extracted

and recorded as a function of wavelength.

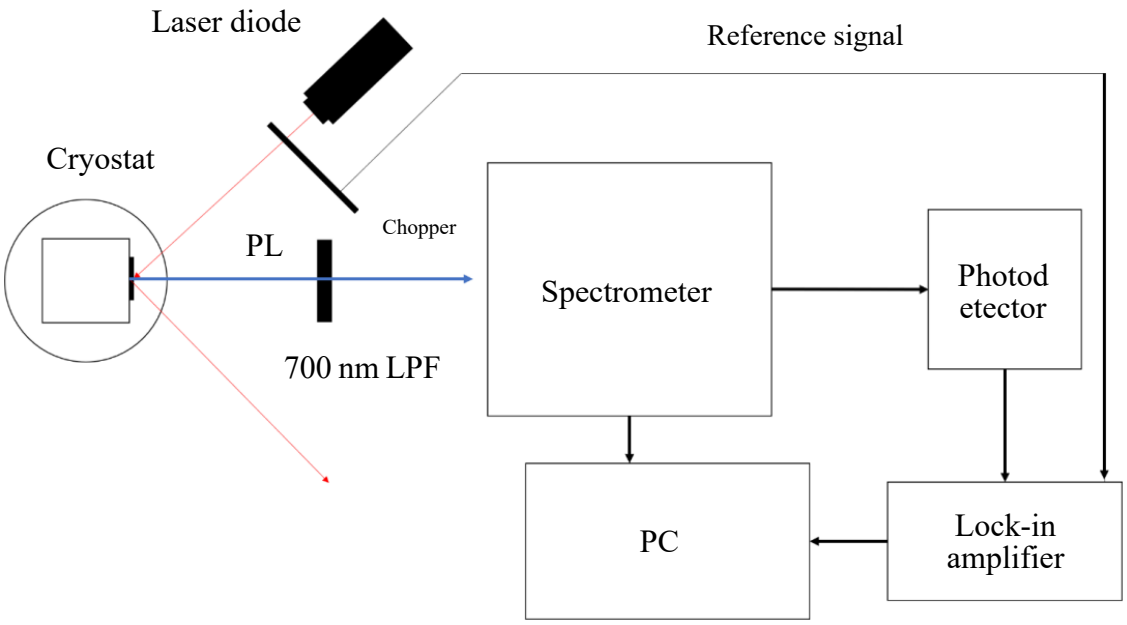

Figure 3.5 Schematic diagram of Macro-PL measurement system.

3.3.2. Micro-PL

Figure 3.6 shows the schematic diagram of micro-PL measurement setup. The sample was affixed to a cryostat using melted Ag paste. The cryostat stores liquid He in a tank and can be cooled to at least 4 K by flowing liquid He through a transfer tube. Temperature can be regulated by adjusting the heater and the supply of liquid He using a temperature controller. During cooling, the vacuum chamber is evacuated by a rotary pump and a turbo molecular pump, and measurements were conducted in a temperature range from 15 K to room temperature.

A semiconductor laser and a white fiber laser were used as excitation light sources. White laser allows for the selection of a specific wavelength using a spectrometer, while semiconductor lasers offer direct access to specific wavelengths such as 785 nm, 850.7 nm, 926.7 nm, 1052.5 nm, and 1290.5 nm. For the PL measurements, 785 nm laser with

an energy greater than the bandgap of GaAs, is chosen as the excitation source. Whereas for the photocurrent-voltage measurements, white laser with 925 nm is used. The laser diode used in this study can reach maximum power of 300 mW and the wavelength resolution for detection in this PL system is 1.27 nm. The PL light emitted by the sample is captured and analyzed using InGaAs photodiode array. The array consists of 512 individual InGaAs photodiodes arranged in a grid pattern. It detects the PL light that has been spectrally resolved by the spectrometer, enabling the measurement of the PL spectrum. The excitation light is focused by an objective lens before reaching the sample. In Micro-PL system, the position of the sample on the stage can be adjusted to control the illumination area and intensity per unit area. Additionally, a XYZ-axis manipulator within the cryostat allows for precise micro-positioning of the laser beam on the sample, meanwhile real-time monitoring of the sample surface condition can be observed throughout measurement.

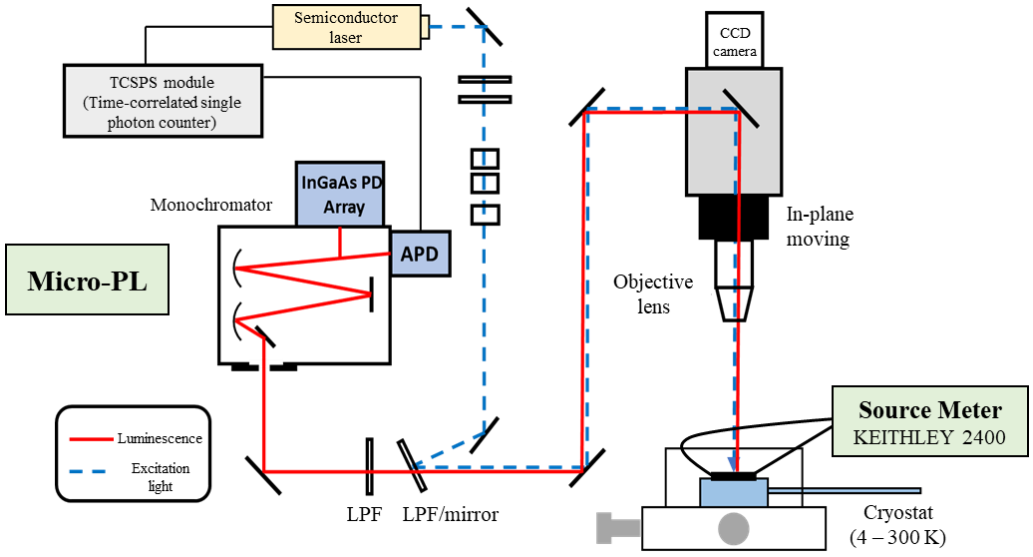

Figure 3.6 Schematic diagram of Micro-PL measurement system.

3.4. Photocurrent-Voltage Measurement

I-V measurement, also known as current-voltage characteristic measurement, is a technique used to analyze the relationship between the voltage applied across an electrical device and the current flowing through it. I-V measurements can be done by gradually increasing or decreasing the voltage, and measuring the current flowing through the sample at each voltage level. Whereas photocurrent-voltage measurement combines both I-V measurement and the study of light interaction affecting carrier transport. It specifically focuses on the relationship between the voltage applied across a sample and the resulting photocurrent generated by light irradiation. The sample can act as a photoconductor or photodetector, that converts light into electrical signal.

In this study, to perform photocurrent-voltage measurements on the InAs QD samples and GaAs buffer layer sample, electrodes with ohmic contacts were created on top of the GaAs capping layer. A mask pattern as shown in Figure 3.7 was formed by photolithography process to create electrodes. AuGe and Au was deposited on the patterned electrodes by metal evaporation, and unnecessary parts were removed along

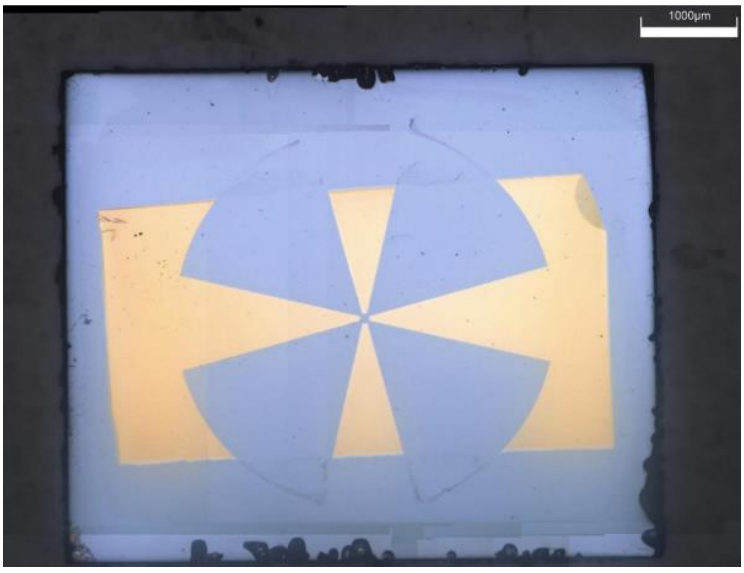

Figure 3.7 AuGe electrodes on sample for photocurrent-voltage measurement.

with the resist by lift-off. Annealing was then performed to diffuse Ge into the GaAs, creating an n+ region and achieving ohmic contact. Finally, wires were fixed to each electrode using Indium and IC tape for wiring.

3.4.1. Photolithography

Photolithography was used to create the desired patterns on the samples for photocurrent-voltage measurement. The photolithography process of depositing electrodes on sample is shown in Figure 3.8. AZ5218-E was used as the resist, and AZ300MIF was used as the developer. First, the resist was applied by spin coating at 4000 rpm for 30 seconds to achieve a thickness of approximately 2 μm. Next, a pre-bake was performed in an oven set to 100 °C for 60 seconds. After the pre-bake, the sample was placed in a mask aligner and brought into contact with the mask for an initial exposure of 6 seconds under ultraviolet light. The sample was then returned to the oven for a post-exposure bake at 120°C for 90 seconds. Final exposure on the sample was performed for 18 seconds without mask. The sample was then developed in developer for 30 seconds, rinsed with DI water and lastly underwent a post-bake at 120 °C for 120 seconds.

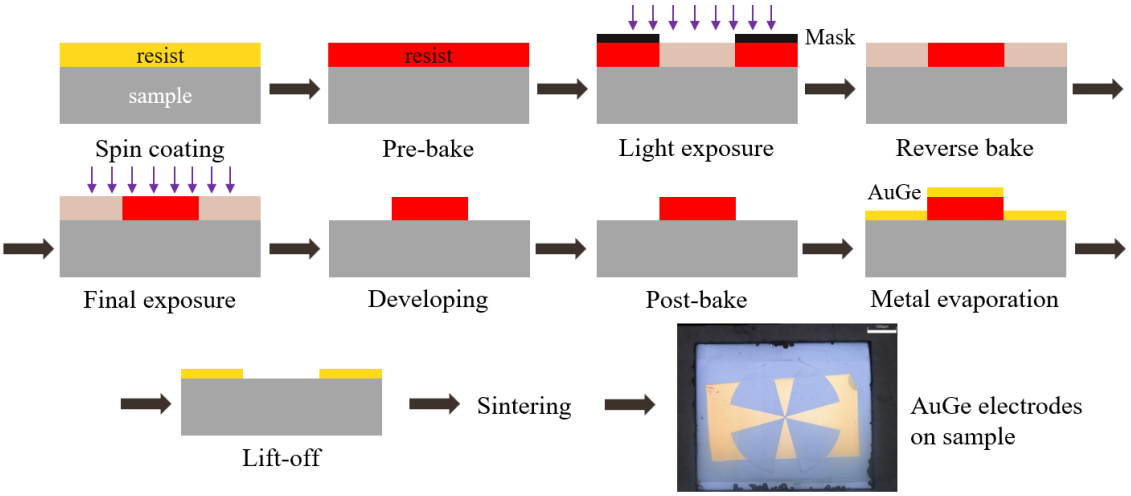

Figure 3.8 Photolithography process for depositing electrodes on sample.

3.4.2. Metal Evaporation and Lift-Off

After photolithography process, the electrodes were deposited on sample using the resistance-heated evaporation system (Sanyu Electron SVC-700TMSG) to heat the AuGe and Au sources. The mass ratio of the sources was Au:Ge = 88:12, using approximately 1 gram of the source. This mass ratio corresponded to the composition that evaporates at the lowest temperature. Samples then undergo annealing process where Ge diffuses into the GaAs side to form an n+ region, resulting in a very thin Schottky contact layer and achieving ohmic contact. The separation distance between electrodes is 120 μm for UHD QD sample, 107.2 μm for LD QD sample, and 106.2 μm for GaAs buffer layer sample.

After the process of electrode deposition, the sample was immersed in acetone to remove the resist, leaving only the electrode pattern. After the resist was removed, the sample was rinsed with DI water.

3.4.3. Sintering

With the Au/AuGe deposited electrodes, the sample was ready to undergo sintering process in a thermal annealing system. Before sintering, the pressure was reduced to below $10^{-3}\ Torr$ (low vacuum condition) using rotary pump to prevent oxidation of the sample and contact with impurities. The temperature was then increased at a rate of 13.2 °C/min until 350 °C was reached, followed by continuous annealing for 12 minutes to diffuse Ge onto the sample surface, forming an n+ region.

3.4.4. Measurement Setup

The photocurrent-voltage measurement was conducted by connecting the sample to the PL spectrum measurement system. A source meter (Keithley-2400) was used to

connect the wires and perform the four-terminal measurement method. Laser light from a supercontinuum light source (frequency: 60MHz, period < 100ps) was spectrally dispersed by a spectrometer and irradiated onto the sample with an intensity of 17mW, and at the wavelength of 925 nm. The irradiation diameter was confirmed using a charge-coupled device (CCD) camera, and the light was irradiated between the electrodes for the photocurrent measurement at temperatures ranging from 15 K to 210 K. A range of voltages is applied across the device similar to a standard I-V measurement. At each voltage level, ranging from -5 V to 0 V and from 0 V to 5 Volt, the current flowing through the device was measured. This included both the dark current (current flowing without light) and the photocurrent generated by light irradiation.

3.5. Hall Effect Measurement

The Hall effect causes a voltage to form on a semiconductor in the presence of a magnetic field[50], and it is a powerful tool used to determine whether a semiconductor is p-type or n-type. It also allows for the measurement of carrier concentration and carrier mobility. When a sample is immersed in a magnetic field, the charge carriers are deflected, creating an electric field. The direction of this electric field depends on the sign of the charge carriers, and the polarity of the Hall voltage across the semiconductor reveals this sign. The magnitude of the Hall voltage is dependent on the current, the charge carrier density, and the strength of the magnetic field. Conventionally, the Hall effect is measured using the Lorentz force[44], represented by the right-hand rule:

$$F_m = qv \times B \tag{3.3}$$

Where F_m represents force, q is moving charge, v is the velocity, and B is the magnetic field. However, in this study, we employ the Van der Pauw method[51,52]. This

method can measure the properties of a sample of any arbitrary shape, provided the sample is flat, preferably symmetrical, thickness must be less than the width and length of the sample, and contains no isolated holes. The Van der Pauw method employs a four-point probe placed around the perimeter of the sample to provide an average resistivity measurement, as shown in Figure 3.9. The measurements obtained include the resistivity of the material, the carrier type, the majority carrier concentration, Hall coefficient, and the mobility of the majority carrier.

The Van der Pauw determine the resistivity of a sample by measuring its resistance in various configurations. The procedure begins by selecting one side of the sample (using terminals 1 and 2) as the current injection points, while the opposite side (terminals 3 and 4) serves as the voltage measurement points[53]. The current I_S is applied, and the resistance across these terminals is measured, recording this as the initial resistance R_0 along with its standard deviation SD_0. Next, the same measurement is performed with the current direction reversed (negative current), producing a resistance R_1 and standard deviation SD_1. After this, the roles of the current and voltage terminals are swapped—

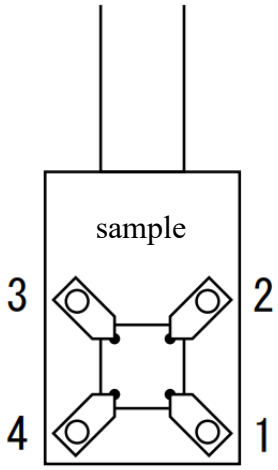

Figure 3.9 Sample placement on a sample holder, employing the Van der Pauw measurement method[53].

now injecting current through terminals 3 and 4, and measuring the voltage across terminals 1 and 2. This configuration yields a new resistance value R_2 and standard deviation SD_2. The process is repeated with the current direction reversed, resulting in a resistance R_3 and standard deviation SD_3.

The procedure then shifts to measuring resistance in an orthogonal direction to the initial setup. The current is injected through a different pair of terminals (2 and 3), with the voltage measured across the opposite terminals (4 and 1). This provides a resistance value R_4 and standard deviation SD_4. The steps previously described by measuring resistance with reversed current and swapped terminals are then repeated in this orthogonal direction, producing additional resistance values R_5, R_6, and R_7 along with their respective standard deviations SD_5, SD_6, and SD_7.

The average resistance values in two perpendicular directions, R_a and R_b are calculated by:

$$R_a = \frac{1}{4} \cdot (R_0 + R_1 + R_2 + R_3) \tag{3.4}$$

$$R_b = \frac{1}{4} \cdot (R_4 + R_5 + R_6 + R_7) \tag{3.5}$$

The directional ratio r is then calculated to be equal to or greater than 1, ensuring the correct relationship between R_a and R_b.

$$r = \left|\frac{R_a}{R_b}\right| \; or = \left|\frac{R_b}{R_a}\right| \quad (\geq 1) \tag{3.6}$$

Next, the balance factor $f(r)$ or known as the "F value" is determined to ensure the consistency of the measurement.

$$\cosh\left(\frac{r-1}{r+1} \cdot \frac{\ln 2}{f(r)}\right) = \frac{1}{2} \cdot \exp\left(\frac{\ln 2}{f(r)}\right) \quad 0 \leq f(r) \leq 1 \tag{3.7}$$

With R_a and R_b established, the overall average resistance R_{ab} is computed, along with the standard deviation SD.

$$R_{ab} = \frac{R_a + R_b}{2} \tag{3.8}$$

$$SD = \sqrt{\frac{SD_0^2 + SD_1^2 + SD_2^2 + SD_3^2 + SD_4^2 + SD_5^2 + SD_6^2 + SD_7^2}{8}} \tag{3.9}$$

Using these values, the resistivity ρ and sheet resistance R_{sheet} are calculated, factoring in the sample's thickness t. Additionally, the error ratio Er is determined as a percentage, reflecting the precision of the measurements.

$$\rho = \frac{\pi \cdot t}{\ln 2} \cdot R_{ab} \cdot f(r) \quad [\Omega \cdot cm] \tag{3.10}$$

$$R_{sheet} = \frac{\pi}{\ln 2} \cdot R_{ab} \cdot f(r) = \frac{\rho}{t} \quad [\Omega] \tag{3.11}$$

$$Er = \frac{SD}{R_{ab}} \times 100 \quad [\%] \tag{3.12}$$

To determine the DC magnetic field Hall coefficient measurement, a magnetic field B is applied, and the system is allowed to stabilize. This stabilization is monitored by checking the output current of the electromagnet's power supply at regular intervals, ensuring it remains within the set tolerance range. Next, the measurement is performed using the sample's diagonal electrodes (terminals 1 to 3) as the current input terminals, and the orthogonal diagonal (terminals 2 to 4) as the voltage measurement terminals. The resulting Hall resistance R_m is recorded as R_0, with its standard deviation SD_R recorded as SD_0. The same configuration is then used with a reversed current direction, and the process is repeated to obtain R_2 and SD_2.

The procedure is then repeated with terminals 2 to 4 as the current input and terminals 1 to 3 as the voltage measurement terminals. The Hall resistance R_m is recorded as R_4, and standard deviation SD_4. Again, a reversed current measurement is performed to obtain R_6 and SD_6. After these measurements, the magnetic field is reversed, and the system is once again allowed to stabilize. With the magnetic field reversed ($-B$), the

measurements are repeated exactly as before. This includes the initial configuration to obtain R_1 and SD_1, and the reversed current direction measurements to obtain R_3, R_5, and R_7 along with their respective standard deviations SD_3, SD_5, and SD_7.

For each direction of the current, the average Hall resistances, R_c and R_d are calculated along with their standard deviations SD_c and SD_d.

$$R_c = \frac{1}{4} \cdot (R_0 - R_1 + R_2 - R_3) \tag{3.13}$$

$$R_d = \frac{1}{4} \cdot (R_4 - R_5 + R_6 - R_7) \tag{3.14}$$

$$SD_c = \sqrt{\frac{SD_0^2 + SD_1^2 + SD_2^2 + SD_3^2}{4}} \tag{3.15}$$

$$SD_d = \sqrt{\frac{SD_4^2 + SD_5^2 + SD_6^2 + SD_7^2}{4}} \tag{3.16}$$

The overall average Hall resistance, R_{cd} is then determined by averaging the resistances R_c and R_d. The standard deviation for this combined resistance, SD_{cd}, is calculated to account for the combined uncertainties.

$$R_{cd} = \frac{R_c + R_d}{2} \tag{3.17}$$

$$SD_{cd} = \sqrt{\frac{SD_c^2 + SD_d^2}{2}} \tag{3.18}$$

Finally, using the absolute value of the overall average Hall resistance R_{cd}, key parameters such as the Hall coefficient R_H, carrier concentration CC, and mobility MO are calculated.

$$RH = \frac{t}{B} \cdot \frac{V_{HALL}}{I_s} \times 10^4 = \frac{t}{B} \cdot |R_{cd}| \times 10^4 \quad [cm^3/C] \tag{3.19}$$

$$CC = \frac{1}{RH \cdot e} = \frac{B}{t \cdot |R_{cd}|} \cdot \frac{1}{1.6 \times 10^{-15}} \quad [cm^{-3}] \tag{3.20}$$

$$MO = \frac{RH}{\rho} = \frac{|R_{cd}|}{R_{sheet} \cdot B} \times 10^4 \quad [cm^2/V \cdot s] \tag{3.21}$$

3.5.1. Sample Preparation

In this procedure, Indium electrodes are fabricated on the four corners of an MBE-grown sample to establish ohmic contacts. To minimize contact resistance and ensure a uniform ohmic contact, the Indium electrodes are carefully shaped into small, hemispherical forms. The shaped Indium electrodes are then attached to the four corners of the MBE-grown sample as shown in Figure 3.10. This process requires precise positioning and secure attachment to ensure proper electrical connection. To further enhance the ohmic contact characteristics, the sample with the attached Indium electrodes undergoes sintering process. This involves placing the sample inside a uniform heating oven and subjecting it to a specific temperature and time profile.

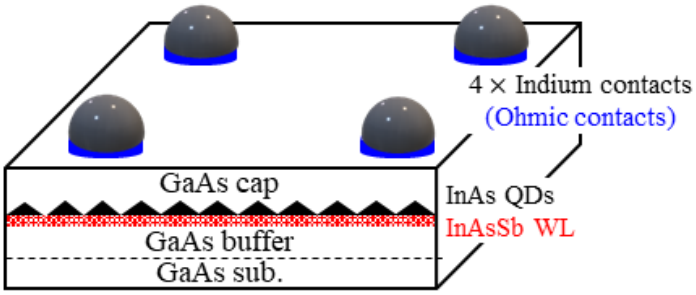

Figure 3.10 Placement of Indium contacts at the four corners of sample for Van der Pauw measurement.

3.5.2. Setup for Hall Effect Measurements

The sample is securely attached to the sample stage holder by four electrodes. The cryostat, equipped with liquid nitrogen, is utilized to cool the sample down to a temperature of 78 K. For temperature-dependent measurement, a temperature controller

connected to a heater mounted on the sample stage allows for precise control of the sample temperature, ranging from 78 K to 400 K. A multimeter is used for voltage and current measurements; a source meter is used to provide current to flow through the sample; switching system allows automatic selecting and switching of different contact points on the sample for measurements in various configurations; electromagnetic current source generates magnetic field that is perpendicular to sample surface. These components work together to measure the Hall voltage and resistance of the sample as shown in the setup of Hall effect measurement in Figure 3.11.

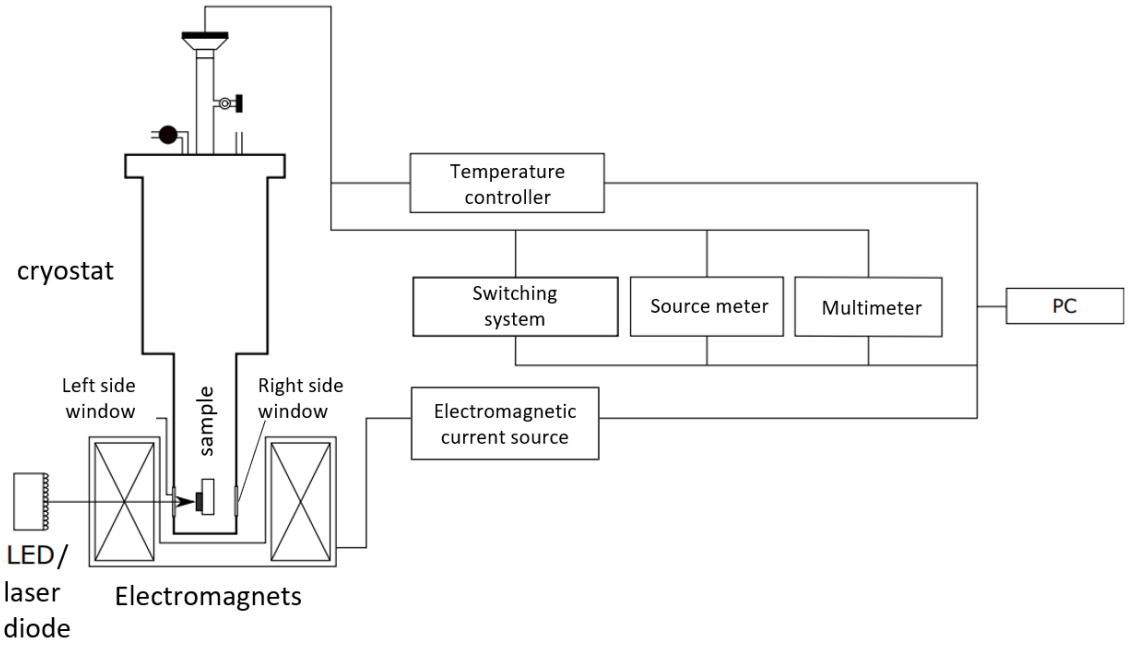

Figure 3.11 Setup for Hall effect measurements[91].

An optical window integrated into the measurement system enables the introduction of light from an external source, providing a uniform light source for the sample. Two types of light source are used in the measurement, which are LED array and laser diode. In initial stage of Hall effect measurement, a 1050 nm LED array was used as light source (a standard setup in Hall effect experiment), as shown in Figure 3.12. Due to the wider beam and incoherent light emitted by the LED array, data analysis for QDs was

challenging. Therefore, a self-customized setup replacing LED array with laser diode of 980 nm excitation wavelength is used at a later stage of Hall effect measurement, as shown in Figure 3.13. The power detector measured approximately 20% less laser power than was emitted by the laser diode $(1\,mW \approx 0.803\,mW)$. This is likely due to the presence of transparent glasses on both sides of the windows, which may have filtered some of the light before it reached the sensor. The magnetic field for Hall measurements was set at 0.35 Tesla, and the constant current was $1 \times 10^{-7}\,A$.

(a) (b) (c)

Figure 3.12 Setup for LED light source. (a) LED array is placed at the window of the system where light is irradiated perpendicularly on the sample. (b) Top view of LED array. (c) DC power supply for LED array supplying constant voltage of 10 V.

(a) (b) (c)

Figure 3.13 Setup for 980 nm laser diode light source. (a) Laser diode is placed at the window (left) of the system, supported by adjustable holder. (b) The sensor of the power detector detects the irradiated laser light at the opposite window (right) of the system. (c) The power detector displays the detected laser power on its screen (up), and the laser power emitted from laser diode is shown on the screen of remote control (down). Emitted laser power of 1 mW is detected as 0.803 mW.

3.6. Chapter Summary

The chapter details the comprehensive process of preparing, growing, and analyzing high-quality GaAs and InAs quantum dot samples using MBE and various characterization techniques. A GaAs buffer layer is grown at 590°C, followed by the deposition of an InAsSb WL and InAs QDs at 460°C, with careful flux control and monitoring via RHEED. The QDs are capped with a GaAs layer for PL measurements, and the sample undergoes rapid cooling and unloading from MBE chamber. Subsequent analyses include AFM for surface characterization, macro-PL and micro-PL for optical properties, photocurrent-voltage measurements and Hall effect measurements for electronic properties, with electrodes created through photolithography and metal evaporation, followed by sintering the Indium contacts pasted on the sample to form ohmic contacts.

Chapter 4. Abnormal Photoluminescence Properties of InAs/InAsSb In-Plane UHD QDs

4.1. Introduction

The interaction of electronic states between adjacent QDs is interesting for the development of new physical properties and device applications. When the interdot separation distance becomes small enough for the electron wavefunctions to overlap, the electronic interaction occurs through the tunneling coupling between adjacent QDs. In addition, if adjacent QDs have the same energy level and their electronic states resonate, the energy states of coupled QDs separate into a bonding state and an antibonding state. It is called electronic strong coupling. Assembled QDs with strong coupling will exhibit different optoelectronic properties from assembled isolated QDs. The electronic interactions of vertically multi-stacked QDs could be controlled by the separation distance between stacked dots and have been widely studied[54,55]. According to the previous reports[56,57], the electronic state in strongly coupled QDs became delocalized as the interdot spacing is less than about 10 nm. While there have been reports on theoretical studies regarding in-plane strong coupling between adjacent QDs[27–29], there are fewer experimental studies on self-assembled QDs due to low QD density and large inhomogeneous broadening of the QD size. In this study, the in-plane UHD QDs of InAs/InAsSb grown epitaxially on GaAs substrates were successfully fabricated using MBE. These in-plane UHD QDs were closely aligned to $< 4\,nm$ interdot separation distances, and the highest QD density of $0.8 - 1 \times 10^{12}\ cm^{-2}$ was achieved. The ultrahigh QD density is one of the key factors in realizing in-plane electronic strong coupling between neighboring QDs and forming in-plane energy minibands in the QD

layer. In recent study, we have demonstrated in-plane miniband formation due to the strong coupling in ground states (GS) of InAs/InAsSb UHD QDs.[33]

In this study, we observed abnormal PL properties of InAs/InAsSb UHD QDs on a GaAs substrate compared to a sample of InAs high density (HD) QDs and a conventional sample of InAs low density (LD) QDs. The results from HD QDs were used to support the evidence of strong coupling observed in UHD QDs, as ultrahigh density QD samples are challenging to fabricate and produce, with references to such high density QDs being rare. From these temperature-dependent PL properties, including spectrum, decay time, intensity, and full width at half maximum (FWHM), we comprehensively discuss the phenomenon of strong coupling not only in ground states (GS) but also in excited states (ES) of InAs/InAsSb UHD QDs.

4.2. Temperature-Dependent Homogeneous Broadening of Single QD

Several studies have explored how phonon interactions influence the temperature dependence of the exciton's homogeneous linewidth, Γ in QDs. While QDs possess discrete energy levels due to three-dimensional carrier confinement, the coupling to acoustic and optical phonons is expected to be weaker compared to semiconductor quantum wells (QWs). For single InAs QDs, the homogeneous broadening of the linewidth has been analyzed using a Lorentzian profile. This broadening originates from thermoactivated processes involving acoustic and optical phonons, which can be described by the standard equation for thermoactivated broadening[58]:

$$\Gamma(T) - \Gamma(T=0) = \gamma_{ac}T + \gamma_{op}\frac{1}{e^{\frac{\hbar\omega_{LO}}{kT}} - 1} \tag{4.1}$$

Where the first term describes the acoustic phonon scattering, while the second term describes scattering with optical phonons. Studies have shown that phonon-assisted

broadening occurs not only in the ground state exciton of single QDs but also in their excited states. In the study[59], a linear increase in the homogeneous broadening of single InAs/GaAs QDs at excited states as the temperature rose from 10 K to 40 K. This behavior is attributed to the dominant interaction with acoustic phonons (optical phonons are omitted) at these low temperatures.

At higher temperatures (above ~60 K), thermal excitation of optical phonons becomes significant and influences on exciton scattering. This is where a strong increase of the homogeneous linewidth is observed. It was reported that at lower temperatures, the number of states within the QD confinement potential that can be reached from the exciton ground state via phonon scattering is limited. As a result, the broadening of the linewidth with temperature is weaker. Conversely, at higher temperatures, the number of available states within the QD for scattering increases significantly, opening up more scattering channels. This ultimately leads to a faster rise in the homogeneous linewidth as the temperature approaches room temperature[60]. To study the temperature dependence of light emission from a single InAs QD, our research group performed PL measurements between 5 K and 80 K. A Distributed Bragg Reflector (DBR) structure was incorporated into the sample design to improve the efficiency of light extraction from the QD. The temperature dependence of the PL spectra for single InAs QD from Yamaguchi laboratory is shown in Figure 4.1(a). Similar observations of acoustic phonon sidebands (broadening in the emission lines) are reported in a reference journal paper[61] as shown in Figure 4.1(b). These sidebands become dominant features of the QD PL spectrum at 80 K, where the QD line recovers a quasi-Lorentzian line shape. The inset of Figure 4.1(b) depicts the change in the homogeneous linewidth, which is the difference between the central Lorentzian line fit and the actual data. This behavior aligns well with the temperature-

dependent homogeneous linewidth observed for the single InAs QD in Figure 4.2. The agreement between the experimental data and the thermoactivated broadening equation

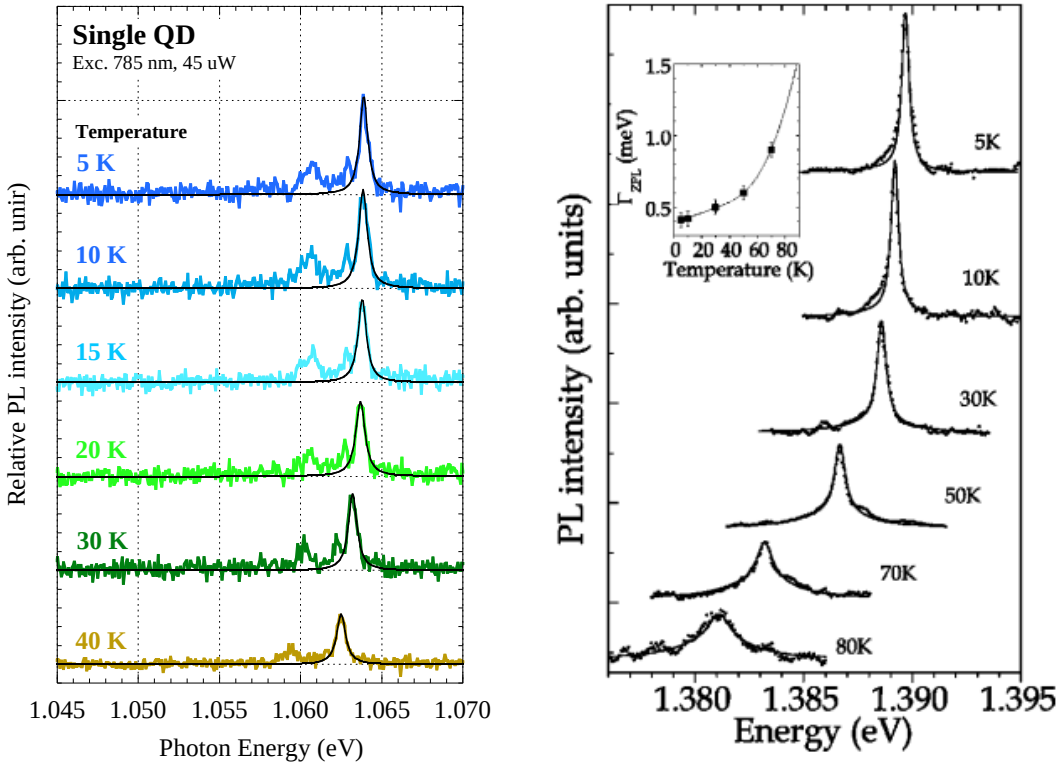

Figure 4.1 Temperature-dependent PL spectra of single QDs from (a) Yamaguchi laboratory, and (b) reference journal paper[61].

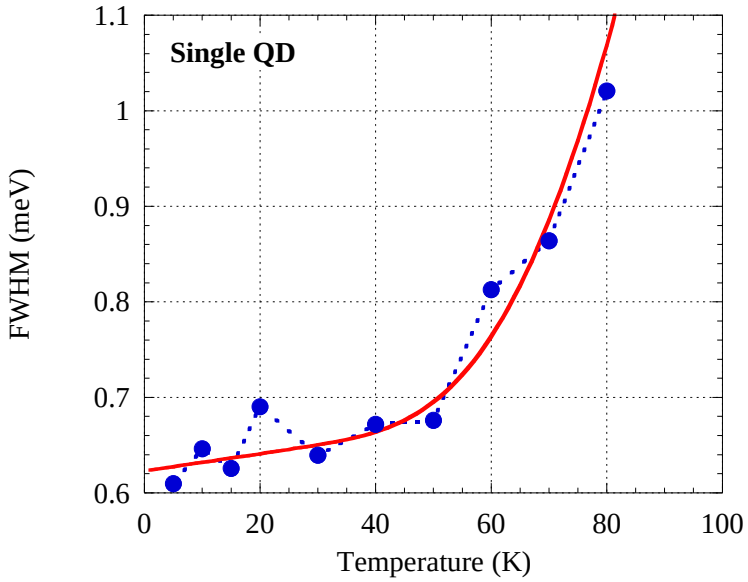

Figure 4.2 Temperature-dependent PL homogeneous linewidth of single InAs QD[33]. Red solid line fitted according to equation 2.1.

(represented by the red solid line in Figure 4.2) suggests that the observed increase in homogeneous broadening with temperature arises from thermoactivated processes involving acoustic and optical phonons[61].

4.3. Coupling of Energy States in Quantum Dots

Carriers can move within a QD array through tunneling. Carrier motion can be categorized into two types: incoherent and coherent, based on the tunneling mechanism. Incoherent motion is primarily controlled by non-resonant tunneling, whereas coherent motion occurs through coherent tunneling, such as in a Bloch wave[62]. Coherent carrier motion involves the formation of extended states or minibands. Regardless of whether carrier motion is coherent or not, it is expected to result in a red shift of the PL peak energy and a reduction in PL linewidth. In incoherent carrier motion, the mechanism involves non-resonant tunneling of carriers from smaller to larger dots, requiring the involvement of phonons or other carriers and exhibiting a relatively low tunneling rate. From the study by Tackeuchi et. al., a carrier could tunnel approximately 0.9 times during its lifetime in a coupled QD array, which indicates that the carriers' mean free path is limited to one or a few dots, with no significant red shift or linewidth narrowing anticipated[63].

From the study by M. Bayer et al., the coupling and entangling of quantum states in a pair of vertically aligned, self-assembled InAs QDs were verified by the interaction-induced energy splitting of s-shell states, depending on the separation distance between the dots[56]. Similarly, in the case of InAs QDs in this study, the height of the quantum dot is significantly smaller than the radius, resulting in the wave function of a carrier in a dot being well localized along the growth direction. As shown in Figure 4.3, at low excitation

power and a low temperature of 60 K, the luminescence of single QD molecules showed the splitting of s-shell emission into the entangled exciton states |a'> and |b'>, which are eigenstates of the electron-hole Hamiltonian, when the dot distance was 8 nm. Further reduction of the quantum dot separation caused the emission line |a'> to shift significantly to lower energies, while the energy of the peak |b'> remained almost constant, leading to an increase in their splitting to more than 30 meV when the dot distance became smaller than 5 nm. This behaviour suggests energy level splitting due to dot coupling and was in qualitative agreement with expectations from Hamiltonian model calculations.

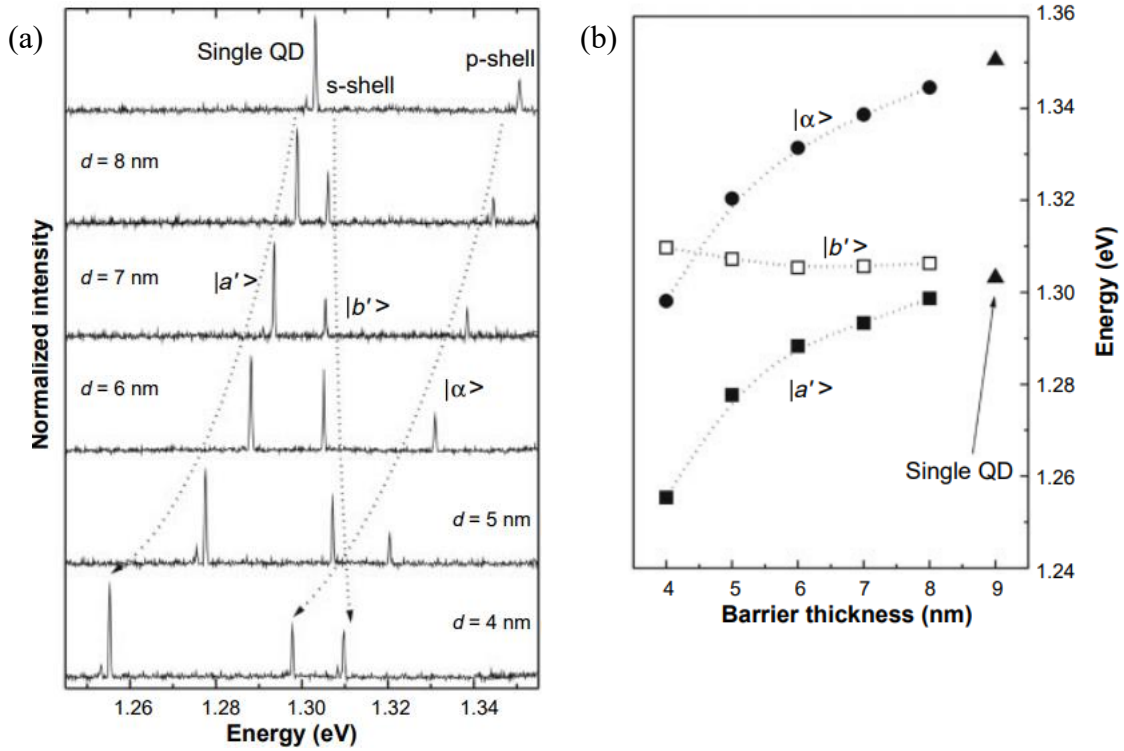

Figure 4.3 The luminescence of single QD molecules showing the splitting of s-shell emission as the separation distance between dots decreases[56].

Another study by K. Goshima et al. introduces a strong quantum mechanical coupling between stacked InGaAs QDs with small interdot spacing. Their numerical calculations show that the degenerate state of the electron wave function splits into bonding and antibonding states when the interdot spacing is less than 10 nm, while the degenerate state

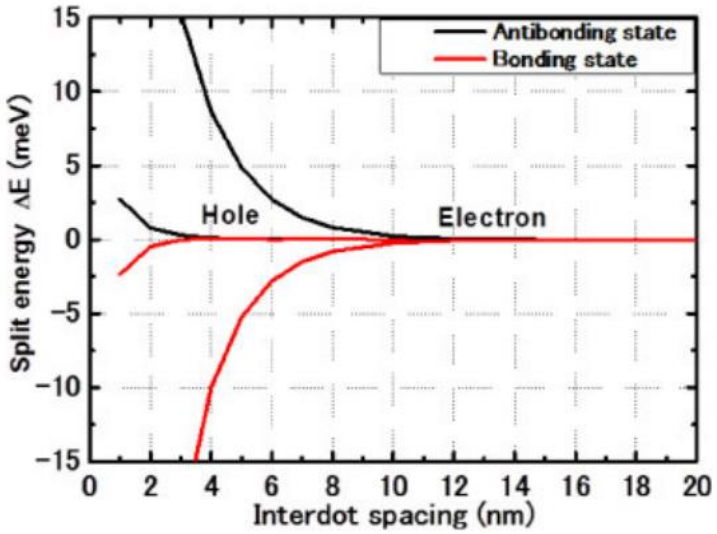

Figure 4.4 The degenerate state of the electron wave function splits into bonding and antibonding states when the interdot spacing is less than 10 nm, while the degenerate state of holes splits at an interdot spacing of less than 4 nm[57].

of holes splits at an interdot spacing of less than 4 nm, as shown in Figure 4.4. These findings indicate a transition of the wave function from localization to delocalization due to quantum mechanical coupling between QDs, which is the primary mechanism behind miniband formation[57]. The authors also define minibands as formed from the split energy difference exceeding 0.1 meV. Experimental results corroborate these findings, showing that a small interdot spacing of 3.5 nm exhibits coupling and miniband properties, characterized by minimal differences in Transverse Electric mode and Transverse Magnetic mode in polarized PL spectra, lower activation energy, and broader and less distinct transition states in PL excitation.

Based on the studies regarding coupling of energy states between small interdot separation of QDs, the model of strong coupling of InAs QDs in this study was defined. Figure 4.5(a) illustrates the schematic diagrams of temperature dependent energy states of GS, ES and the energy bandgap of an isolated QD. At low temperatures, an isolated QD has a very narrow energy state with minimal homogeneous broadening. However, as the temperature increases, the homogeneous broadening of energy states increases, leading to the spreading out of the QD energy state. While the bandgap energy decreases with increasing temperature, this phenomenon is referred to as Varshni shift[64]. Figure 4.5(b) illustrates the schematic diagram of quantum dots' states and the degree of homogeneous broadenings for two QDs (QD1 and QD2) under low temperature and high temperature. E_0 corresponds to the exciton emission energies of the QDs, which aligns with the temperature dependence of the bandgap energy E_g, following the Varshni empirical formula. At low temperature (T_L), QD states are discrete and homogeneous broadening ΔE is minimal, therefore QD energy levels between adjacent QDs do not overlap and no significant electronic coupling between individual QD states. Conversely,

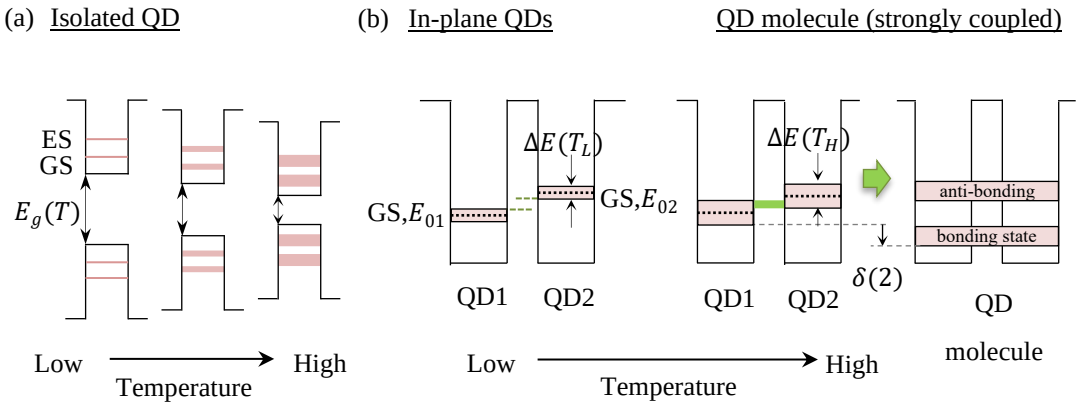

Figure 4.5 Schematic diagram of (a) temperature dependent homogeneous broadening of energy states and the shrinkage of the energy bandgap of an isolated QD, and (b) the strong coupling of two in-plane QDs as temperature increases, resulting in the formation of QD molecule, exciton state splitting, and a reduction in the QD minimum energy by $\delta(2)$.

at higher temperature (T_H), the widened homogeneous broadening causes the matching and overlapping between the states of QD1 and QD2, resulting in electronically strong coupling between both QDs (formation of QD molecule). When a QD molecule is formed, the exciton state splits into bonding and anti-bonding states. When the energy level of QD1 is lower than that of QD2 ($E_{01} < E_{02}$), the minimum energy of the QD is further reduced to the bonding state minimum energy. Therefore, it is predicted that the PL spectrum shifts toward low energy side due to the strong coupling. When multiple adjacent QDs couple strongly, an energy miniband is formed. In the context of InAs QDs, given the effective mass of hole is heavier than the electron, holes are individually confined in the valence band and do not have interactions with the neighboring ones.

4.4. Carrier Transport between In-Plane Quantum Dots

Under varying temperature conditions, the carriers in QD ensemble transition from a random, nonuniform carrier distribution at low temperatures to a more uniform, equilibrium-like distribution at higher temperatures, where the carriers reach a common Fermi level[65]. At low temperatures, the carriers are in a nonequilibrium state. Their distribution across the QDs is random, and the system has not yet reached thermal equilibrium. This randomness occurs due to insufficient energy available to the carriers, causing them to become confined to specific QDs without an even distribution. In contrast, at higher temperatures, the carriers gain enough energy to move more freely between the QDs. The carriers in QD ensemble transition to a quasiequilibrium state, where the carrier distribution is no longer random. Instead, the carriers share a common Fermi level, where the energy distribution of the carriers becomes more uniform throughout the QD ensemble, reflecting thermal equilibrium. This transition of carrier distribution is

facilitated by the temperature-activated coupling between QDs, provided by the wetting layer states linking the dots. Therefore, wetting layer not only plays an important role in achieving high densities of QDs, it also aids in analyzing the temperature-dependent carrier dynamics in QD ensemble.

The PL of S-K growth type QD ensemble typically exhibits an abnormal temperature dependence behaviour. This includes a significant temperature-induced band gap shrinking, which can eventually become sigmoidal, as plotted in Figure 4.6 for UHD QDs, and a temperature-driven reduction in the PL FWHM. This phenomenon is based on the temperature-dependent carrier dynamics explained above, where various factors should be taken into account such as the QD size distribution, processes like carrier capture, relaxation, and retrapping. The temperature-dependent carrier distribution that can be determined in the PL spectra can be broadly categorized into three stages. At low temperatures, carriers are distributed randomly among the QDs. The PL spectrum symbolizes the distribution of the QD state energies across the ensemble. As the temperature rises, the PL spectrum shifts to lower energies, mirroring the behavior of the bulk band-gap energy, while FWHM remains unchanged. With increasing temperature, carriers are thermally excited into higher energy states and subsequently redistributed among the QDs. Carriers excited from smaller QDs, which have higher energies are preferentially transferred to larger QDs with lower energies. This results in a significant redshift of the PL peak energy and a reduction in FWHM. At higher temperatures, carriers in deeper energy QDs are increasingly excited. The difference in excitation probabilities between carriers from higher-energy and lower-energy QDs decreases. Consequently, the PL peak energy redshift begins to align more closely with the bulk band-gap energy trend (Varshni shift), and the FWHM increases. If tunneling were the primary mechanism

responsible for carrier redistribution, the PL spectra would exhibit a different behavior.

The PL minimum energy for UHD QDs and LD QDs were plotted in Figure 4.7 as a function of temperature, with Varshni's empirical relationship for the InAs bandgap represented by black dotted lines. The PL minimum energy originates from the largest QDs, where carriers consistently occupy their GSs. Therefore, the PL minimum energy value is less sensitive to the carrier escape and redistribution. Consequently, in the absence of strong coupling between adjacent QDs, the temperature dependence of the PL minimum energy aligns with the Varshni shift. The inset in Figure 4.7 illustrates the determination of PL minimum energy, identified from the rising point of the lower energy side of a PL spectrum. For LD QDs, the PL minimum energy consistently shifted to lower energy levels along the Varshni's line, regardless of temperature increment. This behavior is attributed to the longer separation distance between adjacent large QDs, which prevents electron tunneling and strong coupling. Clear evidence of three distinct regions of lower energy shifting in the PL minimum energy of UHD QDs is presented. In region I (15 K – 100 K), the PL minimum energy consistently shifted along the upper Varshni's line. In

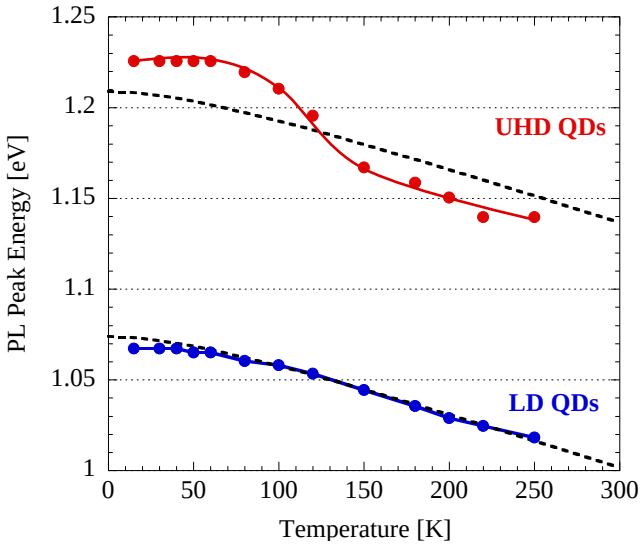

Figure 4.6 PL peak energy of UHD QDs and LD QDs. Black dotted lines represent the Varshni shifts of the InAs bandgap.

region II (100 K – 200 K), a substantial drop in energy was observed, deviating from the upper Varshni's line. Finally, in region III (200 K – 250 K), the PL minimum energy reverted to following the lower Varshni's line.

In region I, the majority of carriers in UHD QDs are fully confined, allowing for carrier transport via tunneling as previously reported[21]. Consequently, the PL minimum energy of the largest QDs aligns with the upper Varshni shift line. However, region II, the deviation of the PL minimum energy from the upper Varshni shift indicates the lowering of the GS levels of the largest QDs due to the strong coupling[33]. With increasing temperature, the number of strongly coupled QDs increases, leading to a further decrease in the PL minimum energy. Moving to region III, the PL minimum energy following the lower Varshni's line indicates saturation in miniband formation resulting from strong coupling. This suggests that the lowering of the lowest energy level due to strong coupling ceases as the number of strongly coupled QDs saturates. This unique temperature

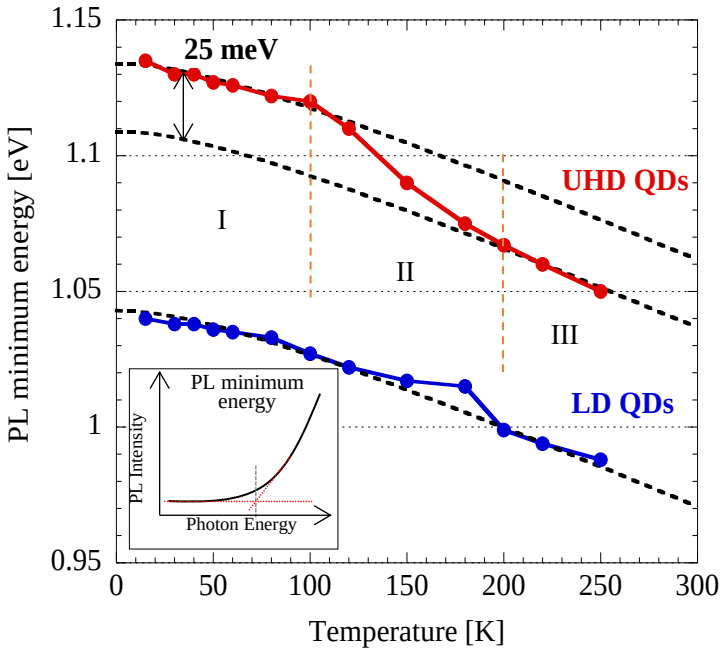

Figure 4.7 PL minimum energy of UHD QDs and LD QDs. Black dotted lines represent the Varshni shifts of the InAs bandgap. The inset showed the determination of PL minimum energy, from the rising point of the lower energy side of PL spectrum.

dependence of PL minimum energy can be explained by the above scenario, even in the presence of carrier escape and redistribution. Given that the interdot spacings between UHD QDs are much smaller than those of LD QDs, the exciton states of individual QDs broaden at high temperatures, leading to overlapping of neighboring QD states. As reported, the strong coupling occurs in the electron wavefunction at interdot distance of less than 10 nm, and in the hole wavefunction at less than 4 nm.

4.5. Related Studies of Strongly Coupled Bands in Ensemble QDs

The report by Mazur et al. identifies the crossed transitions from the wetting layer (WL) valence band to the electron ground states of a self-assembled InGaAs/GaAs QD ensemble[66]. The PL measurements were conducted over a variable temperature range of 8–300 K. Continuous-wave PL excitation was provided by a 532 nm laser. The ensemble was characterized by an average QD diameter of 40 nm, a height of 8 nm, and a density of $4 \times 10^{10}\ cm^{-2}$. Evidence of continuum states in the QDs was shown in two key results. First, the appearance of a sub-peak at higher energy on the PL spectra, under very low excitation density, was attributed to the crossed transitions between the WL valence band and the QD hole states, indicating a coupling between these two states to form a continuous state. This sub-peak became more pronounced as the excitation densities decreased below those required for WL and QD excitation transitions.

Second, abnormal PL results were observed: the PL peak shifted significantly by 50 meV towards lower energies, the integral intensity of the PL decreased non-monotonically, and the FWHM value exhibited two minima with increasing temperature. As shown in Figure 4.8, these PL results shared similarities with findings of HD QDs and UHD QDs from our study at high excitation power, where a shift of the spectra to lower energies, a decrease in PL integral intensity, and a reduction in PL FWHM were also observed. However, we did not observe the sub-peak demonstrating crossed transitions between WL and QDs, likely due to inhomogeneous broadening and hole confinement in our QDs. It is important to note that Mazur et al. mentioned that if tunneling were present, all carriers would transfer to the largest QDs at low temperatures, leading to an expected increase in FWHM as the temperature rises from 10 to 30 K. We observed this increase in our PL

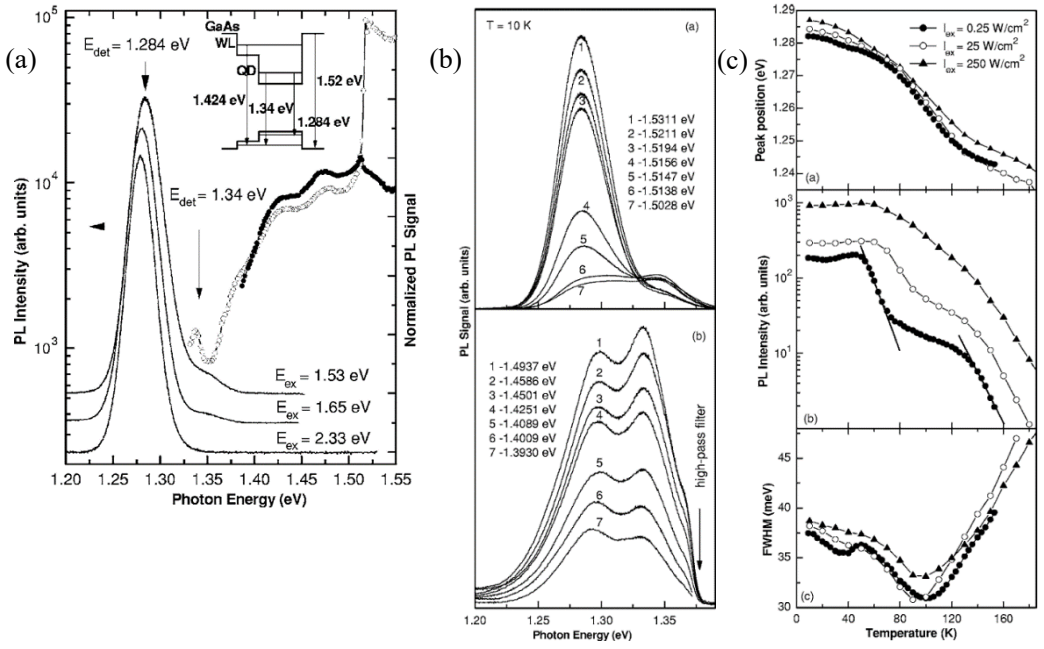

Figure 4.8 (a) Low-temperature PL (T = 10 K) and PLE spectra for different excitation energies. Inset shows schematic of optical transitions derived from the PLE and PL spectra. (b) (Upper panel) PL spectra for below-GaAs barrier excitation. (Lower panel) The low-energy PL band corresponds to QD excitonic transitions, while the high-energy PL band is attributed to crossed transitions. (c) Temperature dependence of the PL peak energy, PL integral intensity, and FWHM[66].

FWHM. This phenomenon suggests that even at the lowest temperatures, carriers are distributed across the entire ensemble of QDs due to a balance between tunneling carrier transfer and carrier excitation. Since interdot tunneling is non-resonant, increasing the temperature promotes carrier transfer through both the tuning of electronic levels in adjacent QDs and the thermal excitation of QD electrons into local continuum states. As the QD electronic wave function becomes more spread out, its overlap with adjacent QDs increases, raising the probability of interdot tunneling. Therefore, the presence of local continuum states near the QDs facilitates interdot carrier transfer through tunneling. Another similar report was from Mano et. al.[67], who discussed about the anomalous temperature-dependent PL spectra of an ensemble of QDs, and the presence of continuous states between WL and QDs that existed but restricted to limited area among QDs.

The study by Zhou et al. investigated the temperature dependence of PL in low-density (A1) and high-density (A2) InAs QD samples[68]. The study examined carrier channels—including coupled bands in QDs, the wetting layer (WL), and continuous states (CS) that exist between QD states and the WL—across different temperature regimes, with a focus on QD density. A rate equation model was used to fit the experimental data. A2 were characterized by an average diameter of 33.4 nm, a height of 1.4 nm, and a density of $1.3 \times 10^{11}\ cm^{-2}$; whereas A1 had an average diameter of 55.4 nm, a height of 9.8 nm, and a density of $6.3 \times 10^{9}\ cm^{-2}$. The samples were mounted in a cryostat that provided temperatures ranging from 15 to 300 K and were excited using a 532 nm solid-state laser. The carrier transfer process related to CS can be described as follows: as the temperature increases, carriers from the QD states can be thermally activated into CS at relatively low temperatures and then transferred to neighboring QDs via LO phonon-assisted tunneling or carrier-carrier scattering. According to the theory of lateral coupling, the minimum

energy of CS decreases as the coupling strength increases, similar to the bonding state in coupled double quantum wells. The CS minimum reflects the strength of lateral coupling through CS.

The differences observed in the PL spectra between A1 and A2, along with the alignment of the fitting results with experimental data, indicate that lateral carrier transfer is dependent on QD density. Due to the higher density in A2, CS-mediated transfer or direct tunneling is expected. These PL results are consistent with findings from our study on LD, HD and UHD QDs, where PL spectra shift to lower energies, the activation energies, and nearly constant PL FWHM were observed for A1, as shown in Figure 4.9. However, the FWHM for A2 differed from that of UHD QDs. The authors noted that the energy difference between the CS minimum and QD states affects FWHM behavior. A decrease in the CS minimum leads to a more pronounced drop in FWHM, indicating stronger CS-mediated carrier transfer. Particularly, when the CS minimum is equal to or lower than the QD states, the FWHM increases in the low-temperature range, which is consistent with the expectations for direct tunneling.

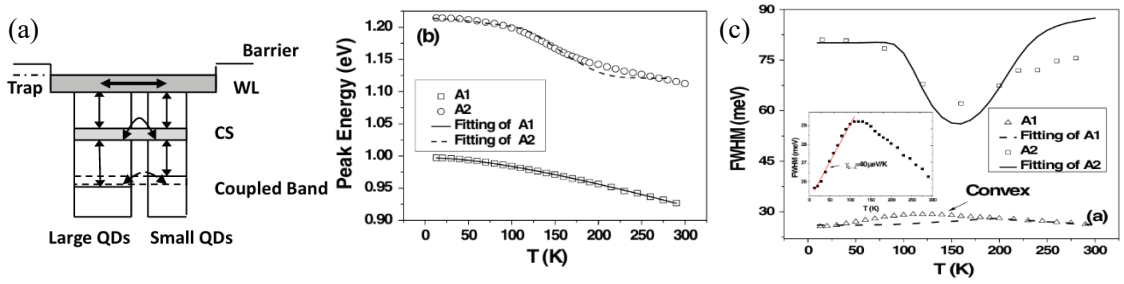

Figure 4.9 (a) Schematic diagram of different carrier channels for a self-assembled QD system. (b) Temperature dependence of PL peak energy of A1 and A2. (c) Temperature dependence of PL FWHM of A1 and A2[68].

To compare the PL properties of coupled ensemble QDs (S-K growth mode) with non-coupled ensemble QDs, Sanguinetti et. al. had come out with a sample of InGaAs/GaAs QD structures without a wetting layer, using a modified MBE growth method called heterogeneous droplet epitaxy (HDE)[65]. No wetting layer was connected to the HDE-QDs, and the electronic wave function was localized around 10 nm in the lateral direction, provided QD width of 30 nm and QD height of 12 nm. Temperature dependences of PL were carried out in 10 – 290 K range, excited with Ar^+ laser and Ti: Sapphire tunable laser. From Figure 4.10, the PL results of a SK-QD reference sample showed the typical anomalous behavior in both plots of PL peak energy and PL FWHM, as described before. On the other hand, the PL peak energy of HDE-QD sample shifted along the GaAs gap temperature-dependent line, with no sign of sigmoidal phenomenon. In addition, PL FWHM of HDE-QD sample increased with temperature due to thermal population of states. The HDE-QD was said to have non-coupled QDs and nonequilibrium states due to the absence of wetting layer, which is fundamental to achieve quasiequilibrium

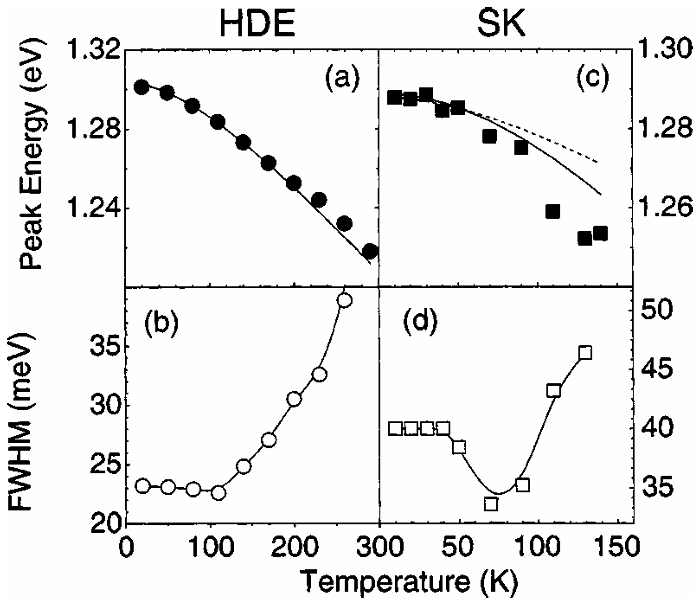

Figure 4.10 Temperature-dependent PL peak energy of (a) HDE-QD, (c) SK-QD, and PL FWHM of (b) HDE-QD and (d) SK-QD[65].

distribution in ensemble of QDs. Although carriers in HDE-QD can move between the dots through continuous barrier states, however it is less efficient that using wetting layer as a coupling channel between QDs. It is because the energy gap between the QD GS and the barrier states is much larger than the energy gap between the QD GS and the wetting layer. This larger energy difference delays the onset of a common equilibrium across the QDs until higher temperatures are reached. In addition, continuous barrier states can act as nonradiative centers that trap carriers and reduce the probabilities of carriers moving from one QD to another. From the article, the presence of the wetting layer extended states offers an efficient coupling channel between the QDs.

4.6. Experimental Setup

Figure 4.11 shows the schematic diagrams of 3 types of InAs QD sample structures of (a) InAs/InAsSb UHD QDs, (b) InAs HD QDs, and (c) InAs LD QDs. All samples were fabricated on semi-insulating GaAs (001) substrates using MBE. For all QD samples, a 200 nm thick non-doped GaAs buffer layer was grown on the GaAs substrate at 580 °C. Subsequently, the InAs UHD QDs were grown on an InAsSb WL at 460 °C. To ensure high uniformity, density and crystal quality of the in-plane UHD QDs, the coalescence and ripening of adjacent QDs were effectively suppressed by a Sb-mediated SK growth mode, thereby incorporating Sb atoms into the WL before the growth of InAs QDs. The supply flux ratio of $\mathrm{Sb}_4/(\mathrm{Sb}_4 + \mathrm{As}_4)$ was kept at 4.7 %. The coverage of the InAsSb WL was 1.25 - 1.30 ML, and the InAs coverage for QDs was 0.95 - 1.0 ML, resulting in a total coverage of 2.2 – 2.3 ML. The growth rate of UHD QDs was 0.035 MLs^{-1}, leading to a QD density of $0.8 - 1 \times 10^{12}\ cm^{-2}$. For the InAs HD QDs and LD QDs, after the growth of the GaAs buffer layer, the temperature was lowered to 500 °C for the growth

of InAs WL and InAs QDs. With a growth rate of 0.089 MLs^{-1} for HD QDs and 0.033 MLs^{-1} for LD QDs, a total InAs coverage of 2.77 ML was achieved for HD QDs and 2.6 ML for LD QDs. The QD density was $3.47 \times 10^{11}\ cm^{-2}$ for HD QDs and $4 \times 10^{10}\ cm^{-2}$ for LD QDs. All QD samples contained of only one QD layer, capped with a 60 nm thick GaAs layer at 460 °C.

The topographies of the InAs QDs were captured using AFM, and the densities of QDs were calculated based on the AFM images as shown in Figure 4.11. It should be noted that the densities of QDs were determined using top-view images obtained from AFM, whereas the size of the QDs, including their height and lateral size, were measured from the line profiles of individual dots. The average height and lateral size of InAs UHD QDs were 1.5 nm and 12 nm, respectively; for InAs HD QDs, they were 2.1 nm and 23 nm; and for InAs LD QDs, they were 10 nm and 29 nm. In the PL measurement, a laser diode with pulse width of 300 ps and repetition frequency of 50 MHz was used. The maximum

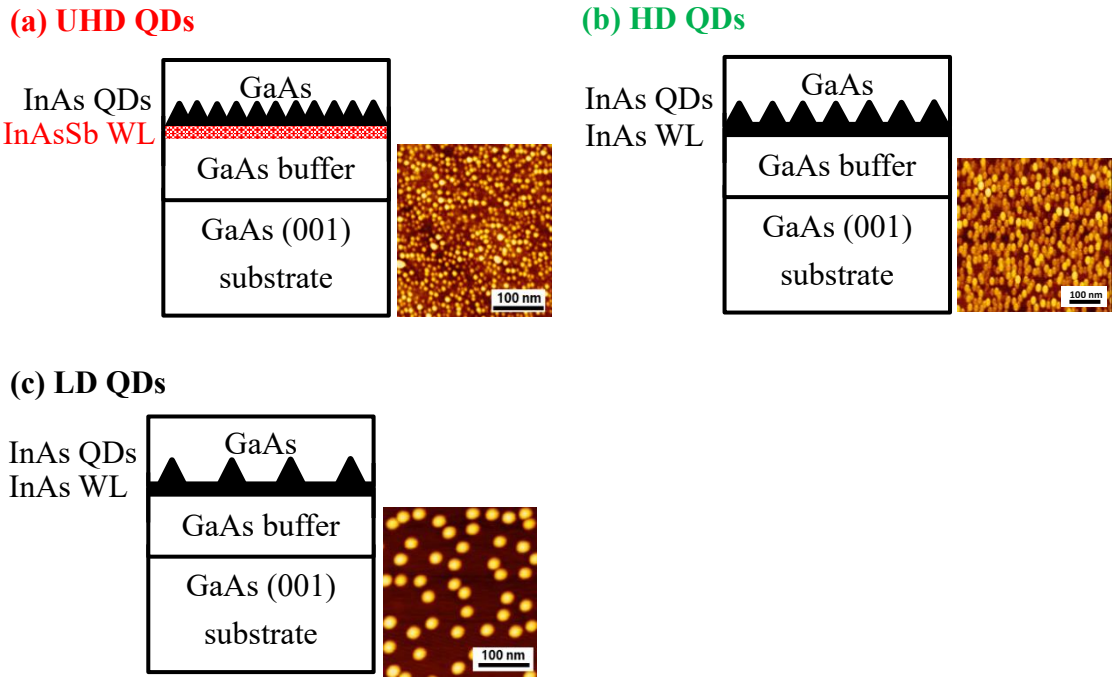

Figure 4.11 Schematic diagrams of InAs QD sample structures and typical AFM images of (a) UHD QDs, (b) HD QDs, and (c) LD QDs.

pulsed power was 300 mW, which corresponded to relative excitation power of 1000. Excitation wavelength was 785 nm, and the wavelength resolution for detection in this PL system was 1.27 nm. Temperature dependences of PL properties was measured from 15 K to 250 K.

4.7. Results and Discussions

Temperature dependences of PL properties were measured using a micro-PL system for the QD samples, with temperature ranging from 15 K to 250 K. The relative excitation power was approximately 30. As depicted in Figures 4.12, the PL spectra of UHD QDs, HD QDs and LD QDs shifted towards the low energy side as the temperature increased. This lower energy shifting corresponds to the Varshni shift, which describes the temperature dependence of the energy gap in InAs. At 15 K, the peak energy of UHD QDs was 1.229 eV (1009 nm), HD QDs was 1.219 eV (1019 nm) and LD QDs was 1.067 eV (1163 nm). The shorter wavelength and higher energy of UHD QDs and HD QDs were attributed to the quantum confinement effect of smaller-sized QDs[69]. As the size of the QDs decreases, the confinement of carriers inside the dot becomes stronger, increasing the energy required to excite the carriers accordingly. In contrast, the dot size of LD QDs was larger, resulting in weaker confinement, requiring lesser energy to excite the carriers and hence obtaining a longer wavelength. The FWHM value of the PL main peak at 15 K was 105 meV for UHD QDs, 82 meV for HD QDs, and 29 meV for LD QDs. The main peak of LD QDs originated from the GS transition, while the sub-peak originated from

the first excited state (ES1). Conversely, the main peak of UHD QDs and HD QDs included not only the GS transition but also the first and second excited state (ES2) transitions. The size distribution data of UHD QDs has been previously reported, and the size distribution data suggests that the inhomogeneous broadening of the QD energy levels in UHD QDs is larger than that of LD QDs. Due to the inhomogeneous broadening of UHD QDs, there was significant overlap between the GS and ES spectra, making it challenging to isolate the spectra of the GS peak and ES peak transitions. This situation is similar to that in HD QDs. The PL spectra at relative excitation powers of 1, 5, 20, 100, 500, and 1000, measured at 15 K, were shown in Figure 4.13 (a). The inset showed the positions of PL peak, PL minimum, and H50%, respectively. Blue shift energy at the PL peak, PL minimum, and at 50 % of PL spectra on the high energy sides (H50%) with

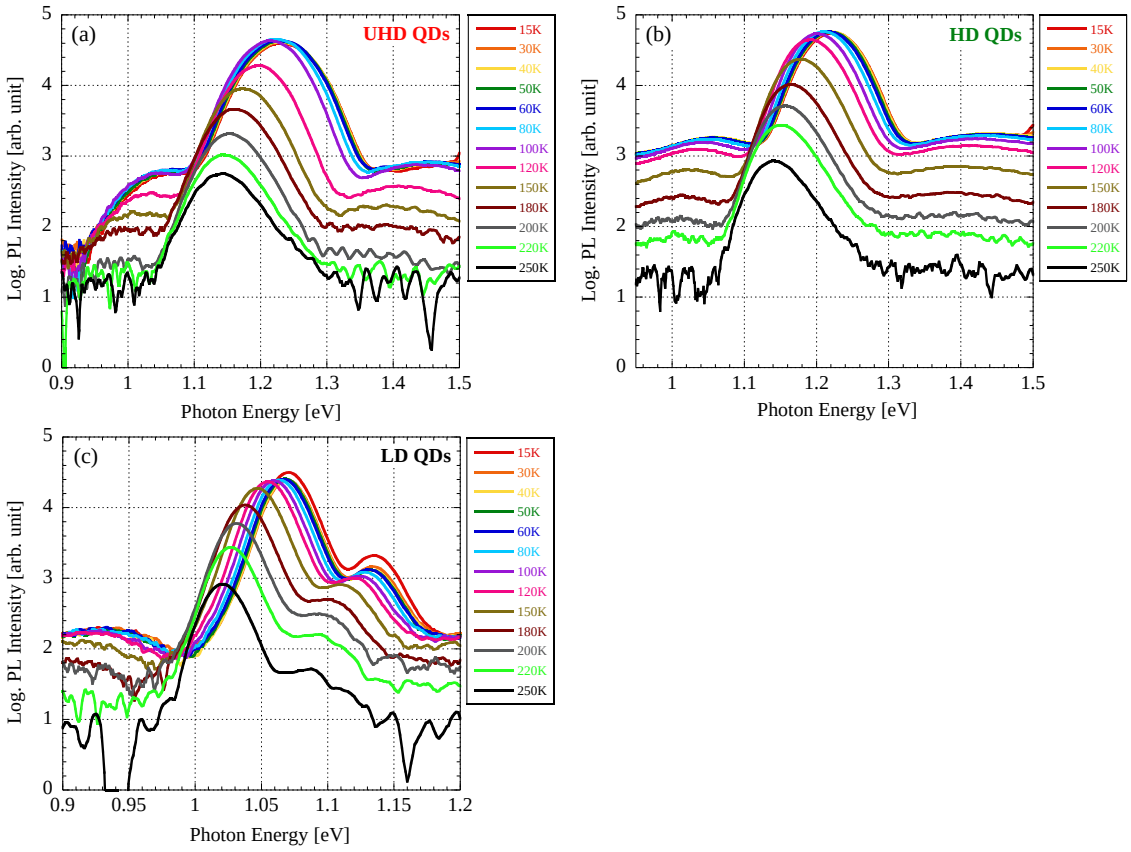

Figure 4.12 Temperature dependences PL spectra for (a) UHD QDs, (b) HD QDs and (c) LD QDs.

respect to relative excitation power were shown in Figure 4.13 (b). No blue shift was observed in PL minimum energy, as indicated by the almost constant response regardless of increasing excitation intensity. The carriers were originated from GS transitions, as the PL minimum energy value is less sensitive to the carrier escape and redistribution. The PL peaks remained almost constant below relative power of 20 and began to shift towards higher energy side as the excitation power increased. In other words, at relative power below 20, the peak was mainly contributed by carriers from the GS transitions. For the case of H50%, the blue shifts were continuous and significant even at weak excitation power. This was attributed to the inclusion of not only the GS but also ES1 components. As a result, the contributions from both GS and ES components should be considered, with a particular focus on ES components in this study.

In order to study the electronic strong coupling of UHD QDs, the temperature dependences of energy shifts for each QD states were analyzed, as depicted in Figure 4.14(a). Figure 4.14(d) – (f) display the logarithmic PL intensity graphs of UHD QDs,

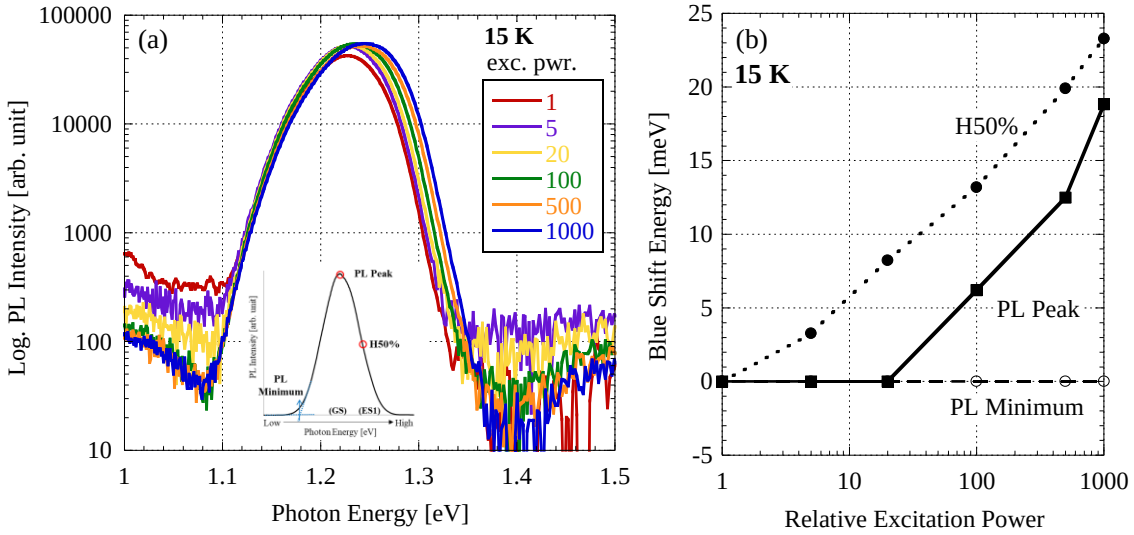

Figure 4.13 (a) Relative excitation power dependences PL spectra of UHD QDs at 15 K, and (b) blue shift energy at the PL peak, PL minimum, and at 50 % of PL spectra on the high energy sides (H50%) with respect to relative excitation power.

HD QDs and LD QDs, exhibiting the GS and ES1 components at 15 K, categorized by different percentages of PL intensity ranging from PL minimum, 10% to 80%. The PL main peak of LD QDs contained only GS components, whereas that of UHD QDs and HD QDs contained not only GS components but also ES components. In Figure 4.14(d) – (e), the high-energy components of H70%, H50% and H20% correspond to the ES components, and the low-energy components of PL minimum, L10%, L20%, L50% and L80% correspond to GS components. In Figures 4.12(a) – (c), the y-axes represent the differences in energies by subtracting the Varshni bandgap energy of InAs ($\mathrm{E}_{\mathrm{Varshni}}(T)$) from the photon energy at certain PL intensity ($\mathrm{E}_{\sim\%}(T)$)at respective temperatures (T). Therefore, the temperature dependent energy variation $\Delta\mathrm{E}(T)$ (= $\mathrm{E}_{\sim\%}(T) - \mathrm{E}_{\mathrm{Varshni}}(T)$) indicates a deviation from the Varshni bandgap energy shifting curve. In Figure 4.14(c), all GS components of LD QDs exhibited minimal variation in energies throughout the temperature change, closely following the Varshni shift. The longer separation distance between adjacent large QDs prevented electron tunneling and strong coupling in LD QDs.

In contrast, the ES1 components of UHD QDs in Figure 4.14(a) showed almost constant variations below 60 K, indicating that carriers in UHD QDs were completely confined and did not strongly combine, although carrier transport by tunneling could occur[21]. Above 60 K, a sudden increase in variations indicated deviation from the Varshni shift, no longer following the bandgap shrinkage from the Varshni empirical formula. Similarly, the GS components of UHD QDs also experienced a sudden increase in energy variation, but at a higher temperature of 100 K. Based on the energy variation from the plots of UHD QDs, strong coupling of QDs was observed from the ESs at 60 K, progressing to strong coupling at the GSs as the temperature increased to 100 K. This observation suggests a dynamic process in UHD QDs where the strong coupling of QDs

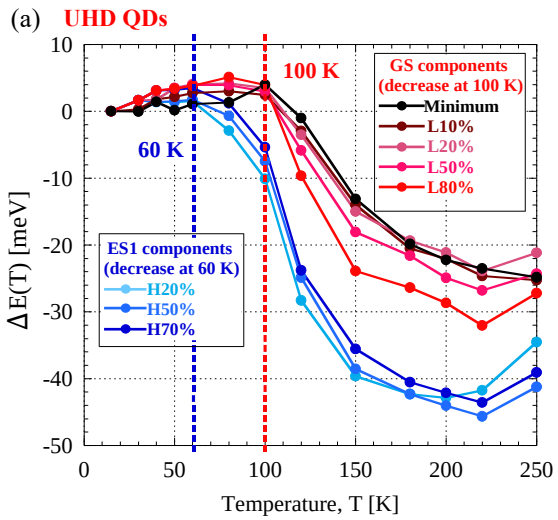
(a) UHD QDs
100 K
60 K
GS components
(decrease at 100 K)
Minimum
L10%
L20%
L50%
L80%
ES1 components
(decrease at 60 K)
H20%
H50%
H70%
ΔE(T) [meV]
Temperature, T [K]

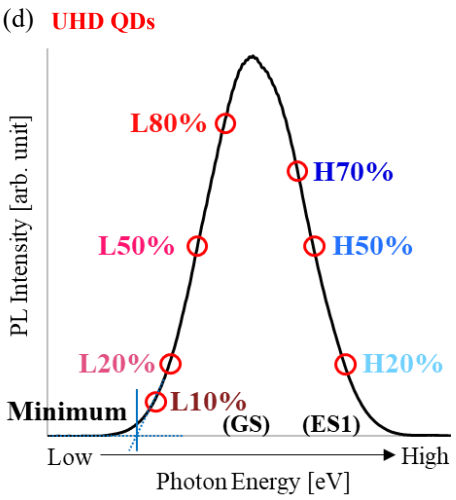
(d) UHD QDs
L80%
H70%
L50%
H50%
L20%
H20%
Minimum
L10%
(GS)
(ES1)
PL Intensity [arb. unit]
Low
High
Photon Energy [eV]

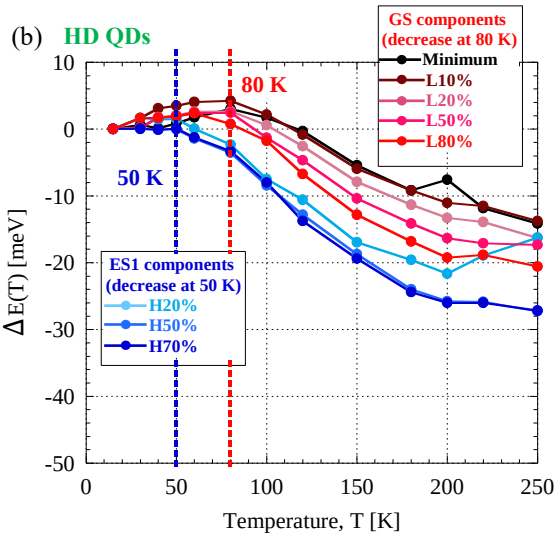
(b) HD QDs
80 K
50 K
GS components
(decrease at 80 K)
Minimum
L10%
L20%
L50%
L80%
ES1 components
(decrease at 50 K)
H20%
H50%
H70%
ΔE(T) [meV]
Temperature, T [K]

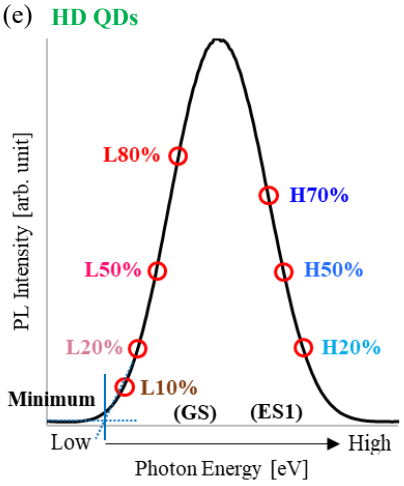
(e) HD QDs
L80%
H70%
L50%
H50%
L20%
H20%
Minimum
L10%
(GS)
(ES1)
PL Intensity [arb. unit]
Low
High
Photon Energy [eV]

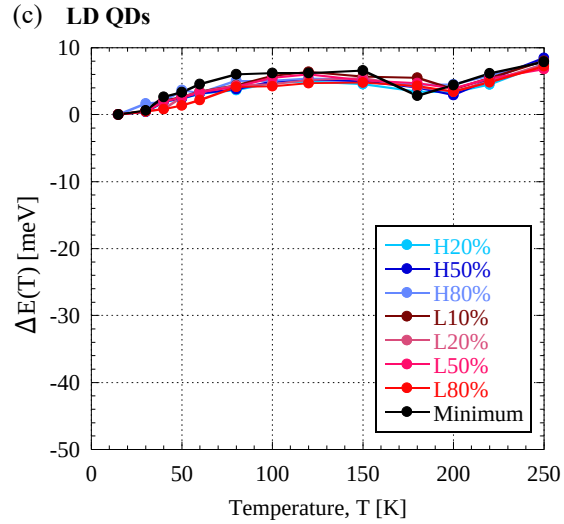
(c) LD QDs
H20%
H50%
H80%
L10%
L20%
L50%
L80%
Minimum
ΔE(T) [meV]
Temperature, T [K]

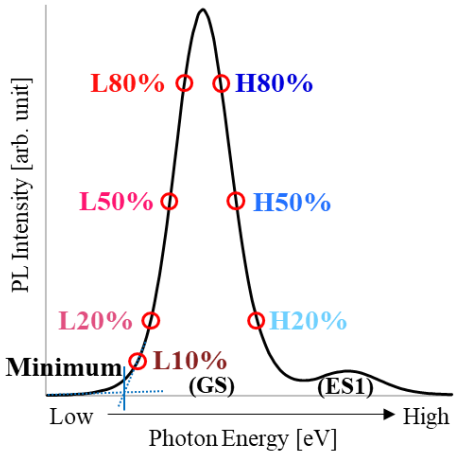
(f) LD QDs
L80%
H80%
L50%
H50%
L20%
H20%
Minimum
L10%
(GS)
(ES1)
PL Intensity [arb. unit]
Low
High
Photon Energy [eV]

Figure 4.14 Temperature dependent energy variation graphs featuring the GS and ES1 components for (a) UHD QDs, (b) HD QDs and (c) LD QDs. Y-axes represent differences in energies by subtracting the Varshni bandgap energy of InAs ($E_{Varshni}(T)$) from the photon energy at certain PL intensity ($E_{\sim\%}(T)$), $\Delta E(T) = E_{\sim\%}(T) - E_{Varshni}(T)$, at respective temperatures (T). The PL intensity graphs of (d) UHD QDs, (e) HD QDs and (f) LD QDs exhibit the GS and ES1 components at 15 K, categorized by different percentages of PL intensity ranging from PL minimum, 10% to 80%. In the legend, H~% represents the high energy side, while L~% represents the low energy side. Graphs of UHD QDs and HD QDs display the GS and ES1 components, while LD QDs displays the GS components.

and the miniband formation initiate from the higher energy side (ESs) at lower temperatures, gradually progressing towards the lower energy side (GSs) as the temperature increases. As discussed in Section 4.4, the PL minimum energy of UHD QDs, originating from the largest QDs where carriers are always occupied in their GSs, experienced deviation from the Varshni shift at 100 K, demonstrating the lowering of the GS levels of the largest QDs due to strong coupling. The energy variation of the PL minimum energy in Figure 4.14 (a) showed an increase in energy deviation above 100 K. This behavior is similar to that of other GS components and is consistent with the results shown in previous study.

As with HD QDs, the ES1 components remained constant below 50 K, while the GS components were constant below 80 K. The slight differences in the temperatures at which energy variation increased (when comparing UHD QDs and HD QDs) were due to differences in inhomogeneous broadening, as the FWHM of HD QDs was slightly smaller than that of UHD QDs. Based on the energy variation observed in the plots of HD QDs, strong coupling of QDs was determined in the ESs at 50 K, progressing to strong coupling in the GSs as the temperature increased to 80 K. According to the plots from both UHD

QDs and HD QDs, the phenomenon of strong coupling at lower temperature for the ESs and at slightly higher temperature for the GSs was significant and reliable.

To provide a clearer understanding of the processes involving the strong coupling of QDs and the formation of energy minibands, schematic diagrams illustrating the states of in-plane QDs in the conduction band are presented in Figure 4.15. As the temperature rises, the homogeneous broadenings of QD energy levels expand. Even if there is a slight difference of QD energy levels of adjacent QDs, the strong coupling between adjacent QDs occurs by overlapping of broaden QD energy levels. Additionally, the energy minibands are formed as the number of strongly coupled QDs increases. Not only the energy matching of QD energy levels but also the separation distance between neighboring QDs must be narrow enough for overlapping the electronic wavefunctions. According to the quantum mechanical coupling effect, the separation distance between QDs is closely related to wavefunction localization and delocalization. Strong coupling of the electron wavefunction was reported to occur at interdot distances of less than 10 nm. In the case of InAs/InAsSb UHD QDs, the average separation distance between the

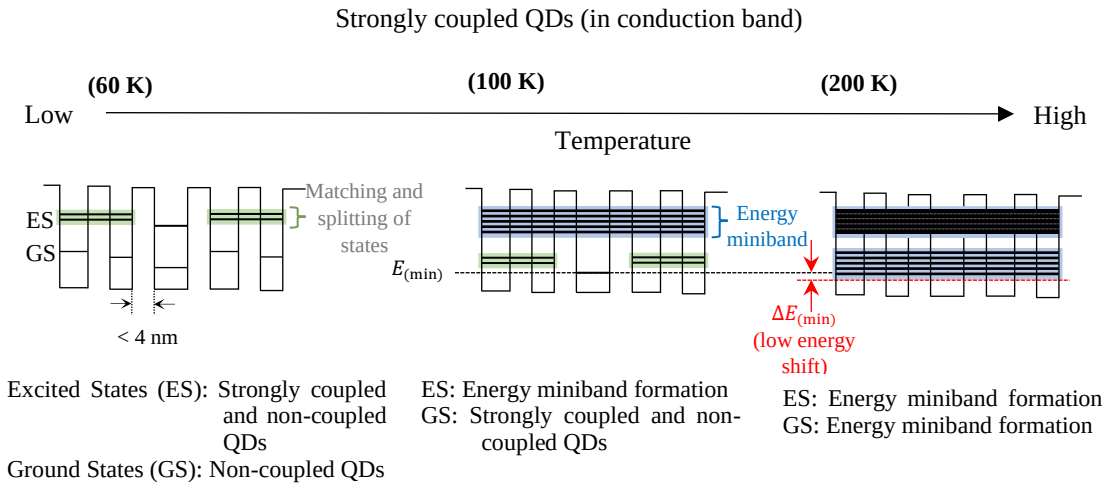

Figure 4.15 Schematic diagrams of temperature dependence of strong coupling process in conduction band. Energy miniband is formed by many strongly coupled QDs.

in-plane QDs was less than 4 nm. Since the homogeneous broadening of QD GSs is very narrow at temperatures below 60 K, strong electronic coupling is challenging to achieve due to quantum level differences between adjacent QDs, despite the small separation distance. However, electrons in QD ESs possess higher energies within broader energy distributions, leading to the matching and overlapping of similar energy levels with neighboring QDs. This overlap of QD energy states fosters strong electronic coupling between neighboring QDs through coherent tunneling. QD energy states then split into bonding and antibonding states due to strong coupling, representing electron wavefunction delocalization (indicated by green bands). As the temperature increases to 60 K, further homogeneous broadening of ESs allows majority of neighboring QD energy levels to match and overlap. The splitting and spreading of many energy states begin to form a continuous band across in-plane QDs, known as an energy miniband (indicated by blue bands). At 100 K, further homogeneous broadening of GSs initiates strong coupling interactions between QDs. Minibands are successfully formed in ESs, while in GSs, the formation of minibands is still in progress. When a miniband is formed, the minimum energies of QDs shift to lower energy levels due to wider homogeneous broadening.

Figure 4.16 illustrates the temperature dependence of PL decay time in UHD QDs and LD QDs, analyzing three portions of the PL spectra: the peak, 50 % PL intensity at the high energy side (H50%), and 50 % PL intensity at the low energy side (L50%). As indicated in the inset of Figure 4.16(a), the H50% of UHD QDs consists of ES1 components, whereas the peak and L50% consist of GS components. On the other hand, the PL spectra of LD QDs, as shown in Figure 4.16(b), consist of solely GS components across the peak, H50% and L50%. In LD QDs, it was observed that the lifetime of carriers at GSs remained unchanged below 30 K, then increased at 120 K due to carrier

delocalization in large QDs[29]. The nonradiative lifetime subsequently decreased with increasing temperature due to the thermal escape of QDs, from around 120 K to 250 K. The PL decay lifetime plots of LD QDs exhibited a response similar to that found in several studies[70,71]. Conversely, the GSs of UHD QDs maintained their lifetimes until 50 K. This nearly constant PL lifetime indicated weak carrier delocalization in small QDs. Since the majority of carriers originated from the GSs, strong coupling was not observed before 100 K, as indicated in Figure 4.14(c). The lifetime of UHD QDs' ESs remained constant and then started to decline from 15 K to 150 K. In contrast, an increase could be observed at the GSs from 50 K to 100 K. This behavior was also observed by Yang et al., where the thermal emission of carriers into the wetting layer occurred at higher transition energies, resulting in reduction of PL decay lifetime as the temperature increased[72]. Simultaneously, these carriers were recaptured by the low energy QDs to be replenished, resulting in an increase in PL decay time at the GSs. The shorter decay time of ES compare to that of GS in UHD QDs could correlate to the carrier relaxation to GS as reported in several studies[73,74]. Faster decay times were reported for higher energy levels by Tackeuchi et. al. in their multi-coupled InAs/GaAs QD sample structure, that suggested the presence of lateral tunneling between QDs[63]. The carriers in the higher

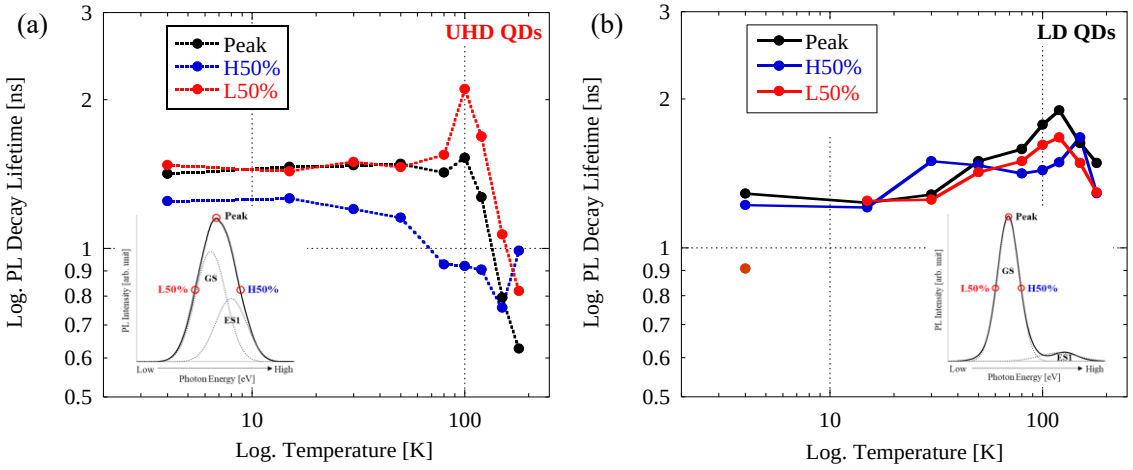

Figure 4.16 Temperature dependence PL decay time of (a) UHD QDs and (b) LD

energy levels of smaller QDs can transfer to lower energy levels in neighboring larger QDs. Since carriers at higher energy levels have more available lower-energy states to transition into, the decay time shortens for higher energies. Conversely, carriers at lower energy levels experience slower decay due to more carriers arriving from higher energy levels and the limited availability of lower-energy states to transition into. Additionally, in Figure 4.16, the major "drop" temperature of the GSs was at 100 K, compared to the 50 K "drop" temperature at the ESs. Since strong coupling of QDs and miniband formation progressed from the ESs (> 60 K) to the GSs (> 100 K), both the effect of strong coupling process and thermal carrier escape due to nonradiative processes could be observed from the decrease in lifetime as homogeneous broadening of states widened with increasing temperature.

Figure 4.17 shows the temperature dependence of the PL integral intensity for both UHD QDs and LD QDs. Due to localization effects at low temperatures, the PL integrated intensities of UHD QDs were almost insensitive to temperature below 100 K, while LD QDs remained constant below 120 K. Both QD samples experienced an intensity drop as

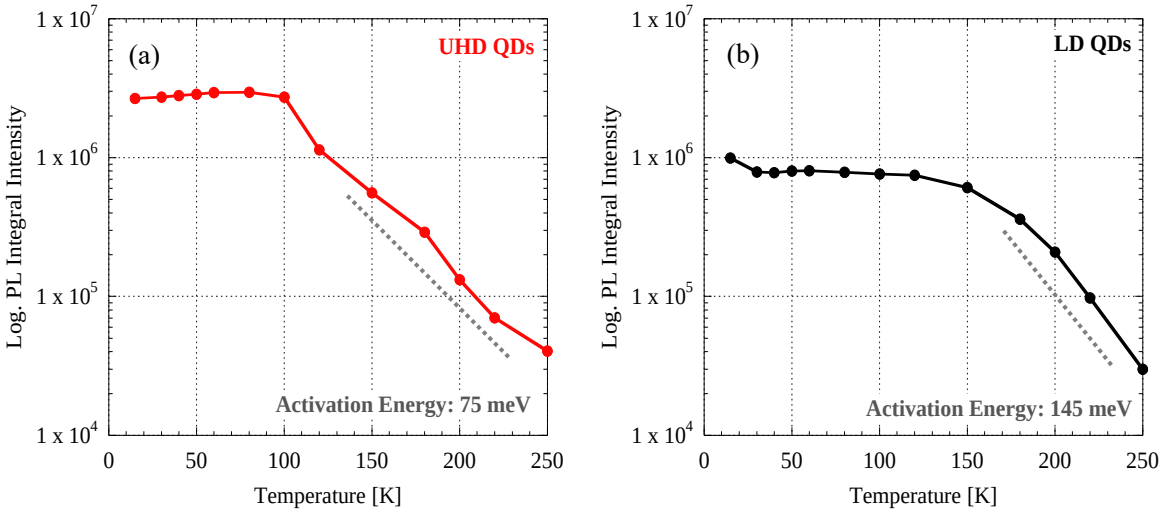

Figure 4.17 Temperature dependence PL Integral Intensity of (a) UHD QDs and (b) LD QDs.

the temperature increased due to the enhancement of non-radiative recombination processes[70,75]. A sudden quenching of PL intensity was observed at 100 K for UHD QDs and at 150 K for LD QDs, attributed to the carrier escape and non-radiative recombination processes. Activation energies for both types of QDs were calculated and plotted using Arrhenius plot. The higher activation energy of LD QDs (145 meV) compared to UHD QDs (75 meV) indicates that LD QDs has deeper energy levels. This means that carriers in LD QDs require more energy to thermally excite from the QDs to the GaAs continuous energy band. In LD QDs with a large interdot spacing, there is no electronic coupling between the QDs, leading to strong quantum confinement of carriers within them and higher activation energy. Conversely, in UHD QDs with small interdot spacings, the wave function of electrons may become delocalized, reducing the level of quantum confinement and subsequently lowering the activation energy.

The temperature dependences of PL FWHM variations for UHD QDs and LD QDs are illustrated in Figure 4.18. The FWHM of LD QDs originated from GS peak transitions, whereas the FWHM of UHD QDs included both GS peak transitions and ES peak

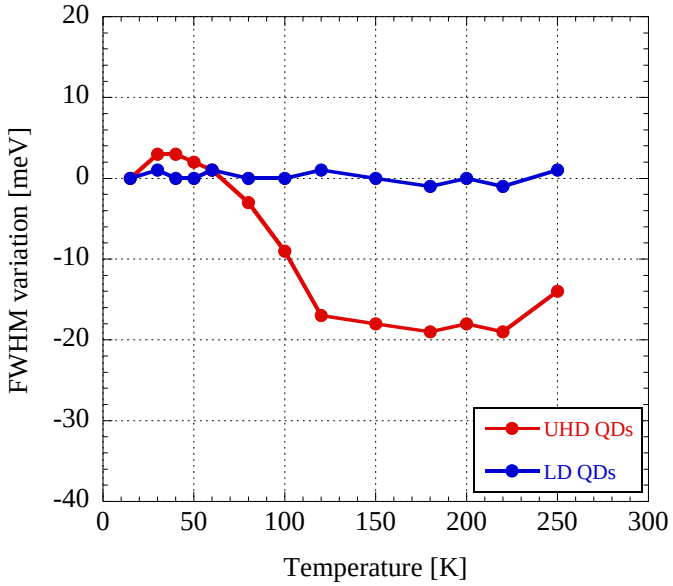

Figure 4.18 Temperature dependence PL FWHM of UHD QDs and LD QDs.

transitions. The FWHM of LD QDs remained almost constant despite the increasing temperature, attributed to the narrow size distribution of QDs and the wider separation between QDs, which prevented strong coupling to occur. Conversely, for UHD QDs, a similar behavior observed in other studies[76–80] can be seen from 15 K to 120 K, where the FWHM drastically decreased. As the temperature increases, the carrier escape from smaller QDs with higher energy levels via tunneling to neighboring QDs is enhanced, resulting in the observed shrinkage of FWHM. From 120 K to 220 K, the FWHM of UHD QDs remained almost constant, contrary to the "V-shaped variation" observed in some studies[59,61,81], which can be attributed to electron-phonon scattering. This behavior is clarified by the PL spectra of UHD QDs, where strong coupling of QDs occurred, and minibands were already formed at both GSs and ESs above 100 K. When the miniband is formed, carriers can move laterally within the continuous energy miniband of the UHD QD layer. This means that carrier transfer strongly depends on the miniband, where carrier excitation and recombination occur within the miniband, through strongly coupled QDs, leading to the observed almost constant FWHM. Furthermore, above 220 K, a slight increase in FWHM was observed, with the increase from 220 K to 250 K being 5 meV. This slight broadening of the FWHM is related to the carrier energy distribution in the miniband of the UHD QD layer, where electrons occupy higher energy states in the miniband, based on the Fermi-Dirac distribution function $f(E)$. This energy distribution broadening of 5 meV corresponds to an $f(E)$ value of 0.147, explaining the slight increase in the PL FWHM of UHD QDs by the electron energy distribution in the miniband. Therefore, it is possible that this abnormal behavior of the constant FWHM originated from the in-plane miniband formation.

4.8. Chapter Summary

In-plane InAs UHD QDs ($0.8 - 1 \times 10^{12}\ cm^{-2}$) were fabricated on an InAsSb WL, capped with a GaAs layer using MBE. Through thorough investigation of PL spectra, decay times, and FWHM variations, unique temperature dependent phenomena exhibited by UHD QDs have been discovered. Below 60 K, UHD QDs demonstrated minimal variation in PL intensity, suggesting carrier confinement within individual QDs. Based on the temperature dependences of PL energy and decay times, strong coupling of UHD QDs was observed from the ESs at 60 K, progressing to strong coupling at the GSs as the temperature increased to 100 K. This observation suggests a dynamic process where the coupling of QDs and the formation of minibands initiate from the higher energy side (ESs) at lower temperatures, gradually progressing towards the lower energy side (GSs) as the temperature increases. Temperature dependent FWHM variations between 120 K and 220 K remained almost constant, attributed to carrier transfer that strongly depends on miniband, where strong coupling of QDs and miniband formation already observed above 100 K. These findings contribute to a deeper understanding of the electronic interactions and transport mechanisms in UHD QDs, thus facilitating their potential applications in high-performance optoelectronic devices.

Chapter 5. Photoconductive Properties of InAs/InAsSb In-Plane UHD QDs

5.1. Photocurrent-Voltage Properties

5.2.1. Introduction

As miniaturization continues to drive technological advancements, QDs have emerged as promising building blocks for next-generation electronic and optoelectronic devices. Among their intriguing properties, self-assembled QDs have received particular attention as it directly influences device performance, especially in photodetection structures like quantum dot infrared photodetectors (QDIPs) and intermediate band solar cells (IBSCs). QDIPs leverage the discrete energy levels of QDs to detect infrared light with high sensitivity and QDIPs have the advantage to operate at high temperatures (> 150 K). Similarly, in IBSCs, QDs introduce an intermediate band within the semiconductor's bandgap, enabling the absorption of sub-bandgap photons. This intermediate band facilitates a two-step photoexcitation process[15,26,82,83]. This mechanism allows IBSCs to harvest a wider spectrum of solar energy, increasing the overall efficiency of solar cells.

To optimize the performance of QD-based devices, understanding the mechanisms governing carrier transport between their energy levels is crucial, alongside their structural characteristics. At low temperatures, the strong localization of QD levels due to quantum confinement leads to hopping conduction within the QD layer. However, a reduction in the surrounding barrier thickness can lead to significant delocalization of the QD wave functions. This delocalization will result in strong interdot coupling through resonant tunneling, as observed in several studies on vertically-stacked QD structures like quantum dot superlattice (QDSL). When the dot periodicity, interdot distance, and dot

size distribution are very uniform, as in the case of QDSL, delocalized wavefunctions lead to coupling with surrounding QDs via resonant tunneling, forming minibands[30,31,83]. Additionally, due to the small QD separation distance of less than 4nm, strong interdot coupling induced by significant wavefunction overlap in the in-plane InAs/InAsSb ultrahigh-density QDs has been shown recently to induce an additional PL minimum energy shifting in GS at 100 K[33], and PL high energy shifting in ES at 60 K[84], which leads to in-plane miniband formation.

Building upon this existing research, the present work focuses on the in-plane photoconductive properties of InAs LD QDs and UHD QDs via temperature-dependent photocurrent-voltage measurements under 925 nm light irradiation. Two-step photoexcitation process in QD samples was supported by the quadratic trend observed in excitation intensity dependence measurements. Furthermore, photocurrent density measurements across a range of temperatures revealed that UHD QDs exhibit a substantially higher photocurrent density compared to LD QDs, particularly at temperatures above 120 K. This is attributed to the formation of miniband and adjacent QDs that are coupled strongly. These connections allow for efficient lateral carrier transport, reducing the likelihood of carrier recombination and thereby increasing the overall photocurrent.

5.2.2. Experimental Setup

Figure 5.1 shows the schematic diagrams of two types of samples (a) InAs LD QDs and (b) InAs/InAsSb UHD QDs, as well as the structure of the QD samples. In the photocurrent experiments, a 500 nm thick non-doped GaAs layer without QDs was also prepared for comparison. All samples were produced on SI GaAs(001) substrates using

MBE. From AFM measurements, the average lateral size and average height of InAs UHD QDs were 12 nm and 1.5 nm, respectively, whereas those of InAs LD QDs were 29 nm and 10 nm, respectively. A 200 nm thick non-doped GaAs buffer layer was deposited on the GaAs substrate at 580 °C. The temperature was lowered to 460 °C for the growth of InAsSb WL and InAs UHD QDs. By incorporating Sb atoms into the WL prior to InAs QDs growth (Sb-mediated S-K growth mode), the coalescence and ripening of QDs were effectively suppressed. The coverage of the InAsSb WL ranged from 1.25 to 1.30 ML, and the InAs coverage for QDs ranged from 0.95 to 1.0 ML, resulting in a total coverage of 2.2 to 2.3 ML. The growth rate of UHD QDs was 0.035 ML/s, resulting in a QD density of $0.8 - 1 \times 10^{12}\ cm^{-2}$. The InAs LD QDs were grown on the InAs WL at 500 °C and the same growth rate of 0.035 ML/s. A total InAs coverage of 2.6 ML, and the QD density was $4 \times 10^{10}\ cm^{-2}$. In both samples, the single QD layer was covered with a 60 nm

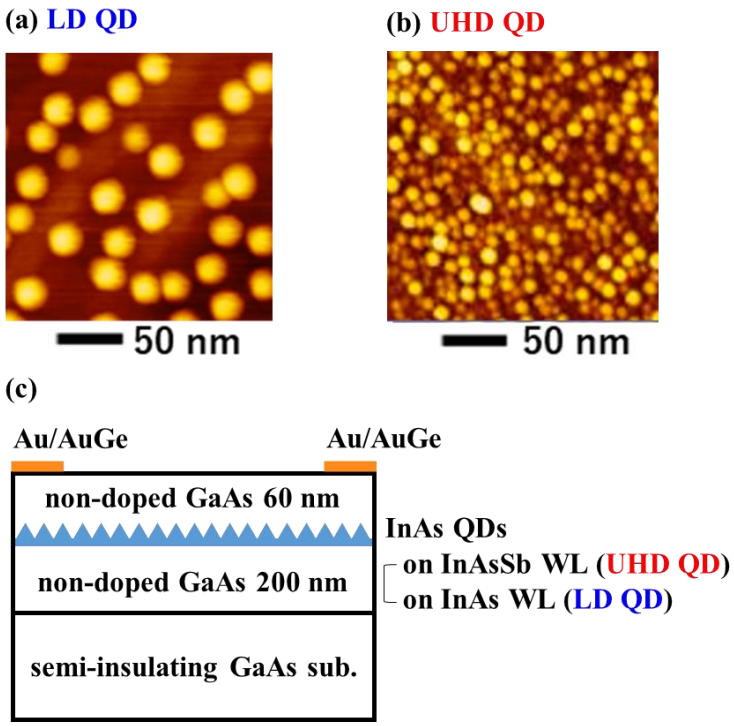

Figure 5.1 AFM images of (a) LD QDs (b) UHD QDs and (c) schematic diagram of InAs QD sample structure for photocurrent measurement.

thick non-doped GaAs capping layer.

Figure 5.1(c) shows the sample structure for photocurrent measurements. After the MBE growth, Au/AuGe electrodes for ohmic contact were fabricated on the sample surfaces. The separation distance between two electrodes was around 100 μm for all of the samples. In the photocurrent measurements, the laser beam with a diameter of about 60 μm was irradiated on the center between two electrodes, and the sample temperature was changed from 15 K to 210 K. The light wavelength and laser power density were 925 nm and approximately $5.7\ W/cm^2$ (maximum), respectively.

5.2.3. Methodology

After crystal growth, electrodes for ohmic contact were fabricated on the samples. Photolithography was used to create the desired patterns on the samples for photocurrent measurement. Electrode deposition was performed using a resistance-heated vacuum deposition system to deposit AuGe and Au sources in a vacuum. The AuGe mass ratio was Au:Ge = 88:12, corresponding to the composition that evaporates at the lowest temperature. Samples then undergo annealing process where Ge diffuses into the GaAs side to form an n+ region, resulting in a very thin Schottky contact layer and achieving ohmic contact.

Photocurrent measurement was conducted by connecting the sample to the micro-PL measurement system. A source meter (Keithley-2400) was used to connect the wires and perform the four-terminal measurement method. Laser light from a supercontinuum light source (frequency: 60MHz, period <100ps) was spectrally dispersed by a spectrometer and irradiated onto the sample at the wavelength of 925 nm. The irradiation diameter was confirmed using a CCD camera, and the light was irradiated between the electrodes for

the photocurrent measurement at temperatures ranging from 15 K to 210 K.

5.2.4. Results and Discussions

Figure 5.2 shows the PL spectra of (a) LD QDs and (b) UHD QDs at temperatures ranging from 15 K to 210 K. The excitation light wavelength was 785 nm (1.58 eV), which is higher in energy than the GaAs bandgap. Photoexcited carriers relax into the QDs through phonon interactions, filling the lower QD levels of the GS and the ES1. In the LD QDs, two distinct peaks were observed, corresponding to emissions from GS and ES1 transitions. In contrast, the UHD QDs exhibited broad PL spectra at all temperatures due to significant inhomogeneous broadening. These broad spectra included contributions from GS, ES1, and ES2. By decomposing the PL spectrum into its GS and ES1 components, we can also predict the presence of ES2 and the third excited state (ES3) components, as shown in the fitted spectra at 210 K.

In the photocurrent measurements of LD QDs, UHD QDs, and samples without QDs,

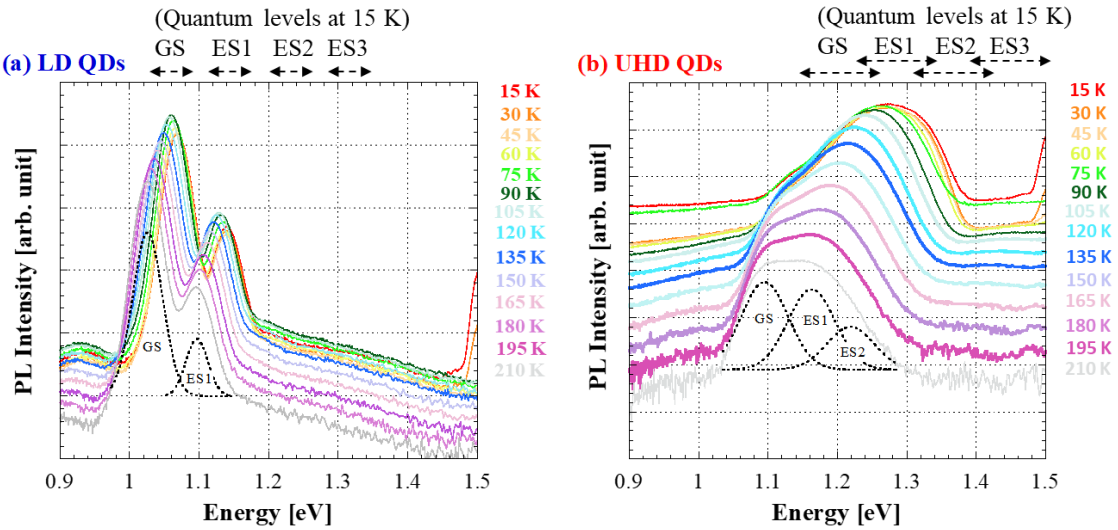

Figure 5.2 Temperature dependences PL spectra for (a) LD QDs and (b) UHD QDs. Decompositions of PL spectra into GS and ES are shown in both QD spectra at 210 K and respective quantum levels marked by arrows at 15 K for better understanding.

the excitation light had a wavelength of 925 nm (1.34 eV). This wavelength is below the GaAs bandgap, so interband absorption in GaAs does not occur. However, photoexcited carriers can be generated near ES3-ES4 for LD QDs and ES2-ES3 for UHD QDs across the temperature range of 15 K to 210 K. Figure 5.3 shows the temperature-dependent photocurrent density (J) versus electric field (E) curves for UHD QDs, LD QDs, and samples without QDs. The electron density in the undoped GaAs layers of all samples was very low, approximately $4 \times 10^{14}\, cm^{-3}$, causing the GaAs layers to be fully depleted by electron traps in the GaAs surface states. This depletion results in high resistance in the samples under dark conditions. When exposed to 925 nm light, photocurrent was detected even in the GaAs sample without QDs, as shown in Figure 5.3(c). This photocurrent is attributed to the photoexcitation of electrons in the GaAs surface states. Applying a bias voltage between two electrodes creates a transverse electric field across the surface depletion layer, leading to the lateral flow of photoexcited carriers. However, the photocurrent decreased accordingly as temperature increased because of phonon scattering and recombination process.

Both UHD QD and LD QD samples showed an exponential increase in photocurrent density with increasing electric field, which then gradually saturated. This exponential increase in photocurrent density is attributed to the field emission (tunneling) effect, where electrons within the QDs tunnel into the GaAs conduction band. Using Wentzel-Kramers-Brillouin (WKB) approximation[85], the tunneling probability (T) for a triangular potential barrier of energy height E can be expressed as:

$$T \cong \exp\left[-d(8\,\pi\,/3h)(2mE)^{\frac{1}{2}}\right] \qquad (5.1)$$

Where, m is an effective mass of electron, and h is Plank constant. The width d of

tunnel barrier monotonically decreases with increasing the applied voltage (electric field). Thereby, the tunnel current increases exponentially with increasing the applied voltage. As the energy levels of the UHD QDs are higher than those of the LD QDs, the tunneling energy barrier for the UHD QDs is lower, enhancing the tunneling effect. The substantial photocurrent observed at low temperatures is believed to result not only from the tunneling effect of photoexcited electrons in the QDs but also from the two-step photoexcitation effect via the QD levels.

Higher photocurrent was observed in UHD QDs at low temperatures from 15 K to 90 K, while lower photocurrent was observed at higher temperatures from 120 K to 210 K. This is due to scattering is less likely to occur at low temperatures hence mobility of carriers is expected to be higher, so does the conductivity. Previous studies have shown that strong coupling of QDs and the formation of minibands in UHD QDs begin at the higher energy side (ES1) at 60 K and gradually progress towards the lower energy side (GS) by 100 K. Thus, at 60 K, continuous minibands are likely already formed at higher

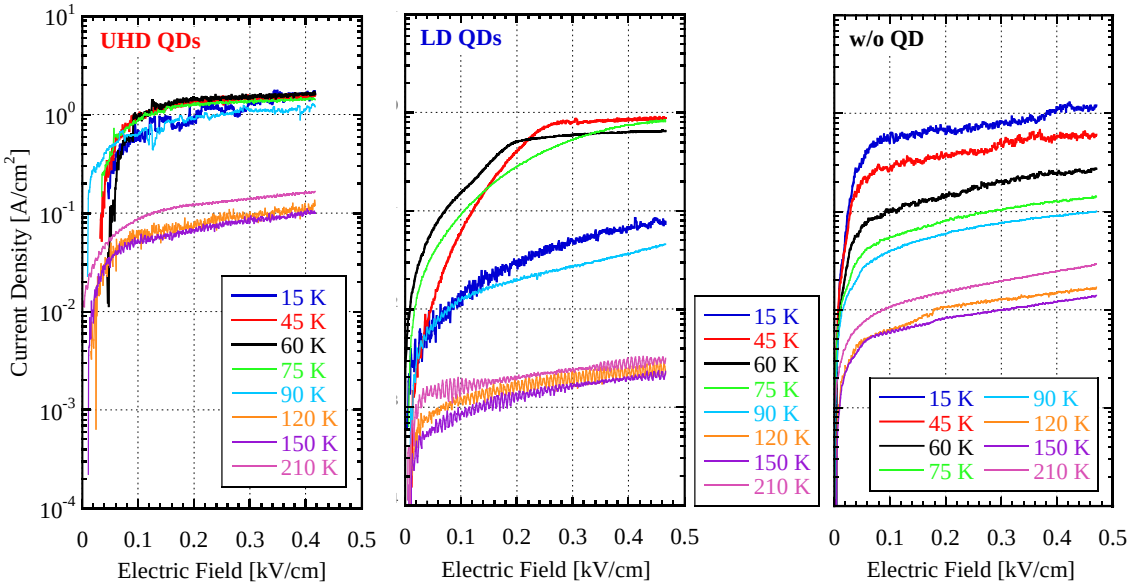

Figure 5.3 Temperature-dependent photocurrent density versus electric field graphs of UHD QDs, LD QDs and GaAs sample without QD.

energy states (ES2 and ES3). Under these conditions, the higher energy levels consist of partial minibands and localized states. Carriers can transport laterally between QD levels through these partial minibands and are thermally excited to the GaAs conduction band at a higher rate due to the lower barrier height, which indicates that carriers can conduct parallelly in both QD layer and GaAs layer. However, at 15 K, partial minibands are not formed even at higher energy states, resulting in the localization of carriers within the QDs. In this scenario, current flow relies on tunneling from one state to another, and the rate of carrier escape to the GaAs conduction band is lower due to the higher barrier height. This results in lower current density at 15 K compared to 45 K – 75 K.

In contrast, minibands are not formed in LD QDs due to the larger separation distance between adjacent QDs, resulting in primary transport through hopping conduction. Despite of less scattering events at low temperatures, higher photocurrent density observed in LD QDs from 15 K to 60 K can be attributed to the two-step photoexcitation process. As shown in Figure 5.4(a), first-step optical absorption occurs between QD energy levels from the QD valence band to the QD conduction band, and then these first-photoexcited electrons in QDs are excited to the continuous states of GaAs conduction band (the second-step photoexcitation). Above 90 K, the lowest current density among all samples observed in LD QDs was attributed to recombination processes, of which the QDs acted as a recombination center in this scenario, that further enhanced the recombination events, resulting in extremely small photocurrent. Among all samples, the photocurrent density of UHD QDs at every temperature was significantly higher, which was attributed to carrier tunneling between close-distance QDs and lateral transport in miniband of QD layer.

Figure 5.5 shows the relationships between the photocurrent and the relative excitation

light power for the UHD QDs, LD QDs, and the sample without QDs at (a) 15 K, (b) 60 K, and (c) 180 K. At 15 K and 60 K, the photocurrent of UHD QDs increased proportionally to the square of the excitation light power at both a weak electric field (0.04 kV/cm) and a high electric field (0.35 kV/cm) under low excitation power. This quadratic behavior is evidence of the two-step photoexcitation effect due to longer carrier lifetime at low power. As the relative excitation light power exceeded about 100 μW, the trend shifted to a linear increase in photocurrent. This change is attributed to the decrease in the optical absorption coefficient of the first step due to increased carrier occupancy at the QD levels, hence tunneling to GaAs band is dominant. A similar linear behavior was observed at 180 K with increasing excitation power but at a much lower current density. This is because two-step photoexcitation was suppressed by increased recombination of the first-excited carriers.

For LD QDs, photocurrent saturation was observed as the excitation power increased at low temperatures (15 K and 60 K), with more pronounced saturation at low electric

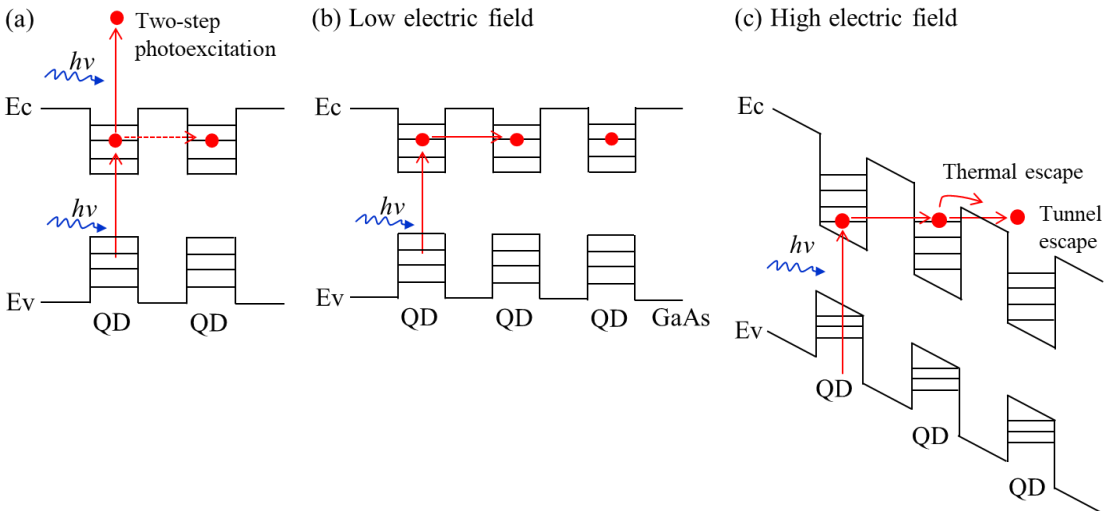

Figure 5.4 Schematic band diagrams of UHD QDs in (a) two-step photoexcitation process, (b) low electric field photocurrent measurement, and (c) high electric field photocurrent measurement.

field. This saturation is due to the state filling effect and the slower rate of excitation to the GaAs conduction band in LD QDs, making the photocurrent less dependent on increasing power. On the other hand, photocurrent during high electric field exhibited exponential manner, which indicates that both two-step photoexcitation and hopping conduction existed due to lower barrier height between QDs which assisted the tunneling probability.

The sample without QDs, on the other hand, demonstrated a linear relationship with respect to excitation power regardless of temperature and electric field strength. This

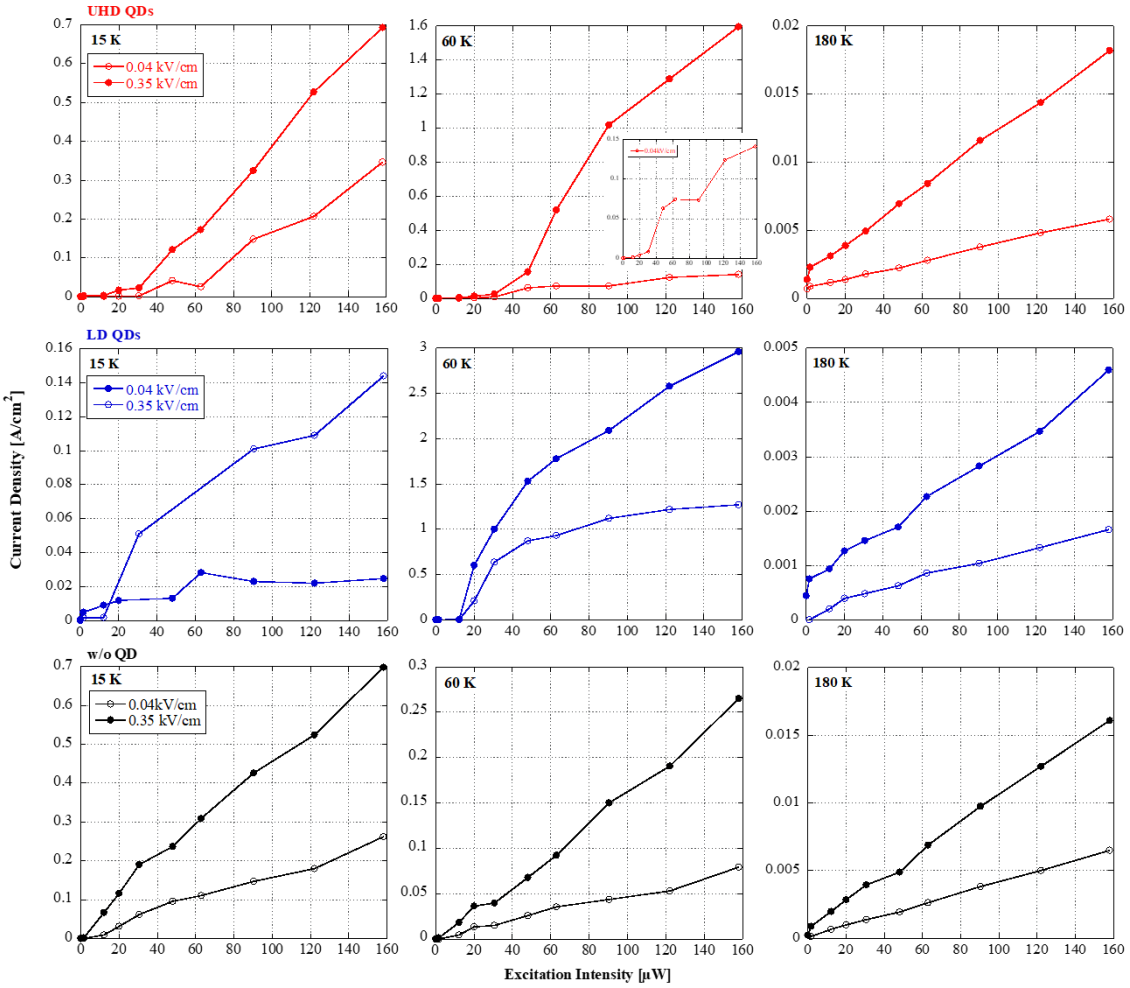

Figure 5.5 Photocurrent of InAs QD samples and w/o QD sample with respect to relative excitation light power at 0.04 and 0.35 kV/cm at (a) 15 K, (b) 60 K, and (c) 180 K.

linear behavior is primarily due to photoexcitation originating from electrons trapped in surface states. As shown in Figure 5.3, the photocurrent of all samples experienced a significant decrease above 150 K. Conversely, Figure 5.5 shows that the photocurrent increased monotonically with increasing excitation light power at 180 K. As the temperature rises, the non-radiative recombination lifetime decreases, leading to a shorter carrier lifetime in the QD states. Additionally, higher temperatures enhance carrier escape from the QD levels. Therefore, at 180 K, for all samples, the photocurrent significantly decreased due to the suppression of the two-step photoexcitation and the increased recombination of the first excited carriers.

Figure 5.6 shows the temperature dependence of photocurrent density for the UHD QDs, LD QDs, and samples without QDs. At an electric field of 0.35 kV/cm, the photocurrent in LD QDs is mainly due to two-step photoexcited carriers and field-emitted carriers from the QD states through the tunnel barrier. In this low-temperature region, the carrier lifetime within the QD states is longer, enhancing the two-step photoexcitation

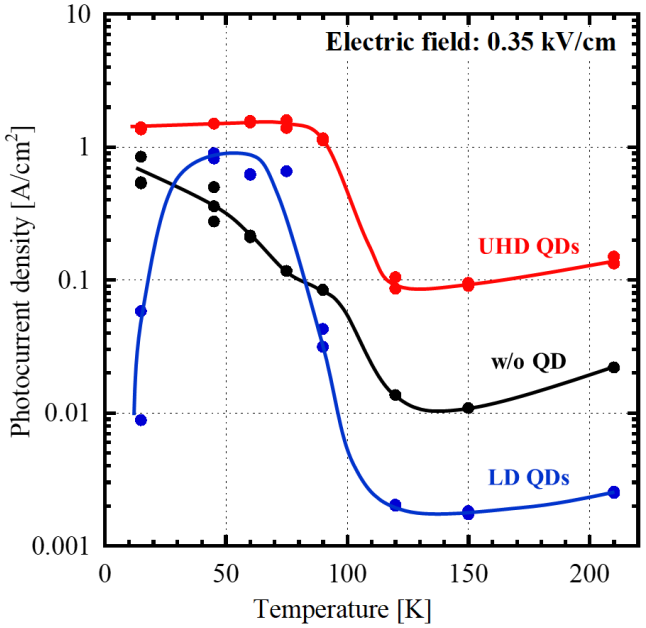

Figure 5.6 Temperature dependence of photocurrent density for UHD QDs, LD QDs, and samples without QDs.

effect. These two-step photoexcited electrons are excited to high-energy states in the GaAs conduction band, significantly contributing to the photocurrent. The differences in photocurrent between UHD QDs and LD QDs are small at low temperatures, which is due to the difference in QD density. As the temperature increases above 80 K, the photocurrent significantly decreases and increases slightly above 150 K. As mentioned in Figure 5.3(c), the photocurrent of LD QDs is lower than that of the sample without QDs due to carrier annihilation via recombination through QD levels at high temperatures.

In contrast, despite the higher QD density, the photocurrent in UHD QDs is about 50 times larger than in LD QDs above 120 K. This is a notable property of UHD QDs. The separation distance between neighboring QDs in UHD QDs is very small, less than about 4 nm. Thus, in-plane carrier transport in the UHD QD layer is facilitated by electronically connected channels of adjacent QDs (partial minibands). This lateral transport of electrons in the UHD QD layer suppresses carrier annihilation due to recombination, contributing significantly to the photocurrent. For typical low-density QD samples, lateral carrier transport in the conduction band is mainly due to hopping conductance via the QDs. However, the photocurrent significantly decreases due to carrier recombination through the QDs at higher temperatures above 100 K.

5.2.5. Summary of photocurrent measurements

This study has thoroughly investigated the photocurrent properties of LD QDs and UHD QDs over a wide temperature range (15 K to 210 K). The results demonstrate significant differences in the behavior of these two types of QDs, particularly in their interaction with light and their electrical response. The photocurrent behavior under varying excitation light power showed quadratic dependence at low temperatures for

UHD QDs, evidencing the two-step photoexcitation effect. At higher temperatures (180 K), all samples exhibited reduced photocurrent due to enhanced recombination processes. Temperature-dependent photocurrent density measurements highlighted UHD QDs with photocurrent density 50 times greater than that of LD QDs above 120 K. This is attributed to the electronically connected channels of adjacent QDs in UHD QDs, facilitating lateral transport and suppresses carrier annihilation due to recombination, contributing significantly to the photocurrent.

5.2. Hall Effect Measurements of InAs/InAsSb In-Plane UHD QDs

5.2.1. Introduction

With sufficient information obtained from PL measurements and photocurrent-voltage measurements, Hall effect measurement provide additional insights into the QD samples, particularly the UHD QD samples with their strong coupling properties. Hall measurements were conducted in the presence of a magnetic field to determine the samples' resistivity, carrier type, majority carrier concentration, Hall voltage and coefficient, and majority carrier mobility. Carrier concentration and mobility are key parameters for understanding the fundamental behavior of carriers in the material and for designing and optimizing various electronic and optoelectronic devices. Understanding carrier dynamics is crucial for the development of high-performance electronic components like high-electron-mobility transistors (HEMTs)[86], which rely on 2DEG (two-dimensional electron gas) [87] structures to achieve high-speed and high-frequency operation.

Hall measurements have been used by researches to study the scattering mechanisms and defects in group III/V materials since stress and strain would occur due to lattice

mismatch of the materials. For instance, the InAs/GaAs superlattice samples with 2DEG channels, it is reported that at low temperatures, very thin InAs layers will form charges at the interface as point defects or dislocations, resulting in scattering by those charges a dominant mechanism[88]. At high temperature, the dominant mechanism is phonon scattering. In Figure 5.7, carrier density increased with rising temperature, while mobility decreased accordingly. It was stated that below 100 K, impurity scattering was more significant, while above 100 K optical phonon scattering was the main mechanism. The benchmark of bulk and epitaxial InAs's electron mobility with respect to electron density is shown in Figure 5.8, which can be used as reference to Hall measurements for InAs QDs in this study.

Recent studies in QD growth techniques have led to the development of UHD QDs, which exhibit strong coupling and minibands formation properties[33,84]. These minibands are expected to enhance carrier transport, leading to high mobility at low electric fields[89], due to the reduced scattering of carriers as they move through the QD layer. However, the electrical properties of InAs QDs (LD QDs and UHD QDs), which utilize Hall measurement technique to obtain desired results, are still not fully understood in the

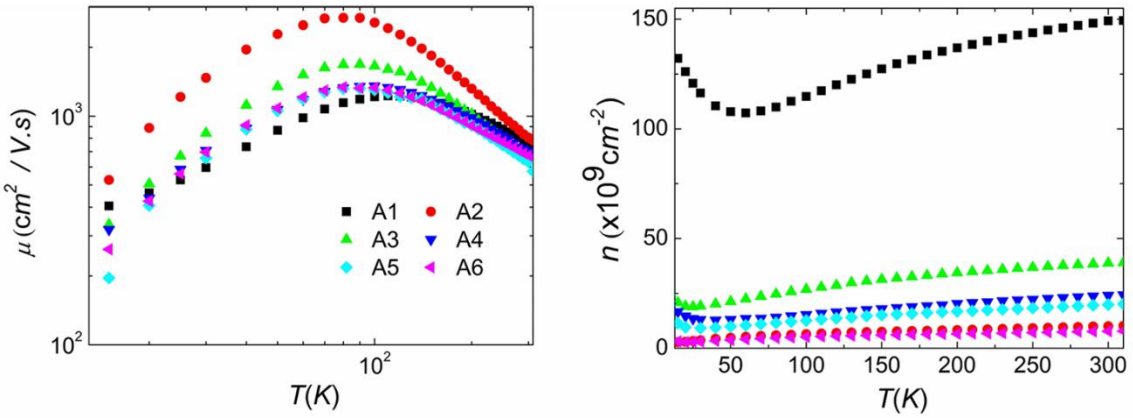

Figure 5.7 Hall measurement results of InAs/GaAs superlattice samples (A2 – A6) and reference one-layer InAs/GaAs sample (A1), under dark condition. Carrier density increased with rising temperature, while mobility decreased accordingly[88].

related field. In this study, the Hall measurement results of UHD QDs were compared with that of LD QDs and reference GaAs samples.

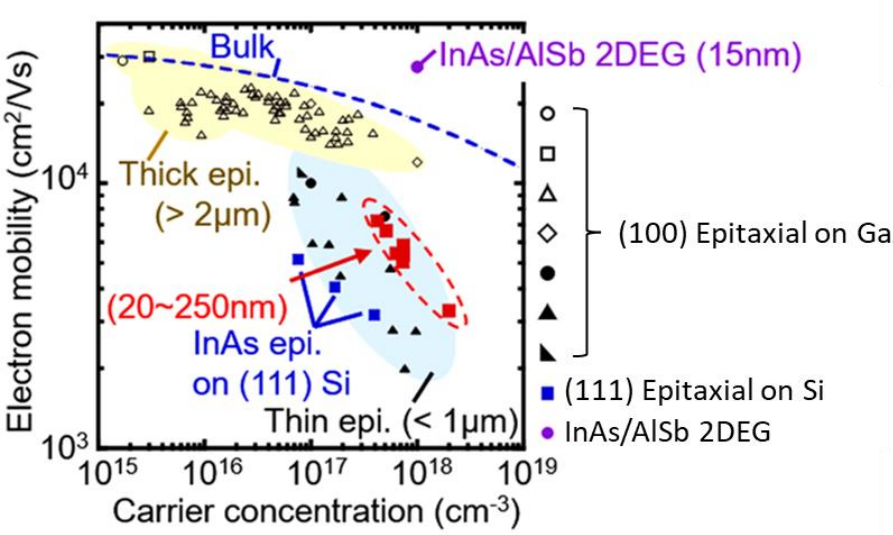

Figure 5.8 The benchmark of bulk and epitaxial InAs's electron mobility with respect to electron density[92].

5.2.2. Experimental Setup

To analyze the electrical properties of the samples, Hall effect measurements were conducted using the Van der Pauw (four-point probe) method under three different light conditions: dark, LED light irradiation, and laser light irradiation. Two GaAs samples—Si-doped GaAs (n-GaAs) and non-doped GaAs (i-GaAs) were measured under dark conditions, while two InAs QD samples—UHD QDs and LD QDs were measured under LED and laser light irradiation, as shown in Figure 5.9. The excitation wavelength for the LED array was 1050 nm, and 980 nm for the laser diode. The absolute maximum power dissipation of 1 piece of LED was 130 mW, with pulsed forward current of 1000 mA, and pulsed forward voltage of 1.9 V. In Hall measurement, laser diode of 980 nm was controlled to provide maximum output power of 20 mW using a power controller. Liquid nitrogen was used to lower the temperature to 78 K. The temperature was then raised

from 78 K to 300 K using helium for heat dissipation and a temperature controller to heat the sample in the cryostat, under a high pressure of less than 4 Pascal. The magnetic field for the Hall measurements was set at 0.35 T, with a constant current of 1×10^{-4} A for n-GaAs sample and 1×10^{-7} A for i-GaAs and InAs QD samples. Before the Hall measurements, indium contacts were shaped into small, hemispherical forms and attached to the four corners of the samples to form ohmic contacts, as shown in Figure 3.10.

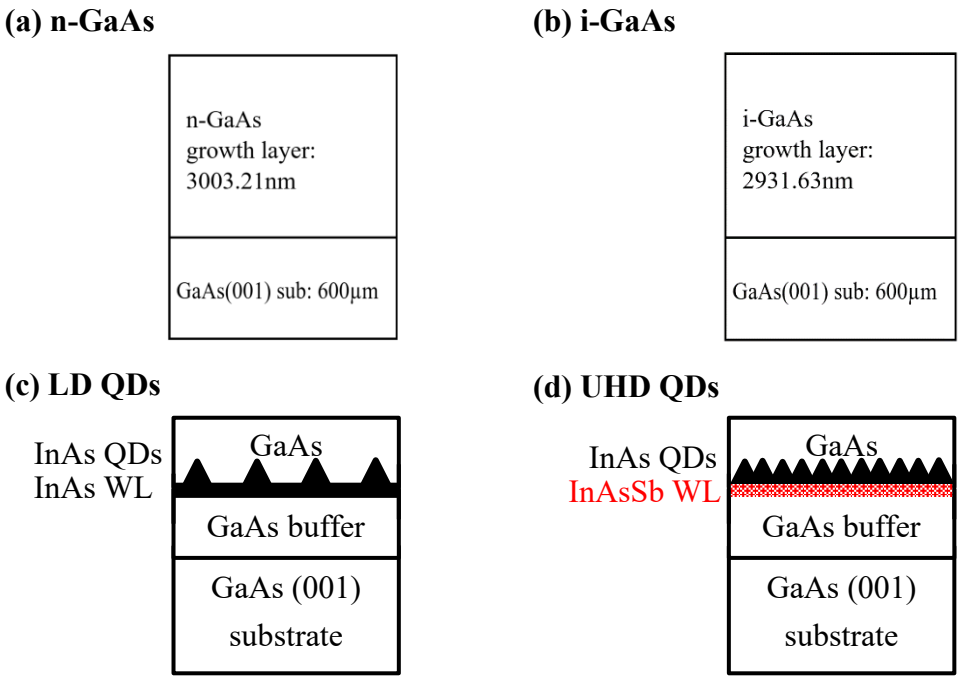

Figure 5.9 Schematic diagrams of Hall measurement sample structures of (a) n-GaAs, (b) i-GaAs, (c) LD QDs and (d) UHD QDs.

5.2.3. Results and Discussions

5.2.3.1. Measurements under dark conditions

Hall measurements were carried out under dark conditions (without light irradiation) for GaAs samples. A silicon-doped GaAs layer, considered an n-GaAs sample, was fabricated on a non-doped GaAs layer and substrate. The thickness of this sample was 3 μm. A constant current of 1×10^{-4} A was applied to the sample, and the resistivity

obtained was as low as 0.01 Ω cm across the temperature range from 80 K to 300 K. Figure 5.10 (a) shows the logarithmic carrier concentration of n-GaAs with respect to temperature. As expected, the doped GaAs sample exhibited a high carrier concentration of $10^{17}\ cm^{-3}$, which increased with rising temperature due to scattering and thermal escape of carriers. Electrons gain sufficient thermal energy to overcome the bandgap and move from the valence band to the conduction band of GaAs. The highest carrier concentration observed was $1.99 \times 10^{17}\ cm^{-3}$ at 280 K, while the lowest was $1.6 \times 10^{17}\ cm^{-3}$ at 80 K. The carrier type was calculated and confirmed as "N," indicating that electrons were the majority carriers contributing to current flow in the sample. Figure 5.10(b) shows the temperature-dependent mobility of n-GaAs, where mobility decreased as temperature increased. Since the density of carriers is inversely proportional to their mobility, the highest carrier concentration corresponded to the lowest mobility of $2540\ cm^2/V \cdot s$, while the highest mobility was $3550\ cm^2/V \cdot s$ at 130 K.

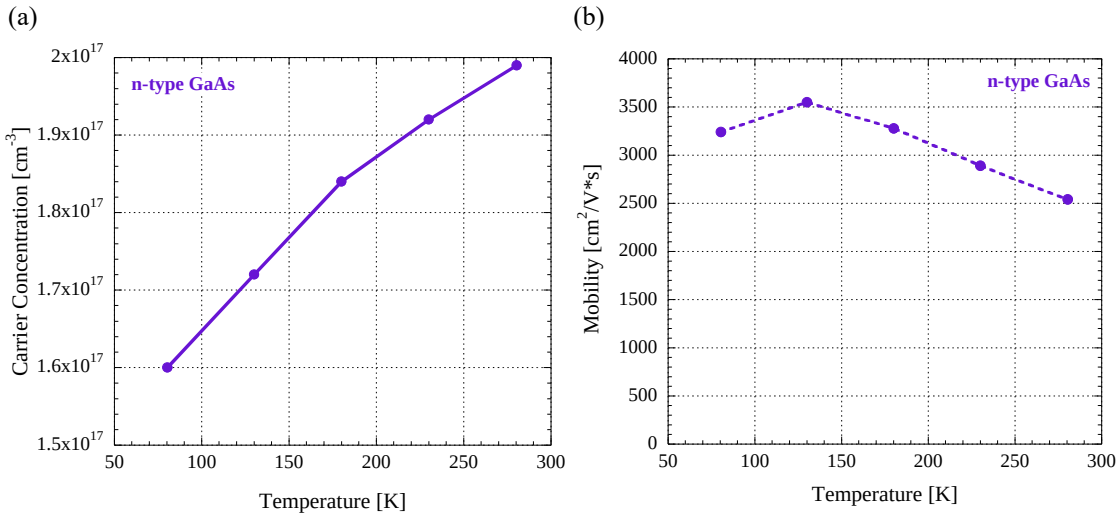

Figure 5.10 Temperature-dependent (a) carrier concentration and (b) mobility of n-GaAs under dark conditions.

Electron mobility is directly related to the mean free time between collisions, which is determined by different scattering mechanisms:

$$\mu_n = \frac{q\tau_c}{m_n^*} \quad [cm^2/V \cdot s] \tag{5.2}$$

As shown in Figure 5.11 (a), lattice scattering, resulting from thermal vibrations of the lattice atoms, was more pronounced. Lattice vibrations increase with temperature and become dominant at high temperatures, leading to a decrease in mobility. Mobility due to lattice scattering typically decreases in proportion to $T^{-\frac{3}{2}}$, however, in this case, the value did not closely match $-\frac{3}{2}$, as the highest temperature was 300 K, compared to 650 K in Figure 5.11(b), which shows electron mobility in silicon as a function of temperature for different donor concentrations[44]. The inset in Figure 5.11(b) illustrates the scattering mechanisms and their temperature-dependent properties related to electron mobility.

On the other hand, a non-doped GaAs layer, referred to as an i-GaAs sample, was fabricated on a non-doped GaAs substrate. The thickness of this sample was 3 µm. A constant current of 1×10^{-7} A was applied to the sample, and the average resistivity

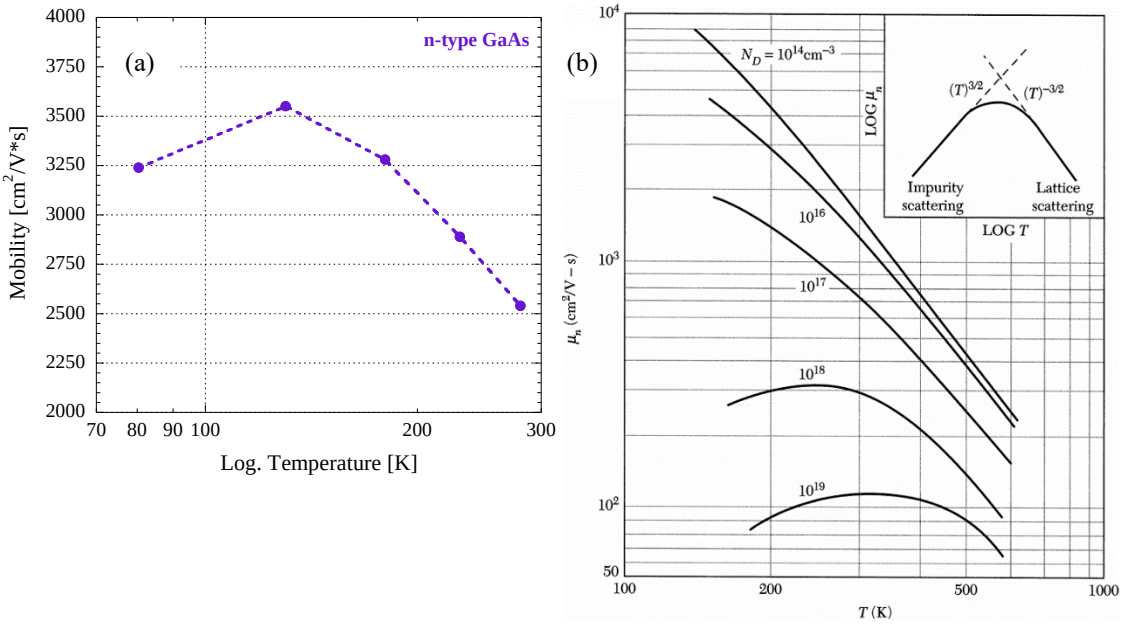

Figure 5.11 (a) Temperature-dependent electron mobility of n-GaAs in log-scale. (b) Electron mobility in silicon of different donor concentrations with respect to temperature. Inset shows the theoretical temperature-dependent electron mobility[44].

obtained was approximately 250 Ω cm across the temperature range from 80 K to 300 K. Figure 5.12(a) shows the logarithmic carrier concentration of i-GaAs as a function of temperature. The i-GaAs sample exhibited carrier concentration ranging from $10^{12}\ cm^{-3}$ to $10^{14}\ cm^{-3}$, which increased with rising temperature due to thermal escape of carriers. The highest carrier concentration observed was $4.81 \times 10^{14}\ cm^{-3}$ at 300 K, while the lowest was $2.45 \times 10^{12}\ cm^{-3}$ at 78 K. The carrier type was unknown from 78 K to 130 K, but above 150 K, the carrier type was identified as "P," indicating that holes were the majority carriers contributing to current flow in the sample at higher temperatures.

Figure 5.12(b) shows the temperature-dependent mobility of i-GaAs, where mobility decreased as temperature increased, consistent with the inverse proportionality between carrier concentration and mobility. Since the carrier type was not confirmed below 130 K, the most reliable measurements were obtained between 150 K to 300 K, with the highest mobility of $1350\ cm^2/V \cdot s$ at 190 K, and the lowest mobility of $212\ cm^2/V \cdot s$ at 300 K. As holes generally have a larger effective mass, their acceleration is more difficult, resulting in lower mobility compared to electrons (as observed in n-GaAs).

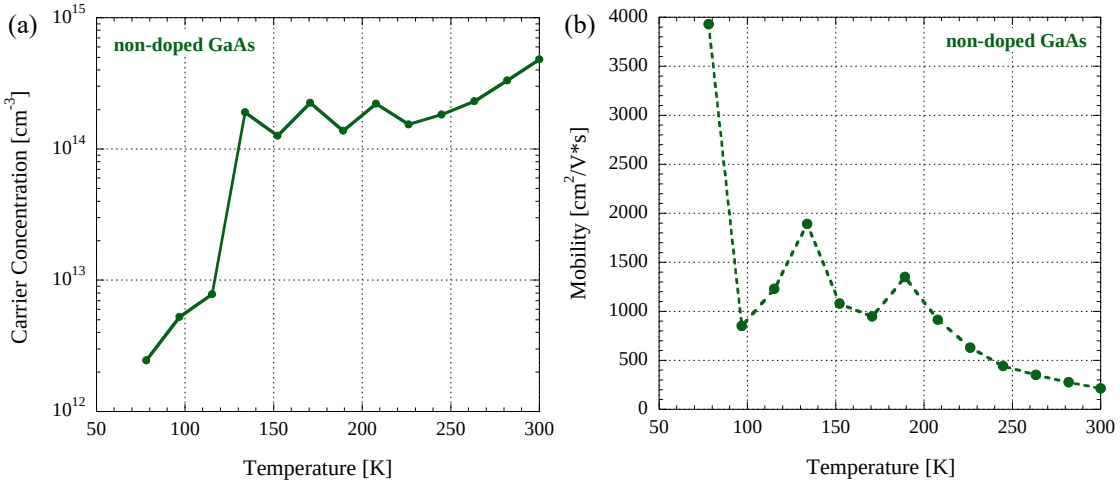

Figure 5.12 Temperature-dependent (a) carrier concentration and (b) mobility of i-GaAs under dark conditions.

5.2.3.2. Measurements under LED light irradiation

Measurements under dark conditions were more challenging for QD samples compared to GaAs samples. This is because QD samples tend to have high resistance due to their small thickness, resulting in instability in Hall measurements and making it difficult to detect the majority carrier concentration. Therefore, an LED array was used as a light source to irradiate both InAs QD samples – LD QDs and UHD QDs, to assist in carrier excitation. The thickness of LD QDs was 0.34 μm, while that of UHD QDs was 0.27 μm. Table 5.1 presents the Hall measurement results for LD QDs, and Table 5.2 provides the results for UHD QDs. These tables include details on resistivity, Hall voltage, Hall coefficient, carrier concentration, mobility, carrier type, and F value.

A constant current of 1×10^{-7} A was applied to both samples. Resistivity increased with temperature, ranging from 80 K to 300 K, with the highest resistivity of 702 Ωcm for LD QDs and 46.5 Ωcm for UHD QDs. The higher resistivity observed in LD QDs is attributed to phonon scattering at elevated temperatures. According to calculations based on Hall voltage and Hall coefficient, the negative signs obtained indicate that the carrier types for both QD samples were identified as "N," meaning electrons were the majority carriers contributing to the current flow in the samples. This is because holes, which have a higher effective mass, are confined within the QDs. Additionally, light with a wavelength of 1050 nm (1.18 eV) can excite electrons confined within the QDs. In contrast, the band gap energy of the GaAs layer is higher (~1.5 eV), so light at this wavelength does not excite carriers in the GaAs layer. The F-values, or balance factors, which represent the consistency of the measurements (with 0 being the worst and 1 being the best), were optimal across the temperature range from 80 K to 200 K.

Table 5.1 Hall measurement results of LD QDs under LED light irradiation.

Temperature	**Resistivity (Ωcm)**	**Hall Voltage [V]**	**Hall Coefficient $[cm^3/C]$**	**Carrier Concentration $[cm^{-3}]$**	**Mobility $[cm^2/V \cdot s]$**	**Carrier Type**	**F value**
80.25	1.00	-0.0019	-1.89×10^4	3.30×10^{14}	18874	N	0.999
100.51	9.09	-0.0115	-1.12×10^5	5.56×10^{13}	12343	N	1
120.31	24.08	-0.0300	-2.92×10^5	2.14×10^{13}	12119	N	1
140.11	59.73	-0.0813	-7.90×10^5	7.90×10^{12}	13225	N	0.997
160.14	169.39	-0.1900	-1.85×10^6	3.38×10^{12}	10902	N	1
179.79	347.2526	-0.34429	-3.35×10^6	1.87×10^{12}	9635.642	N	1
199.99	702.1766	-0.22933	-2.67×10^6	2.34×10^{12}	3807.169	N	1

Figure 5.13(a) shows the logarithmic carrier concentration of LD QDs and UHD QDs as a function of temperature. For both samples, the carrier concentration decreased with rising temperature, which is contrary to the behavior observed in n-GaAs. At 80 K, the highest carrier concentration recorded was $3.3 \times 10^{14}\ cm^{-3}$ for LD QDs and $2.46 \times 10^{15}\ cm^{-3}$ for UHD QDs. The difference in carrier concentration between LD QDs and UHD QDs is due to the QD densities, with UHD QDs having a QD density 25 times higher than that of LD QDs. As temperature increases, the thermal velocity of the carriers rises, which may lead to the capture of free electrons by empty QDs. This trapping of electrons within the QDs could explain the observed decrease in overall carrier concentration at higher temperatures.

Table 5.2 Hall measurement results of UHD QDs under LED light irradiation.

Temperature	**Resistivity (Ωcm)**	**Hall Voltage [V]**	**Hall Coefficient $[cm^3/C]$**	**Carrier Concentration $[cm^{-3}]$**	**Mobility $[cm^2/V \cdot s]$**	**Carrier Type**	**F value**
80.49	0.113	-0.00033	-2.53×10^3	2.46×10^{15}	22500	N	1
100.00	0.919	-0.00244	-1.88×10^4	3.32×10^{14}	20500	N	1
120.12	2.92	-0.00624	-4.82×10^4	1.30×10^{14}	16500	N	1
140.04	6.35	-0.0116	-8.93×10^4	6.99×10^{13}	14100	N	1
159.81	13.6	-0.0198	-1.53×10^5	4.08×10^{13}	11300	N	1
180.04	24.4	-0.044	-3.39×10^5	1.84×10^{13}	13900	N	0.999
200.08	46.5	-0.0836	-6.45×10^5	9.67×10^{12}	13900	N	0.997

Conversely, the electron mobility of both QD samples, shown in Figure 5.13(b), exhibited a decrease and then stable behavior across different temperature ranges. UHD QDs, with an exceptionally high mobility of $22500\ cm^2/V \cdot s$ at 80 K, experienced a gradual decrease in electron mobility with increasing temperature, followed by a slight increase, stabilizing at $13900\ cm^2/V \cdot s$ by 200 K. The highest mobility for LD QDs was $18874\ cm^2/V \cdot s$ at 80 K, which is lower than that of UHD QDs. A significant drop in mobility was observed from 80 K to 100 K for LD QDs, followed by stable mobility from 100 K to 140 K, and a further decrease to the lowest mobility of $3807\ cm^2/V \cdot s$ at 200 K.

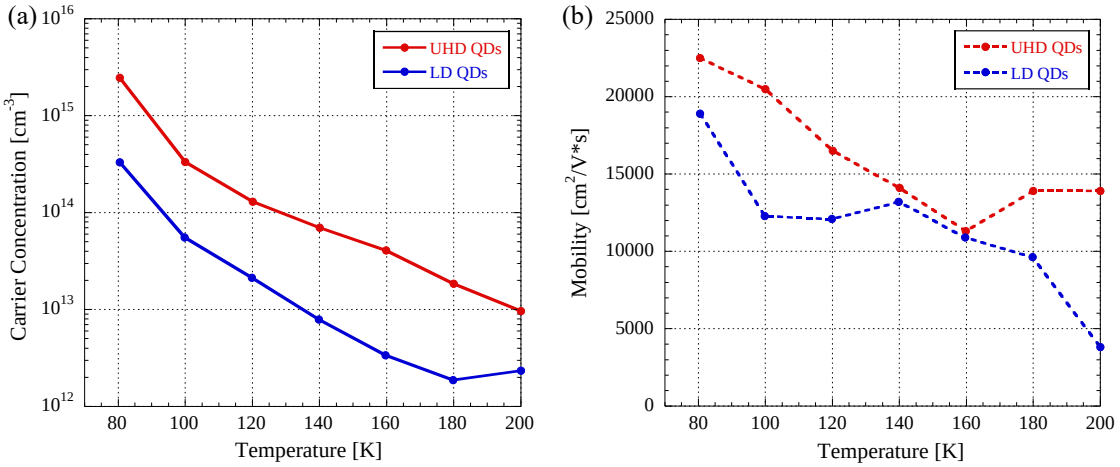

Figure 5.13 Temperature-dependent (a) carrier concentration and (b) mobility of UHD QDs and LD QDs under LED light irradiation.

The high resistance observed in QD samples may be attributed to the presence of surface states, which can act as traps for electrons. These surface states capture electrons, leading to recombination events that can reduce the overall carrier concentration within the QDs. Despite the potential drawbacks of surface states, UHD QDs exhibit a mobility advantage. Due to their smaller size and the shorter distance between adjacent QDs, UHD QDs enable stronger coupling and the formation of a miniband, which facilitates the movement of electrons along the continuous band within the QD layer. This results in higher carrier mobility compared to LD QDs. The impact of surface states on measurements might be more pronounced than the effects of the actual QD layer properties. Additionally, the reasons for the decrease in carrier concentration and mobility with increasing temperature in both QD samples remain unclear due to the complex nature of the sample structures and carrier transport mechanisms.

5.2.3.3. Measurements under laser light irradiation

To gain a better understanding of QD samples under light irradiation, additional measurements were conducted using a laser diode as the light source, in place of the LED

array. The laser diode provides enhanced coherence and a more focused beam compared to the LED array. The measurement parameters, including sample thickness, current, and magnetic field, were consistent with those used in measurements under LED light. However, in this case, a laser with a wavelength of 980 nm (1.265 eV) was used instead of the LED array. The 980 nm light excited carriers through the ground state transition in UHD QDs and the excited state transition in LD QDs. The results of Hall effect measurements conducted over a temperature range from 140 K to 300 K are presented in Table 5.3 for LD QDs and Table 5.4 for UHD QDs. At lower temperatures, Hall measurements under laser light irradiation were unstable, and the majority carriers could not be detected; therefore, results at these temperatures are not included in the tables.

Resistivity increased with temperature, reaching a maximum of 47.7 Ωcm for LD QDs at 300 K and 9.9 Ωcm for UHD QDs at 280 K. The resistivity of both QD samples was significantly lower than the measurements taken under LED light irradiation. The majority carriers in both samples were electrons, as holes with heavier effective mass are strongly confined within the QDs. Figure 5.14(a) shows the logarithmic carrier concentration of LD QDs and UHD QDs as a function of temperature. Similarly, the carrier concentration decreased with rising temperature. At 140 K, the highest carrier concentration observed was $7.53 \times 10^{14}\ cm^{-3}$ for LD QDs and $3.08 \times 10^{15}\ cm^{-3}$ for UHD QDs. In addition to the effect of QD density on carrier concentration, fewer QDs were photoexcited by the 980 nm light in the case of LD QDs, as their carriers are selectively excited between discrete QD energy levels. In contrast, for UHD QDs, the in-plane miniband of the ground states began to form at 140 K. This formation of a continuous energy miniband enhances optical absorption of the 980 nm light in UHD QDs, resulting in a higher carrier concentration compared to that in LD QDs. The electron

Table 5.3 Hall measurement results of LD QDs under laser light irradiation.

Temperature	**Resistivity (Ωcm)**	**Hall Voltage [V]**	**Hall Coefficient $[cm^3/C]$**	**Carrier Concentration $[cm^{-3}]$**	**Mobility $[cm^2/V \cdot s]$**	**Carrier Type**	**F value**
139.74	0.487845	-0.0009	-8.29×10^3	7.53×10^{14}	16984	N	1
159.62	1.222705	-0.0020	-1.9×10^4	3.29×10^{14}	15516	N	1
179.81	2.786534	-0.0039	-3.9×10^4	1.60×10^{14}	13984	N	1
200.04	5.450759	-0.0070	-6.8×10^4	9.18×10^{13}	12476	N	1
219.86	9.513112	-0.0105	-1.03×10^5	6.09×10^{13}	10776	N	1
239.90	16.45515	-0.0145	-1.41×10^5	4.43×10^{13}	8554	N	1
259.97	24.23998	-0.0148	-1.44×10^5	4.33×10^{13}	5949	N	0.995
279.97	35.38471	-0.0147	-1.43×10^5	4.36×10^{13}	4042	N	0.999
299.88	47.67435	-0.0114	-1.12×10^5	5.56×10^{13}	2355	N	0.998

mobility of both QD samples, shown in Figure 5.14(b), decreased across different temperature ranges. The highest mobility for LD QDs was $16984\ cm^2/V \cdot s$ at 140 K, while for UHD QDs, it was $23338\ cm^2/V \cdot s$ at the same temperature. For LD QDs, the photoexcited electrons transport via hopping conduction between the QDs and the GaAs conduction band. In contrast, for UHD QDs, the photoexcited electrons within the ground state miniband move through band conduction. Therefore, the miniband transport of UHD QDs is expected to have higher mobility than hopping conduction of LD QDs. Despite

Table 5.4 Hall measurement results of UHD QDs under laser light irradiation.

Temperature	Resistivity (Ωcm)	Hall Voltage [V]	Hall Coefficient $[cm^3/C]$	Carrier Concentration $[cm^{-3}]$	Mobility $[cm^2/V \cdot s]$	Carrier Type	F value
140.83	0.0867	-0.0003	-2024	3.08×10^{15}	23338	N?	1
160.71	0.2202	-0.0005	-3866	1.61×10^{15}	17555	N	1
181.01	0.4116	-0.0009	-6874	9.08×10^{14}	16700	N	0.999
200.94	0.8149	-0.0012	-9272	6.73×10^{14}	11378	N	1
220.74	0.9244	-0.0015	-11407	5.47×10^{14}	12340	N	1
240.57	1.3225	-0.0018	-14081	4.43×10^{14}	10647	N	0.999
260.59	4.4595	-0.0021	-16624	3.76×10^{14}	3728	N	0.992
280.51	9.9075	-0.0020	-15604	4×10^{14}	1575	N?	0.988

this, a decrease in electron mobility with increasing temperature was observed for both types of QDs. This decrease is likely due to enhanced phonon scattering at higher temperatures. However, the exact relationship between the decreasing carrier concentration and decreasing mobility remains unclear based on these measurements.

Overall, comparing the measurements under LED light irradiation with those under laser light irradiation reveals significant improvements in Hall results when using a laser as the light source. Specifically, measurements with the laser showed much lower resistivity, higher carrier concentration, and higher mobility. This improvement is due to the laser's highly focused and coherent beam, which effectively excites carriers within the QDs and generates more free charge carriers. Increased carrier generation results in lower resistivity by providing more charge carriers for electrical conduction. However, each

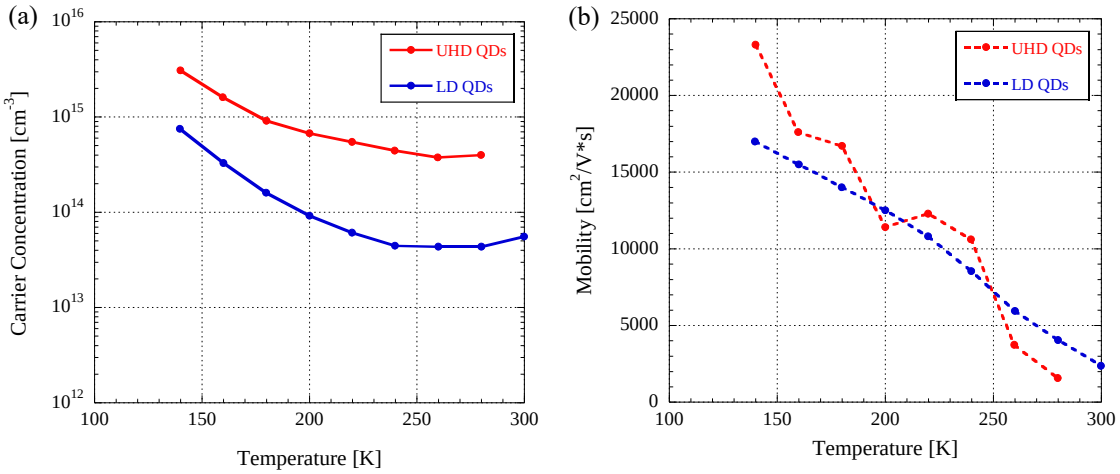

Figure 5.14 Temperature-dependent (a) carrier concentration and (b) mobility of UHD QDs and LD QDs under laser light irradiation

light source has its advantages and disadvantages. LED light irradiation provided more stable measurements at lower temperatures but resulted in higher resistivity as the temperature increased. In contrast, while laser light was less effective at lower temperatures, its highly coherent and focused beam led to better outcomes in terms of resistivity, carrier concentration, and mobility of the QD samples at higher temperatures.

5.2.3.4. Summary of Hall measurements

This study explored the Hall effect in InAs/InAsSb UHD QDs, comparing them with LD QDs and reference GaAs samples. Hall effect measurements, conducted using the Van der Pauw method under various light conditions (dark, LED, and laser), provided information regarding the resistivity, carrier type, concentration, Hall voltage, and mobility of these samples. The research found that laser light irradiation generally yielded better results in terms of resistivity and carrier mobility at higher temperatures compared to LED light, which, while stable at lower temperatures yet higher resistivity. UHD QDs demonstrated higher carrier mobility due to their smaller size and enhanced coupling,

leading to miniband formation that facilitated electron transport. Despite potential issues with surface states acting as electron traps, UHD QDs showed superior performance compared to LD QDs.

5.3. Chapter Summary

This study provides analysis of both the photocurrent and Hall effect properties of InAs/InAsSb UHD QDs versus InAs LD QDs. The photocurrent study revealed that UHD QDs exhibited a quadratic dependence on light power at low temperatures, indicating a two-step photoexcitation effect. Notably, UHD QDs demonstrated a photocurrent density 50 times greater than LD QDs above 120 K, attributed to minibands that enhance lateral transport and reduce carrier annihilation. In parallel, Hall effect measurements illustrated that UHD QDs outperformed LD QDs in carrier mobility and resistivity, due to minibands which facilitate more efficient electron transport.

Chapter 6. Conclusions

Chapter 1 provides a comprehensive overview of the research background and objectives, highlighting the significance of semiconductor QDs in various technological applications. The chapter highlights the importance of understanding strong QD coupling and miniband formation in UHD QDs, offering valuable insights for the development of advanced QD-based devices with enhanced performance and functionality.

Chapter 2 focuses on the characteristics and fabrication processes of InAs QDs grown on InAsSb wetting layers using MBE. The self-assembly process driven by lattice mismatch and strain is explored, highlighting the transition from 2D to 3D growth and the formation of high-quality QDs. The introduction of Sb into the WL is emphasized for its role in enhancing QD density and uniformity, crucial for improving the performance of QD-based applications.

Chapter 3 details the comprehensive process of preparing, growing, and analyzing high-quality GaAs and InAs quantum dot samples using MBE and various characterization techniques. From the growth of GaAs buffer layers to the deposition of InAs QDs and subsequent analyses using AFM, PL, J-V measurements, and Hall effect analyses.

Chapter 4 presents the findings from the thorough investigation of the temperature-dependent phenomena exhibited by UHD QDs, focusing on PL spectra, decay times, and FWHM variations. The observation of strong coupling of UHD QDs and the dynamic process of miniband formation stresses on the unique electronic interactions between the closely-separated adjacent QDs, in particularly the process of energy shifting in different QD states, where the coupling of QDs and the formation of minibands initiate from the higher energy side (ESs) at lower temperatures, gradually progressing towards the lower

energy side (GSs) as the temperature increases.

First section of chapter 5 demonstrates the photocurrent properties of LD QDs and UHD QDs over a wide temperature range, revealing significant differences in their behavior and interaction with irradiation light. The observation from temperature-dependent photocurrent density measurements highlighted UHD QDs with a photocurrent density 50 times greater than that of LD QDs above 120 K, underscore the importance of miniband formation and carrier transport mechanisms. Second section of chapter 5 concludes the experimental analyses by comparing the electrical properties of LD QDs and UHD QDs using the Hall effect technique under light irradiation. The higher mobility observed in UHD QDs, attributed to miniband transport, presents their superior performance compared to LD QDs.

All in all, these analyses confirmed strong coupling between QDs, leading to the formation of minibands within the layer. Understanding this strong coupling and miniband formation in UHD QDs opens exciting avenues for researchers to explore the potential of self-assembled InAs QDs, particularly in-plane UHD QDs. With their exceptional PL properties and high photocurrent observed under various temperatures and light excitation intensities, UHD QD samples hold significant promise for integration into intermediate-band solar cells or other QD solar cell designs. This research on UHD QDs represents a significant step forward in developing next-generation solar cells with enhanced efficiency and cost-effectiveness, ultimately contributing to a cleaner and more sustainable energy future.

Bibliography

[1] M.A. Reed, J.N. Randall, R.J. Aggarwal, R.J. Matyi, T.M. Moore, and A.E. Wetsel, Observation of Discrete Electronic States in a Zero-Dimensional Semiconductor Nanostructure (1988).

[2] V. Mikhelashvili, O. Eyal, I. Khanonkin, S. Banyoudeh, V. Sichkovskyi, J.P. Reithmaier, and G. Eisenstein, "On the relationship between electrical and electro-optical characteristics of InAs/InP quantum dot lasers," J Appl Phys 124(5), (2018).

[3] M. Tanaka, K. Banba, T. Sogabe, and K. Yamaguchi, "InAs/GaAsSb in-plane ultrahigh-density quantum dot lasers," Applied Physics Express 14(12), (2021).

[4] Y. Nakazato, N. Miyashita, and K. Yamaguchi, "Resonant tunneling injection of electrons through double stacked GaAs/InAs quantum dots with nanohole electrode," Jpn J Appl Phys 62(11), (2023).

[5] A.D. Stiff-Roberts, "Quantum-dot infrared photodetectors: a review," J Nanophotonics 3(1), 031607 (2009).

[6] H.C. Liu, M. Gao, J. McCaffrey, Z.R. Wasilewski, and S. Fafard, "Quantum dot infrared photodetectors," Appl Phys Lett 78(1), 79–81 (2001).

[7] S.J. Xu, S.J. Chua, T. Mei, X.C. Wang, X.H. Zhang, G. Karunasiri, W.J. Fan, C.H. Wang, J. Jiang, S. Wang, and X.G. Xie, "Characteristics of InGaAs quantum dot infrared photodetectors," Appl Phys Lett 73(21), 3153–3155 (1998).

[8] S.Y. Lin, Y.J. Tsai, and S.C. Lee, "Transport characteristics of InAs/GaAs quantum-dot infrared photodetectors," Appl Phys Lett 83(4), 752–754 (2003).

[9] A. Carbone, R. Introzzi, and H.C. Liu, "Photo and dark current noise in self-assembled quantum dot infrared photodetectors," Infrared Phys Technol 52(6), 260–263 (2009).

[10] A. Luque, A. Martí, and C. Stanley, "Understanding intermediate-band solar cells," Nat Photonics 6(3), 146–152 (2012).

[11] C.R. Stanley, Intermediate Intermediate--Band Solar Cells and Band Solar Cells and the Quantum Dot Approach the Quantum Dot Approach (2004).

[12] A. Martí, E. Antolín, C.R. Stanley, C.D. Farmer, N. López, P. Díaz, E. Cánovas, P.G. Linares, and A. Luque, "Production of photocurrent due to intermediate-to-conduction-band transitions: A demonstration of a key operating principle of the intermediate-band solar cell," Phys Rev Lett 97(24), (2006).

[13] Y. Okada, N.J. Ekins-Daukes, T. Kita, R. Tamaki, M. Yoshida, A. Pusch, O. Hess, C.C. Phillips, D.J. Farrell, K. Yoshida, N. Ahsan, Y. Shoji, T. Sogabe, and J.F. Guillemoles, "Intermediate band solar cells: Recent progress and future directions," Appl Phys Rev 2(2), (2015).

[14] S. Heshmati, and S. Golmohammadi, Performance Analysis of Single Quantum Dots and Couple Quantum Dots at Intermediate Band Solar Cells (2013).
[15] R. Tamaki, Y. Shoji, Y. Okada, and K. Miyano, "Spectrally resolved intraband transitions on two-step photon absorption in InGaAs/GaAs quantum dot solar cell," Appl Phys Lett 105(7), (2014).
[16] A. Luque, and A. Martí, "Increasing the Efficiency of Ideal Solar Cells by Photon Induced Transitions at Intermediate Levels," Phys Rev Lett 78(26), 5014–5017 (1997).
[17] A. Martí, N. López, E. Antolín, E. Cánovas, A. Luque, C.R. Stanley, C.D. Farmer, and P. Díaz, "Emitter degradation in quantum dot intermediate band solar cells," Appl Phys Lett 90(23), (2007).
[18] H. Asahi, Y. Horikoshi, and K. Yamaguchi, "Molecular Beam Epitaxy: Materials and Applications for Electronics and Optoelectronics," (2019).
[19] K. Yamaguchi, and T. Kanto, "Self-assembled InAs quantum dots on GaSb/GaAs(0 0 1) layers by molecular beam epitaxy," in J Cryst Growth, (2005).
[20] K. Sameshima, T. Sano, and K. Yamaguchi, "Self-formation of ultrahigh-density (1012cm-2) InAs quantum dots on InAsSb/GaAs(001) and their photoluminescence properties," Applied Physics Express 9(7), (2016).
[21] S. Oikawa, A. Makaino, T. Sogabe, and K. Yamaguchi, "Growth Process and Photoluminescence Properties of In-Plane Ultrahigh-Density InAs Quantum Dots on InAsSb/GaAs(001)," Phys Status Solidi B Basic Res 255(4), (2018).
[22] T. Kanto, and K. Yamaguchi, "In-plane self-arrangement of high-density InAs quantum dots on GaAsSb/GaAs (001) by molecular beam epitaxy," in J Appl Phys, (2007).
[23] N. Kakuda, T. Yoshida, and K. Yamaguchi, "Sb-mediated growth of high-density InAs quantum dots and GaAsSb embedding growth by MBE," Appl Surf Sci 254(24), 8050–8053 (2008).
[24] K. Sakamoto, Y. Kondo, K. Uchida, and K. Yamaguchi, "Quantum-dot density dependence of power conversion efficiency of intermediate-band solar cells," J Appl Phys 112(12), (2012).
[25] Miyuki Shiokawa, Edes Saputra, Katsuyoshi Sakamoto, and Koichi Yamaguchi, Long Carrier Lifetime in Ultrahigh-Density InAs Quantum-Dot Sheet of Intermediate Band Solar Cells (2013 IEEE 39th Photovoltaic Specialists Conference (PVSC), 2013).
[26] R. Suzuki, K. Terada, K. Sakamoto, T. Sogabe, and K. Yamaguchi, "Low sunlight concentration properties of InAs ultrahigh-density quantum-dot solar cells," Jpn J Appl Phys 58(7), (2019).
[27] S. Tomic, T. Sogabe, and Y. Okada, "In-plane coupling effect on absorption coefficients of-InAs/GaAs quantum dots arrays for intermediate band solar cell," Progress in

Photovoltaics: Research and Applications 23(5), 546–558 (2015).
[28] K. Ryczko, G. Sęk, and J. Misiewicz, "The effect of structural parameters on the in-plane coupling between quantum dashes of a dense ensemble in the InAs-InP material syste," J Appl Phys 115(21), (2014).
[29] A. Takahashi, T. Ueda, Y. Bessho, Y. Harada, T. Kita, E. Taguchi, and H. Yasuda, "One-dimensional miniband formation in closely stacked InAs/GaAs quantum dots," Phys Rev B Condens Matter Mater Phys 87(23), (2013).
[30] M.M. Sobolev, M.S. Buyalo, V.N. Nevedomskiy, Y.M. Zadiranov, R. V. Zolotareva, A.P. Vasil'ev, V.M. Ustinov, and E.L. Portnoi, "Emission spectra of a laser based on an In(Ga)As/GaAs quantum-dot superlattice," Semiconductors 49(10), 1335–1340 (2015).
[31] T. Sugaya, T. Amano, M. Mori, and S. Niki, "Miniband formation in InGaAs quantum dot superlattice," Appl Phys Lett 97(4), (2010).
[32] H. Nakatani, T. Kita, O. Kojima, O. Wada, K. Akahane, and M. Tsuchiya, "Photoluminescence dynamics of coupled quantum dots," J Lumin 128(5–6), 975–977 (2008).
[33] S. Tatsugi, N. Miyashita, T. Sogabe, and K. Yamaguchi, "Demonstration of in-plane miniband formation in InAs/InAsSb ultrahigh-density quantum dots by analysis of temperature dependence of photoluminescence," Jpn J Appl Phys 61(10), (2022).
[34] Y. Masumoto, and T. Takagahara, "Semiconductor Quantum Dots Physics, Spectroscopy and Applications," (2002).
[35] K. Murawski, E. Gomółka, M. Kopytko, K. Grodecki, K. Michalczewski, Kubiszyn, W. Gawron, P. Martyniuk, A. Rogalski, and J. Piotrowski, "Bandgap energy determination of InAsSb epilayers grown by molecular beam epitaxy on GaAs substrates," Progress in Natural Science: Materials International 29(4), 472–476 (2019).
[36] P.T. Webster, N.A. Riordan, S. Liu, E.H. Steenbergen, R.A. Synowicki, Y.H. Zhang, and S.R. Johnson, "Measurement of InAsSb bandgap energy and InAs/InAsSb band edge positions using spectroscopic ellipsometry and photoluminescence spectroscopy," J Appl Phys 118(24), (2015).
[37] T. Manyk, K. Murawski, K. Michalczewski, K. Grodecki, J. Rutkowski, and P. Martyniuk, "Method of electron affinity evaluation for the type-2 InAs/InAs1−xSbx superlattice," J Mater Sci 55(12), 5135–5144 (2020).
[38] S.-H. Wei, and A. Zunger, InAsSb/InAs: A Type-I or a Type-II Band Alignment (1995).
[39] K. Yamaguchi, K. Yujobo, and T. Kaizu, Stranski-Krastanov Growth of InAs Quantum Dots with Narrow Size Distribution (2000).
[40] K.E. Sautter, K.D. Vallejo, and P.J. Simmonds, "Strain-driven quantum dot self-assembly by molecular beam epitaxy," J Appl Phys 128(3), (2020).

[41] E. Koichi Yamaguchi, T. Kaiat Ryo Otsubo, and S. Iwasaki, Self Size-Limiting Growth of Uniform InAs Quantum Dots by Molecular Beam (2002).
[42] N. Kakuda, and K. Yamaguchi, "Coarsening process of high-density InAs quantum dots on Sb-irradiated GaAs," Jpn J Appl Phys 57(4), (2018).
[43] N. Kakuda, T. Kaizu, M. Takahasi, S. Fujikawa, and K. Yamaguchi, "Time-resolved X-ray diffraction measurements of high-density InAs quantum dots on Sb/GaAs layers and the suppression of coalescence by Sb-irradiated growth interruption," Jpn J Appl Phys 49(9 PART 1), (2010).
[44] S.M. Sze, "Semiconductor Devices, Physics and Technology" (Wiley, 2002).
[45] J.R. Arthur, Molecular Beam Epitaxy, Surface Science 500, 189–217 (2002).
[46] S. Hasegawa, "Reflection High-Energy Electron Diffraction" in Characterization of Materials (Wiley, 2012).
[47] G. Binnig, C.F. Quate, and C. Gerber, "Atomic force microscope," Phys Rev Lett 56(9), 930–933 (1986).
[48] B. Cappella, and G. Dietler, Force-Distance Curves by Atomic Force Microscopy (1999).
[49] T.H. Gfroerer, "Photoluminescence in Analysis of Surfaces and Interfaces," in Encyclopedia of Analytical Chemistry, (Wiley, 2000).
[50] E.H. Hall, On a New Action of the Magnet on Electric Currents (1879).
[51] L. J. van der Pauw, "A method of measuring the resistivity and Hall coefficient on lamellae of arbitrary shape," Philips Tech Review 20(8), 220–24 (1958).
[52] L. J. van der Pauw, "A method of measuring the resistivity and Hall coefficient on lamellae of arbitrary shape," Philips Res.Repts 13(1), 1–9 (1958).
[53] TOYO Corporation, ResiTest8300 Software Instruction Manual (2011).
[54] J. Liu, Q. Yuan, B. Liang, Q. Yan, Y. Wang, C. Wang, S. Wang, G. Fu, Y.I. Mazur, M.E. Ware, and G.J. Salamo, "Photoluminescence characterization of wetting layer and carrier dynamics for coupled InGaAs/GaAs surface quantum dot pair structures," Opt Express 28(14), 20704 (2020).
[55] S. Tomić, "Intermediate-band solar cells: Influence of band formation on dynamical processes in InAs/GaAs quantum dot arrays," Phys Rev B Condens Matter Mater Phys 82(19), (2010).
[56] M. Bayer, P. Hawrylak, K. Hinzer, S. Fafard, M. Korkusinski, Z.R. Wasilewski, O. Stern, and A. Forchel, Coupling and Entangling of Quantum States in Quantum Dot Molecules (2001).
[57] K. Goshima, N. Tsuda, K. Inukai, T. Amano, and T. Sugaya, "Interdot spacing dependence of electronic structure and properties of multistacked InGaAs quantum dots fabricated without strain compensation technique," in Jpn J Appl Phys, (Japan Society of

Applied Physics, 2018).
[58] S. Rudin, T.L. Reinecke, and B. Segall, Temperature-Dependent Exciton Linewidths in Semiconductors (1990).
[59] C. Kammerer, G. Cassabois, C. Voisin, C. Delalande, P. Roussignol, A. Lemaître, and J.M. Gérard, "Efficient acoustic phonon broadening in single self-assembled InAs/GaAs quantum dots," Phys Rev B Condens Matter Mater Phys 65(3), 333131–333134 (2002).
[60] M. Bayer, and A. Forchel, "Temperature dependence of the exciton homogeneous linewidth in (formula presented) self-assembled quantum dots," Phys Rev B Condens Matter Mater Phys 65(4), 1–4 (2002).
[61] I. Favero, G. Cassabois, R. Ferreira, D. Darson, C. Voisin, J. Tignon, C. Delalande, G. Bastard, P. Roussignol, and J.M. Gérard, "Acoustic phonon sidebands in the emission line of single InAs/GaAs quantum dots," Phys Rev B Condens Matter Mater Phys 68(23), (2003).
[62] S. Lan, K. Akahane, K.-Y. Jang, T. Kawamura, Y. Okada, M. Kawabe, T. Nishimura, and O. Wada, Two-Dimensional In 0.4 Ga 0.6 As/GaAs Quantum Dot Superlattices Realized by Self-Organized Epitaxial Growth (Publication Board, 1999).
[63] Atsushi Tackeuchi, Yoshiaki Nakata, Shunichi Muto, Yoshihiro Sugiyama, Tatsuya Usuki, Yuji Nishikawa, Naoki Yokoyama and Osamu Wada, Jpn. J. Appl. Phys. 34(L1439), (1995).
[64] Y.P. Varshni, Temperature Dependence of The Energy Gap in Semiconductors, Physica 34 149-154 (1967).
[65] S. Sanguinetti, T. Mano, M. Oshima, T. Tateno, M. Wakaki, and N. Koguchi, "Temperature dependence of the photoluminescence of InGaAs/GaAs quantum dot structures without wetting layer," Appl Phys Lett 81(16), 3067–3069 (2002).
[66] Y.I. Mazur, B.L. Liang, Z.M. Wang, G.G. Tarasov, D. Guzun, and G.J. Salamo, "Development of continuum states in photoluminescence of self-assembled InGaAsGaAs quantum dots," J Appl Phys 101(1), (2007).
[67] T. Mano, R. Nötzel, Q. Gong, T. V. Lippen, G.J. Hamhuis, T.J. Eijkemans, and J.H. Wolter, "Temperature-dependent photoluminescence of self-assembled (In,Ga)As quantum dots on GaAs (100): Carrier redistribution through low-energy continuous states," Japanese Journal of Applied Physics, Part 1: Regular Papers and Short Notes and Review Papers 44(9 A), 6829–6832 (2005).
[68] X.L. Zhou, Y.H. Chen, J.Q. Liu, C.H. Jia, G.Y. Zhou, X.L. Ye, B. Xu, and Z.G. Wang, "Temperature dependent photoluminescence of an In(Ga)As/GaAs quantum dot system with different areal density," J Phys D Appl Phys 43(29), (2010).
[69] A. P. Alivisatos, "Semiconductor Clusters, Nanocrystals, and Quantum Dots," Science

271, 933–937 (1996).
[70] L. Kong, Z.C. Feng, Z. Wu, and W. Lu, "Temperature dependent and time-resolved photoluminescence studies of InAs self-assembled quantum dots with InGaAs strain reducing layer structure," J Appl Phys 106(1), (2009).
[71] Z. Xu, Y. Zhang, A. Tackeuchi, Y. Horikoshi, and J.M. Hvam, "Short exciton radiative lifetime in submonolayer InGaAsGaAs quantum dots," Appl Phys Lett 92(6), (2008).
[72] W. Yang, R.R. Lowe-Webb, H. Lee, and P.C. Sercel, Effect of Carrier Emission and Retrapping on Luminescence Time Decays in InAs/GaAs Quantum Dots (1997).
[73] R. Heitz, M. Veit, N.N. Ledentsov, A. Hoffmann, D. Bimberg, V.M. Ustinov, P.S. Kop'ev, and Z.I. Alferov, Energy Relaxation by Multiphonon Processes in InAs/GaAs Quantum Dots (1997).
[74] B. Ilahi, L. Sfaxi, F. Hassen, H. Maaref, B. Salem, G. Guillot, A. Jbeli, and X. Marie, "Optical properties of 1.3 μm room temperature emitting InAs quantum dots covered by In0.4Ga0.6As/GaAs hetero-capping layer," Appl Phys A Mater Sci Process 81(4), 813–816 (2005).
[75] M. Colocci, A. Vinattieri, L. Lippi, F. Bogani, M. Rosa-Clot, S. Taddei, A. Bosacchi, S. Franchi, and P. Frigeri, "Controlled tuning of the radiative lifetime in InAs self-assembled quantum dots through vertical ordering," Appl Phys Lett 74(4), 564–566 (1999).
[76] B. Ilahi, O. Nasr, B. Paquette, M.H. Hadj Alouane, N. Chauvin, B. Salem, L. Sfaxi, C. Bru-Chevalier, D. Morris, R. Ares, V. Aimez, and H. Maaref, "Thermally activated inter-dots carriers' transfer in InAs QDs with InGaAs underlying layer: Origin and dependence on the post-growth intermixing," J Alloys Compd 656, 132–137 (2016).
[77] S. Sanguinetti, M. Henini, M. Grassi Alessi, M. Capizzi, P. Frigeri, and S. Franchi, Carrier Thermal Escape and Retrapping in Self-Assembled Quantum Dots (1999).
[78] Q. Li, S.J. Xu, M.H. Xie, and S.Y. Tong, "A model for steady-state luminescence of localized-state ensemble," Europhys Lett 71(6), 994–1000 (2005).
[79] Q. Yuan, B. Liang, C. Zhou, Y. Wang, Y. Guo, S. Wang, G. Fu, Y.I. Mazur, M.E. Ware, and G.J. Salamo, "Interplay Effect of Temperature and Excitation Intensity on the Photoluminescence Characteristics of InGaAs/GaAs Surface Quantum Dots," Nanoscale Res Lett 13, (2018).
[80] B. Liang, Q. Yuan, L. Su, Y. Wang, Y. Guo, S. Wang, G. Fu, E. Marega, Y.I. Mazur, M.E. Ware, and G. Salamo, "Correlation between photoluminescence and morphology for single layer self-assembled InGaAs/GaAs quantum dots," Opt Express 26(18), 23107 (2018).
[81] G.G. Tarasov, Y.I. Mazur, Z.Y. Zhuchenko, A. Maaßdorf, D. Nickel, J.W. Tomm, H. Kissel, C. Walther, and W.T. Masselink, "Carrier transfer in self-assembled coupled InAs/GaAs quantum dots," J Appl Phys 88(12), 7162–7170 (2000).

[82] S. Asahi, T. Kaizu, and T. Kita, “Adiabatic two-step photoexcitation effects in intermediate-band solar cells with quantum dot-in-well structure,” Sci Rep 9(1), (2019).
[83] S. Watanabe, S. Asahi, T. Kada, K. Hirao, T. Kaizu, Y. Harada, and T. Kita, “Two-step photocurrent generation enhanced by miniband formation in InAs/GaAs quantum dot superlattice intermediate-band solar cells,” Appl Phys Lett 110(19), (2017).
[84] S.J. Oon, T. Ohyama, N. Miyashita, and K. Yamaguchi, “Abnormal photoluminescence properties of InAs/InAsSb in-plane ultrahigh-density quantum dots,” Jpn. J. Appl. Phys. 63 (2024), pp. 085501 1-8.
[85] A. Sinha, R. Roychoudhury, and Y.P. Varshni, Wentzel-Kramers-Brillouin Quantization Rules for Two-Dimensional Quantum Dots (2003).
[86] J. Zhang, H. Lv, H. Ni, Z. Niu, and Y. Zhang, “Temperature dependence on the electrical and physical performance of InAs/AlSb heterojunction and high electron mobility transistors,” Chinese Physics B 27(9), (2018).
[87] R.M. Rubinger, G.M. Ribeiro, A.G. De Oliveira, H.A. Albuquerque, R.L. Da Silva, W.N. Rodrigues, and M.V.B. Moreira, Hall Effect in InAs/GaAs Superlattices with Quantum Dots: Identifying the Presence of Deep Level Defects (2004).
[88] A.F. Oliveira, R.M. Rubinger, H. Monteiro, C.P.L. Rubinger, G.M. Ribeiro, and A.G. de Oliveira, “Main scattering mechanisms in InAs/GaAs multi-quantum-well: a new approach by the global optimization method,” J Mater Sci 51(3), 1333–1343 (2016).
[89] H.Z. Song, K. Akahane, S. Lan, H.Z. Xu, Y. Okada, and M. Kawabe, “In-plane photocurrent of self-assembled (formula presented) quantum dot arrays,” Phys Rev B Condens Matter Mater Phys 64(8), (2001).
[90] A.M. Baró, and R.G. Reifenberger, Part I General Atomic Force Microscopy (2012).
[91] TOYO Corporation, LN-Type Cryostat Instruction Manual, Rev C (2015).
[92] K. Sumita, J. Takeyasu, K. Toprasertpong, M. Takenaka, and S. Takagi, “Influence of layer transfer and thermal annealing on the properties of InAs-On-Insulator films,” J Appl Phys 128(1), (2020).

List of Publications

Journal Papers

1) Sim Jui Oon, Takumi Ohyama, Naoya Miyashita, Koichi Yamaguchi: Abnormal Photoluminescence Properties of InAs/InAsSb In-Plane Ultrahigh-Density Quantum Dots. *Jpn. J. Appl. Phys.* **63** (2024), pp. 085501 1-8.

International Conference

1) Sim Jui Oon, N. Miyashita and K. Yamaguchi: "Photoluminescence Properties of InAs/InAsSb In-Plane Ultrahigh-Density Quantum-Dot Layer with In-Plane Energy Miniband". Publisher: Compound Semiconductor Week 2023 (CSW-2023), (May. 29-Jun 2, 2023), Jeju, P1-066.

Domestic Conference

1) Sim Jui Oon, Takumi Ohyama, Naoya Miyashita, Koichi Yamaguchi: Anomalous Photoluminescence Properties due to Strong Coupling of InAs/InAsSb In-Plane Ultrahigh-Density Quantum Dots. 71st JSAP Spring Meeting 2024 (Tokyo City University).

2) Sim Jui Oon, Mitsuya Arao, Naoya Miyashita, Koichi Yamaguchi: Abnormal Temperature Dependence of Photoluminescence Properties of In-Plane Ultrahigh-Density InAs/InAsSb Quantum-Dot Layer. 70th JSAP Spring Meeting 2023 (Sophia University).

3) Sim Jui Oon, Koichi Yamaguchi: Hall Effects of MBE Grown InAs Quantum Dots Crystal Structure. 48th UEC International Mini-Conference, August 2022.

4) Sim Jui Oon, Koichi Yamaguchi: Characterization of the Growth of Quantum Dots by Photoluminescence and Atomic Force Microscopy. 47th UEC International Mini-Conference, March 2022.

Acknowledgement

I would like to express my sincere gratitude to everyone who contributed to my Ph.D. journey. First and foremost, I would like to thank my supervisor, Prof. Koichi Yamaguchi, for his invaluable guidance, support, and encouragement. His expertise and insights played a key role in shaping my research, and I am deeply grateful for his constant dedication to my growth and success.

I would also like to extend my appreciation to the members of my dissertation committee: Prof. Tomah Sogabe, Prof. Tsuyoshi Okuno, Prof. Yoshinao Mizugaki, and Assoc. Prof. Naoya Miyashita. Their constructive feedback and thoughtful insights were helpful in refining this work. Their expertise offered valuable perspectives that significantly shaped the final outcome of my dissertation.

A special thanks goes to Ms. Mami Fukuchi, whose warmth and hospitality eased my transition to a new country and culture. Her kindness and support provided me with a sense of belonging and made my time in Japan much smoother and more enjoyable.

I am also grateful to the seniors and fellow lab members of the Yamaguchi laboratory, whose assistance and friendship enriched my research experience. Their support made this journey both meaningful and enjoyable. Additionally, I would like to acknowledge the MEXT scholarship for the generous financial support, which enabled me to focus fully on my academic and professional development.

Finally, I am deeply thankful to my family and friends for their constant encouragement, patience, and love. Their ongoing support provided me with the strength and motivation to overcome the challenges of this journey. I am forever grateful for their presence in my life.